Chapter 2

UBR Photometry of 39 Elliptical Galaxies[1]

Abstract

We have obtained U, B and R CCD surface photometry for a sample of 39 elliptical galaxies. For each galaxy we have determined the surface brightness profile, $U-R$ and $B-R$ color profiles, and the ellipticity and position angle profiles, all as a function of the major axis radius, using a two-dimensional ellipse fitting program. In addition, we have derived the sin and cos 3θ and 4θ terms that describe the high-order deviations of the B and R isophotes from ellipses. These high-order residuals are also given as 3θ and 4θ phases and amplitudes, which results in a clearer identification of the structures that contribute to the deviations. While it is very common for ellipticals to display measurable 3θ and 4θ terms, the amplitudes of these terms rarely exceeds 0.5%. The isophotes of elliptical galaxies are very well-characterised by ellipses.

The surface brightness and color profiles are given to radii at which the error in the profile reaches 0.1 mag from the uncertainty in the brightness of the night sky. We have carried out a series of simulations of the effects of seeing on luminosity and ellipticity profiles, to determine the radius beyond which the errors in our data from seeing are less than 0.05 mag and 0.02 in ellipticity. Measurable effects of seeing extend to surprisingly large radii, as much as 5-10 seeing radii, depending upon the ellipticity of the galaxy and the form of the surface brightness profile. Ellipticity and position angle profiles are usually the same in all passbands with no indication that the contours of constant color are more or less flattened than the isophotes, i.e., the isochromes and isophotes have the same shapes, but the insensitivity of the ellipticity to differences between these properties makes this a weak argument. The high-order terms, particularly the 3θ terms, appear to be sensitive diagnostics for the existence of dust in ellipticals. As noted by others, rotationally-flattened ellipticals can have disk-like or box-like residuals. The phase of the high-order residuals has

[1]Co-authored with R.L. Davies, G. Illingworth, L. Davis and M. Cawson

been found to be important for defining the feature contributing to the residuals from ellipses.

We find that all the galaxies in this sample either become bluer in $B-R$ and $U-R$ with increasing radius or are of constant color. Mean values for the logarithmic gradients in color are -0.09 mag (arcsec)$^{-2}$ per dex in radius in $B-R$, and -0.20 mag (arcsec)$^{-2}$ per dex in radius in $U-R$. These color changes are consistent with a decrease in the [Fe/H] of approximately 0.20 per decade in radius. Surprisingly, there is no correlation of color gradient with luminosity. It is striking, however, that the lowest luminosity galaxies in the sample (i.e., those with $M_B > -20$) do not show any color gradients. They have boxy isophotes, and are also rotationally-flattened. While these properties may be related to the fact that they are companions of larger ellipsoidal systems, it could provide an important clue to the formation of ellipticals. Low luminosity ellipticals that are not close companions to giant ellipticals need to be studied.

2.1 Introduction

We have undertaken a program of high-precision, multi-color, surface photometry for 39 elliptical galaxies. For most of the galaxies rotation curves and velocity dispersion profiles have been measured. These data provide a sound basis for exploring relationships between the structure, stellar populations, and kinematics of elliptical galaxies. Our aim is to investigate the intrinsic properties of elliptical galaxies and the mechanisms operating during their formation and evolution.

In this observing program we have emphasized the measurement of color gradients: here we report the only substantial body of modern galaxy surface that includes observations in the ultra-violet. The uncertainties involved in determining $U-R$ gradients are small compared the size of the gradient, so that the gradients are well established. In addition the ultra-violet band is more sensitive to changes in the age and metallicity of the population (Peletier *et al.*, 1989, Chapter 3). There is a well established relationship between the integrated luminosity of early type galaxies and their color such that more luminous galaxies are redder (Sandage and Visvanathan, 1978). Furthermore, all previous work on color gradients has shown that galaxies become bluer going outward (Boroson *et al.*, 1983, Davis *et al.*, (1985 – hereafter Paper I), Cohen, 1986). These two phenomena, the color-magnitude relation and the presence of color gradients, are widely thought to have a common physical origin, namely the higher metallicity of the stellar population in more luminous galaxies and towards the centers of individual galaxies (eg. Cohen, 1979). We find that, although there is a wide scatter, typical galaxies appear to be consistent with color gradients arising from metallicity gradients. The variation in $U-R$ and $B-R$ colors from galaxy to galaxy is also consistent with a change in metallicity causing the color-magnitude relation.

Models of the formation of galaxies involving the isolated collapse of a protogalactic gas cloud have shown to be able to generate color gradients in the end product (Larson, 1975). Color gradients have thus been used as evidence for the role of dis-

sipational processes in galaxy formation. In fact Larson's models produced galaxies that rotate too rapidly and have isochromes that are too flat when compared to real ellipticals. Carlberg (1984) modelled the isolated collapse of a gas cloud and included the effect that sites of star formation have in slowing the collapse. He produced slowly rotating galaxies with a smaller flattening of the ischromes. His model predicts that more luminous galaxies should possess steeper gradients. With the color gradients of this sample we are able to test this.

The observed isophote twisting in ellipticals can be used to explore their intrinsic shape. If low luminosity ellipticals are oblate (Davies *et al.*, 1983, hereafter called DEFIS), they should not exhibit isophote twisting. If ellipticals are triaxial, those galaxies viewed pole-on, that therefore appear roundest in projection, should exhibit the largest isophote twists. Luminosity profiles derived here can be combined with the observed kinematics for comparison with model elliptical galaxies to investigate the dependence of mass-to-light ratio with radius (eg. Binney, Davies and Illingworth, 1989). Recent studies of the structure of elliptical galaxies have emphasized the deviations of the isophote shapes from perfect ellipses (Bender *et al.*, 1988, Jedrezejewski, 1987). The higher order terms in the Fourier expansion of the isophote shapes have a typical amplitude of 0.5% of the light from an isophote. They have been shown to correlate surprising well with both the degree of rotational support and the radio power (Bender *et al.*, 1989). Here we explore these relationships further, identify a subclass of ellipticals that do not follow these trends and discuss possible orbit families that might be responsible for the observed correlations. We have adopted the phase and amplitude notation for the higher order terms suggested by Franx, Illingworth and Heckman (1989b) and have used this to identify unusual structures in a small number of galaxies. By determining the shape of galaxies in different bands we are sensitive to the presence of patchy dust. In addition we demonstrate that the third order terms in the Fourier expansion of the isophote shape are a sensitive indicator of the presence of dust. For galaxies free of the contaminating effects of dust we find that the shape of the stellar light is identical in U, B and R. This sample can be used to search for relationships between the stellar population and kinematics of elliptical galaxies. We are able to investigate the recent suggestion by Vader *et al.* (1988), that those galaxies that are flattened by rotation have the steepest color gradients.

In Paper I we described in some detail the observational program, the photometric and absolute calibration, the surface photometry analysis, and the results for a few galaxies, namely NGC 1052, NGC 3379 and M 87. In this paper we summarize the basic steps, and then pay particular attention to the effects of seeing, sky subtraction and the uncertainty in the calibration of the data for this very much larger sample. In §2.2 and §2.3 we discuss how the data were obtained, reduced and analyzed. In §2.4 the results of a quantitative numerical evaluation of the effects of seeing are presented, followed in §2.5 by the results of this program (with the complete data being tabulated and plotted in Appendix A). The implications of these new data are discussed and summarized in §2.6 and §2.7. In Appendix B we comment on individual galaxies, noting the problems that arose during the analysis,

while highlighting results of particular interest for each galaxy. In a later paper we will analyze the observed color gradients and their relationship to other galaxy parameters in more detail.

2.2 Observations

The elliptical galaxy sample was selected primarily from the tabulation by Davies *et al.* (1983) of 58 ellipticals with velocity and velocity dispersion profiles. In addition, we included those ellipticals in the kinematic mapping study by Davies and Birkinshaw (1988) for which surface photometry was not available, as well as a selection of very luminous ellipticals (cD's and other brightest cluster members). These latter galaxies were taken from Tonry and Davis (1981), Carter *et al.* (1985), and Illingworth and Jedrzejewski (1989). The sample consists of 39 elliptical galaxies ranging in ellipticity from $\epsilon \approx 0$ to $\epsilon \approx 0.6$, and with absolute luminosities in the range $-18 > M_B > -24.5$ (for $H_0 = 50$ km s^{-1}Mpc^{-1}). In Table 2.1 we have summarized some basic data for the galaxies of the sample.

The objects were observed between May 1982 and May 1985 with the #1 0.9-m and the 2.1-m telescopes at Kitt Peak National Observatory. The data from the two telescopes are complementary. The RCA CCD on the 0.9-m telescope offered a large field of view ($5' \times 7'$), but poorly sampled data, and was best-suited to observing the largest and brightest galaxies, whereas the 2.1-m with the RCA CCD gave us the higher spatial resolution and better sampling that was advantageous for the smaller and fainter galaxies. A log of the observations is presented in Table 2.2.

Exposure times were typically 600s in R, 1600s in B and 2000s in U. These times were chosen to equalize the signal-to-noise ratio achieved on the galaxy in R and B; at the point where the galaxy is 5% of the sky brightness a S/N of approximately 15 is achieved by averaging 50 pixels. The exposure time in U was sufficient to produce good data only to radii approximately one-half of those in B and R.

The characteristics of the RCA CCD camera (#1, and occasionally #2) used on the #1 0.9-m telescope for most of this work are given in Paper I. The RCA CCD (#3) used on the 2.1-m telescope at the f/7.5 focus differed little from #1 and #2. CCD #3 has a readout noise of 41 electrons, possesses no serious cosmetic blemishes, is free from "residual" image effects (i.e., saturated pixels do not retain charge into subsequent frames), and is linear up to the limit of digitization. The main disadvantage of this CCD is that there is thorium in the glass substrate on which it is mounted. The thorium decay generates a high radiation event rate of more than 400 events per hour. Fortunately, for the large galaxies studied here these events could easily be masked with minimal effect upon the data. None of these three CCD's shows any significant fringing with the filters used here. The field at the 2.1-m was 3.2′(E-W) x 2.0′(N-S), and the pixels subtended 0.38″ . The characteristics of the U,B and R filters used on both telescopes are summarized in Table III of Paper I. The KPNO Mould U, B and R filter set was used for these observations, and the results transformed onto the Cousins system (see Paper I, and §2.3).

Table 2.1: Global Parameters

Galaxy	Classification		v_{grp}	M_{B_T}	Environment
	RC2	RSA	km s^{-1}		
(1)	(2)	(3)	(4)	(5)	(6)
NGC 315	SA0	– –	5303	-23.59	– –
NGC 720	E5/E3	E5	1728	-21.53	– –
NGC 741	E0/E1	E0	5347	-23.10	Group with N742
NGC 1052	E4/E2	E3/S0	1392	-20.94	Brightest in N1052 group
NGC 1129	– –	– –	5320	-23.68	AWM 7
NGC 1600	E3/E2	E4	4846	-23.14	N1600 group
Abell 496	– –	– –	9780	-23.16	– –
NGC 2300	SA0/E1	E3	2256	-21.54	– –
NGC 2768	E6/E5	$S0_{0,1}$	1355	-21.16	– –
NGC 2778	– –	– –	1827	-19.51	Group with N2779
NGC 2832	E2	E3	6780	-22.86	Group with N2831
NGC 3377	E5/E5	E6	667	-19.50	Leo group
NGC 3379	E1/E1	E0	667	-20.20	Leo group
NGC 3605	E4/E3	E5	1033	-18.34	In N3607 group
NGC 3665	SA0/E2	$S0_3$	2090	-21.36	– –
NGC 3801	S0p	– –	3171	-21.33	Pair with N3802. Dusty
NGC 4261	E2/E2	E3	2087	-21.78	Pair with N4264
NGC 4278	E1/E1	E1	754	-19.87	Pair with N4283
NGC 4374	E1/E1	E1	1074	-21.53	– –
NGC 4387	E5	– –	1074	-18.79	– –
NGC 4406	E3/E3	$S0_1$/E3	1074	-21.79	– –
NGC 4472	E2/E4	E1/$S0_1$	1074	-22.34	Pair with N4467
NGC 4478	E2/E1	E2	1074	-19.52	Pair with N4476
NGC 4486	E0p/E1	E0	1074	-22.14	Virgo A
NGC 4551	E3	– –	1074	-18.94	Pair with N4550
NGC 4636	E0/E1	E0/$S0_1$	1074	-21.46	– –
NGC 4649	E2/E1	$S0_1$	1074	-21.89	Pair with N4647
NGC 4697	E6/E4	E6	1071	-21.63	– –
NGC 4874	E0	– –	6931	-23.40	Central Coma galaxy
NGC 4889	E4/E4	E4	6931	-23.23	Central Coma galaxy
NGC 5638	E1/E1	E1	1596	-20.47	Pair with N5636
NGC 5813	E1/E1	E1	1673	-21.23	In N5846 group
NGC 5831	E3/Ep	E4	1673	-20.33	– –
NGC 5845	E3	– –	1673	-19.27	In N5846 group
IC 1101	– –	– –	23300	-24.40	Abell 2029 cD
NGC 6051	E4	– –	9722	-22.95	AWM 4
NGC 6086	E2	– –	9704	-22.95	Abell 2162 cD
NGC 6269	– –	– –	10700	-23.63	AWM 5
NGC 7626	E1p/E2p	E1	3693	-22.35	Second brightest in Pegasus I

Notes to Table 2.1:
Columns (2) and (3) list the galaxy classifications from the RC2 (De Vaucouleurs *et al.*, 1976) and the RSA (Sandage and Tammann, 1981). Column (4) gives the group velocity from Davies *et al.* (1987), corrected for the motion with respect to the centroid of the local group, using the approach in the RC2. Column (5) lists the integrated blue luminosity M_{B_T}, calculated using the group velocity and B_T from Burstein *et al.* (1987). For a few galaxies other sources have been used to obtain the group velocity and the apparent blue magnitude. The remarks on the environment of the galaxies in column (6) are taken mostly from the RC2.

Table 2.2: Observation log

Galaxy (1)	RA (2)	Dec (3)	Period/Tel. (4)	Qual. (5)	Band (6)	Exp.times (7)
NGC 315[1]	00 55.1	30 05	Jan 84/0.9[2]	2	R	100,600
					B	1600
					U	2000
NGC 720	01 50.6	-13 59	Oct 82/0.9	2	R	600
					B	1600
					U	2000
NGC 741	01 53.8	05 23	Jan 84/0.9	2	R	100,600
					U	2000
			Dec 86/1.5		R	200
					B	360
NGC 1052	02 38.6	-08 28	Oct 82/0.9	1	R	100,600
					B	800+800
					U	2000
NGC 1129[3]	02 52.9	41 26	Jan 84/0.9	2	R	100,600
					B	1600
					U	2000
NGC 1600	04 29.2	-05 12	Oct 82/0.9	2	R	600
					B	1600
					U	2000
			Dec 86/1.5		R	180
					B	300
Ab. 496[3]	04 31.3	-13 22	jan 84/0.9	3	R	100,1200
					B	2400
					U	3600
NGC 2300[3]	07 16.0	85 49	apr 84/0.9	2	R	100(2),600
					B	1600
					U	2000
NGC 2768	09 07.7	60 15	Apr 84/0.9	1	R	100,600
					B	1600
					U	2000
NGC 2778	09 09.2	35 13	Jan 84/0.9	1	R	600+600
					B	1600+1600
					U	2000+2000
			May 85/2.1		R	300+300
					B	1000
					U	2400
NGC 2832	09 16.8	33 58	Jan 84/0.9	1	R	600
					B	1600
					U	2000
NGC 3377	10 45.1	14 15	May 85/2.1	1	R	50,100
					B	150
					U	1800
NGC 3379	10 45.2	12 51	Jan 84/0.9	1	R	100
					U	2000
			Apr 84/0.9		R	100(2),300(2)
					B	1600
NGC 3605[4]	11 14.1	18 17	Apr 84/0.9	1	R	100(2),600(2)

Table 2.2: Observation log

Galaxy (1)	RA (2)	Dec (3)	Period/Tel. (4)	Qual. (5)	Band (6)	Exp.times (7)
					B	1600(2)
					U	2000
			May 85/2.1		R	300(2)
					B	1000
					U	2400
NGC 3665	11 22.0	39 02	Jan 84/0.9	1	R	100,600
					B	1600
					U	2000
NGC 3801	11 37.7	18 00	Jan 84/0.9	1	R	100,600
					B	1600
					U	2000
NGC 4261	12 16.8	06 06	Jan 84/0.9	1	R	100,600
					B	1600
					U	2000
NGC 4278	12 17.6	29 33	Jan 84/0.9	1	R	100,600
					B	1600
					U	2000
NGC 4374	12 22.5	13 10	Jan 84/0.9	1	R	100,600
					B	1600
					U	2000
			May 85/2.1		R	100(2)
					B	300
NGC 4387[3]	12 23.2	13 05	Jan 84/0.9	1	R	100,600
					U	2000
			Apr 84/0.9		R	100,600
					U	1600
			May 85/2.1		R	300(3),600
					B	2000
					U	2400
NGC 4406	12 23.7	13 14	Jan 84/0.9	1	R	100,600
					B	1600
					U	2000
NGC 4472	12 27.3	08 16	Apr 84/0.9	1	R	100,300
					B	1600
					U	2000
NGC 4478[3]	12 27.8	12 36	Jan 84/0.9	1	R	100,600
					B	1600
					U	2000
			May 85/2.1		R	300(2)
					B	1000
					U	2400
NGC 4486	12 28.3	12 40	Mar 84/0.9	1	R	300
					B	600(2)
					U	2000
NGC 4551[3]	12 33.1	12 32	Jan 84/0.9	1	R	600
					U	2000
			Apr 84/0.9		R	100,600

Table 2.2: Observation log

Galaxy (1)	RA (2)	Dec (3)	Period/Tel. (4)	Qual. (5)	Band (6)	Exp.times (7)
					B	1600
			May 85/2.1		R	300(2)
					B	1000
					U	2400
NGC 4636	12 40.3	02 58	Apr 84/0.9	1	R	100,600
					B	1600
					U	2000
NGC 4649	12 41.2	11 49	Apr 84/0.9	1	R	100,600
					B	1600
					U	2000
NGC 4697	12 47.1	-05 40	Jan 84/0.9	1	R	100(2),300
					U	2000(2)
			Apr 84/0.9		R	100,300
					B	600,1600
NGC 4874	12 57.2	28 14	Jan 84/0.9	3	R	100,600
					B	1600
					U	2000
NGC 4889	12 57.7	28 15	Jan 84/0.9	2	R	100,600
					B	1600
					U	2000
NGC 5638	14 27.2	03 27	May 85/2.1	1	R	300,1000(2)
					B	2000
					U	2400
NGC 5813[3]	14 58.6	01 53	Jan 84/0.9	1	R	600
					U	2000
			Apr 84/0.9		R	100(2),600
					B	1600(2)
			May 85/2.1		R	300(2)
					B	1000
					U	2400
NGC 5831[3]	15 01.6	01 24	Jan 84/0.9	1	R	100,600
					U	2000
			Apr 84/0.9		R	100,600
					B	1600
			May 85/2.1		R	300(2)
					B	800
					U	2400
NGC 5845[3]	15 03.5	01 48	Jan 84/0.9	1	R	100,600
					U	2000
			Apr 84/0.9		R	100,600
					B	1600
			May 85/2.1		R	150(2),300
					B	500
					U	2400
IC 1101	15 08.4	05 56	Apr 84/0.9	1	R	600,1200
					B	1600
					U	2000

Table 2.2: Observation log

Galaxy (1)	RA (2)	Dec (3)	Period/Tel. (4)	Qual. (5)	Band (6)	Exp.times (7)
			May 85/2.1		R	600,1000(2)
					B	2000(2)
					U	2400(2)
NGC 6051	16 02.8	24 04	May 85/2.1	3	R	300(3)
					B	1000
					U	2400(2)
NGC 6086	16 10.5	29 38	Apr 84/0.9	3	R	100,600
					B	1600
					U	2000
			May 85/2.1		R	300
					B	1000
					U	2100
NGC 6269	16 56.0	27 56	Apr 84/0.9	3	R	100,600
					B	1600
					U	2000
			May 85/2.1		R	300,600
					B	2000
					U	2100
NGC 7626	23 18.2	07 56	Oct 82/0.9	1	R	600
					B	600
					U	2000

Notes to Table 2.2:
The RA and Dec in columns (2) and (3) are 1950 coordinates. The Quality parameter in column (5) is discussed in the text. The exposure times are in seconds.

1. For NGC 315, the scattered light from a very bright star close to the frame was modelled and subtracted.
2. Telescopes : **2.1** – 2.1m KPNO; **0.9** – #1 0.9m KPNO; **1.5** – 1.5m Danish telescope at ESO.
3. A N-S ramp in the background across the detector that was caused by leakage from a red light close to the detector was modelled and subtracted from the 0.9 m R-band frames.
4. A sloping background due to contamination from a large nearby galaxy, NGC 3607, was subtracted.

2.3 Reduction and Analysis

The data were reduced as described in paper I. We determined the median bias level from the 32 column overscan region of each row of each frame and subtracted it. We then trimmed the frames to 320 × 512, subtracted the bias frame, and divided each galaxy and star frame by the flat field frame taken through the appropriate filter. We used high S/N dome flat field frames taken at the beginning and end of each night. Sky frames were used to verify, and correct if necessary, the uniformity of the flat-fields. No fringing (>0.5%) from night sky lines was observed. We subsequently noticed that some R-frames from the #1 0.9-m telescope, contained small (<1.5% across the detector) background gradients from north to south. These frames are identified in Table 2.2. The gradients were removed by subtracting a linear fit to the background. The gradients were apparently due to an inadequately masked red light in the dome.

2.3.1 Isophote Fitting and Profiles

Luminosity profiles were determined using a version of GASP (Cawson, 1983). The GASP system has been described in detail in paper I. It is used interactively in conjunction with a color image display. A device-mask, identifying all the 'bad' pixels on a given CCD, was generated and applied to all frames, so that none of the 'hot' pixels or columns with traps, etc., were included in the analysis. For each galaxy frame, all the interfering images that were superimposed on the galaxy to be measured, such as stars, small companion galaxies, and cosmic rays, were automatically identified and masked out. In some cases this automatic procedure was augmented by manual identification of objects. Elliptical isophotes were then fitted to the galaxy using a revised version of the program PROF. We are grateful to R. Jedrezejewski for giving us a much faster version of this program. The program takes the preliminary (x, y) center, position angle and ellipticity which had been estimated in the image-finding step, and samples the pixel-data around an ellipse of given major-axis length. If the isophotes of the galaxy are elliptical, and the estimated parameters of the sampling ellipse are close to the true values, then the variation in pixel-values $I(\theta)$ around the sampling-ellipse can be expressed as a Fourier-series with small first and second order terms. The intensity along the ellipse is approximated by

$$I(\theta) = \sum_{i=1}^{2} C_i \cos(i\theta) + \sum_{i=1}^{2} S_i \sin(i\theta).$$

and this equation is fitted to give the Fourier coefficients. An iterative least-squares fitting procedure adjusts the ellipse parameters until the sum of the squared residuals between the data and the ellipse is smaller than a set threshold, or a set number of iterations has been reached. The process was repeated at major axis radii each of which was a factor 1.1× larger than the previous step, until less than 60% of an

isophote was included in the frame, or the galaxy surface brightness fell to 1% of the sky.

The final step at each radius is the determination of any deviations from elliptical isophotes. The third and fourth order Fourier coefficients were determined from fitting

$$I(\theta) = \sum_{i=1}^{4} C_i \cos(i\theta) + \sum_{i=1}^{4} S_i \sin(i\theta),$$

with the low order coefficients held constant. That is, in this final step there was no iteration; C_1, C_2, and S_1, S_2 were held constant. We simply solve for the high-order terms, and so the coefficients do not strictly describe an isophote; the error introduced is inconsequential, since the deviations are very small, being typically 0.5%.

An ellipse is specified completely by the first and second order Fourier terms, so the third and fourth order coefficients are zero for perfectly elliptical isophotes. For isophotes with threefold symmetry the sin 3θ (S3) and/or the cos 3θ (C3) term are non-zero. Similarly, the sin 4θ (S4) and cos 4θ (C4) terms describe shapes with four-fold symmetry; maxima of intensity at 0°, 90°, 180° and 360° have positive C4-terms (all angles are measured from the major axis of the isophote). The presence of a stellar disk along the major axis, i.e., excess light on this axis, is indicated by a positive C4-term. 'Boxy' isophotes with their 'corners' at 45° to the major and minor axis give negative cos 4θ-terms. If these features were oriented at angles shifted by 22.5° with respect to the major and minor axis, then the S4-term would be significant. Non-zero C4-terms are particularly interesting, since they are characteristic of physically interesting structures in galaxies. As we shall see, such structures ("disk-like" and "boxy") are surprisingly common in elliptical galaxies, but with very low amplitude, typically 0.5%. Four examples of model galaxy isophotes with 3θ and 4θ terms of amplitude 5% (10× typical) are shown in Figure 2.1 for an E4 elliptical.

The accurate determination of the 3θ and 4θ terms requires higher S/N data than is needed for luminosity, ellipticity and position angle profiles. For some galaxies, especially the cD's, the amplitudes of these terms are rather uncertain, as can be inferred from the scatter in the values at neighboring radii. This was particularly true for the determination of these terms from the U-band data; as a result, the 3θ and 4θ terms are not shown for the U data.

A subjective quality parameter was assigned to the data of each galaxy. Quality parameter 1 was assigned to those surface brightness measurements with low internal scatter that reproduced well in multiple observations. A few of the fainter galaxies (of low apparent magnitude) could be measured over only a limited radius range due to the poor seeing and/or poor signal-to-noise; these galaxies were assigned quality parameter 3. Intermediate cases were assigned quality 2. These quality parameters are given in Table 2.2. A more direct assessment of the quality of the data can be obtained by inspection of the results in Figure 2.17 (Appendix A).

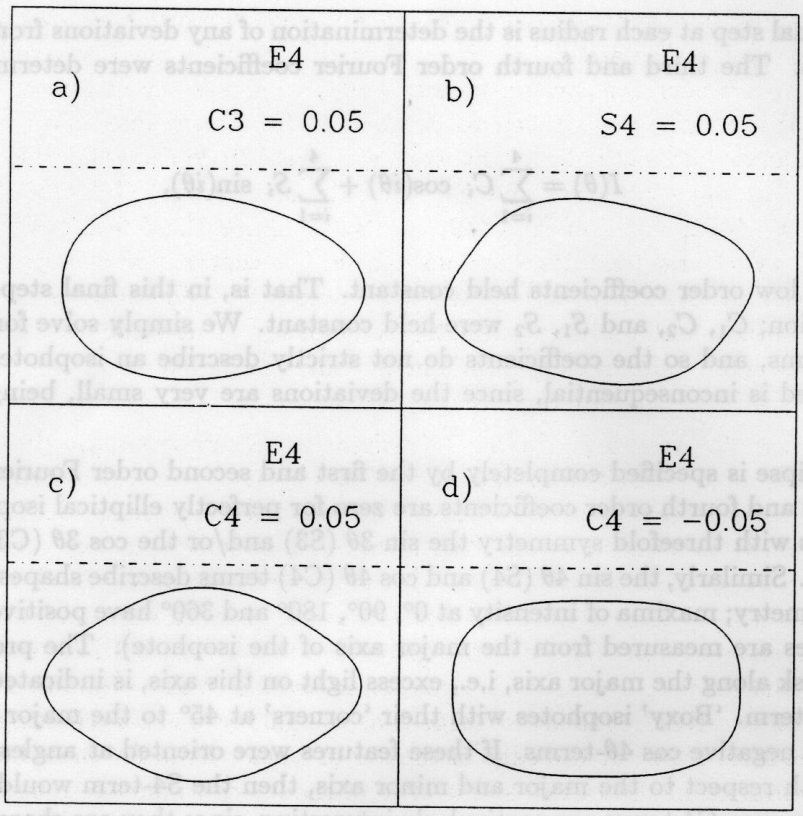

Figure 2.1: *Isophotes of model galaxies with non-zero high order Fourier terms. Several E4 model ellipticals are shown with 3θ and 4θ terms with an amplitude 0.05 (10× typical) added to the model. Figure 2.1a has three-fold symmetry from the addition of a positive cos3θ term; Figures 2.1b-d show four-fold symmetry from added positive sin4θ (in 2.1b), added positive cos4θ (in 2.1c), and added negative cos4θ (in 2.1d). The shape in Figure 2.1c is characteristic of a major or minor axis disk, while that in Figure 2.1d is characteristic of "boxy".*

2.3.2 Sky Subtraction

Most galaxies were sufficiently small that we could measure the sky directly from the galaxy frame. We applied the 'boxes' method from paper I, wherein the pixels in small arrays near the corners were averaged to give a sky estimate. The global average of the arrays was taken to be the sky for that frame. For a number of larger galaxies this method did not work very well, since the galaxy itself was still detectable at the edges of the frame. These galaxies were NGC 2768, 3377, 3379, 4374, 4406, 4472, 4486, 4636, 4649 and 4697. Since the 0.9-m field was 7.5′ × 4.5′, and some large galaxies were offset from the center of the frame, the galaxy contribution at the edges was only a few percent of sky. For these large galaxies we used the 'boxes' method to get an initial value of sky. This value was then corrected slightly so that the luminosity profile in the outer parts fell off with the same slope as that in the intermediate regions.

To assess the accuracy of our sky estimates we compared the profiles for the twelve galaxies with data from both the 0.9-m and the 2.1-m telescopes. The 'boxes' method, with its correction from the luminosity profile when needed, was applied independently to both 0.9-m and 2.1-m frames, after which the sky-subtracted profiles were compared. The radius at which sky could be determined on the 2.1-m was about half as large as on the 0.9-m. We found that no adjustment of the 2.1-m sky level was necessary for six of the galaxies; the 0.9-m and 2.1-m profiles agreed. Of the remainder, four required a decrease in the 2.1-m sky estimate of about 1%. NGC 4374 and NGC 5813 are so large that the galaxy was contributing more than 5% of the level of sky at the edge of the 2.1-m frame. Even for these large galaxies the contribution of the galaxy at the edge of the 0.9-m frame was only of the order of 1% of sky. After correction the sky values should be determined to this level or better. To summarize, we expect, conservatively, that for our best data (those galaxies with quality parameter 1) the uncertainty in sky to be approximately 1%. For the very large galaxies (listed above) the error could be as large as 2%.

An additional diagnostic for sky (and flat field) problems is the position of the center of the galaxy. Any linear gradients will tend to move the center of the outer isophotes systematically in one direction. Of course, real changes in the central position could occur if asymmetries exist due to dust, interactions, etc. However, the shifts found were very small or non-existent, being <0.5 pixel on the 0.9-m telescope, and even less on the 2.1-m, suggesting that both sky problems and other effects are minimal.

The profiles determined from the 0.9-m and 2.1-m telescope data are compared in Figure 2.2 (after adjustment of the 2.1-m sky values). We have applied an inner radial cutoff, to account for uncertainty introduced by the effects of seeing (see §2.4). The cutoff was based on the best seeing, so the effects of the poorer seeing frames (usually from the 0.9-m telescope) are still visible. For each galaxy the best 2.1-m frame was subtracted from the best 0.9-m frame, after correcting the 2.1-m sky background. The dominant source of noise in these comparisons is the 0.9-m data. For some galaxies, for which the 0.9-m data is poor (e.g., NGC 6086 and NGC

6269) the comparisons show large scatter. Differences in the U band have the largest amplitude, because the signal in U is the smallest on both telescopes.

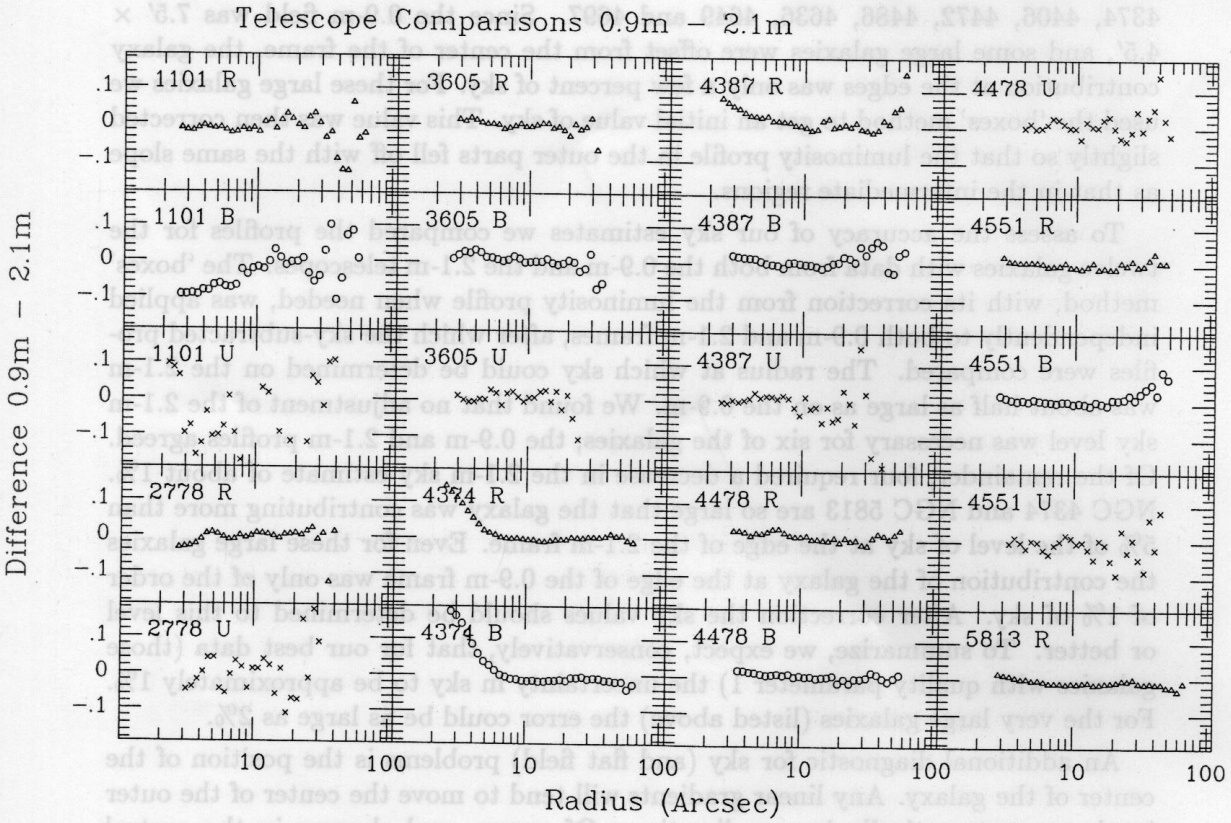

Figure 2.2: *Comparison of the profiles from the 0.9-m and the 2.1-m data, after correction of the 2.1-m sky levels. The profiles have been limited to the radial range set by the 2.1-m seeing at small radii (§2.4) and the sky uncertainty at large radii (§2.3.2). Some seeing effects from the 0.9-m are apparent. The U data are crosses, the B data are open circles, and the R data are open triangles.*

We also checked whether our profiles were reproduced from frame to frame. More than one frame is available in R from the 0.9-m for 20 galaxies. These typically

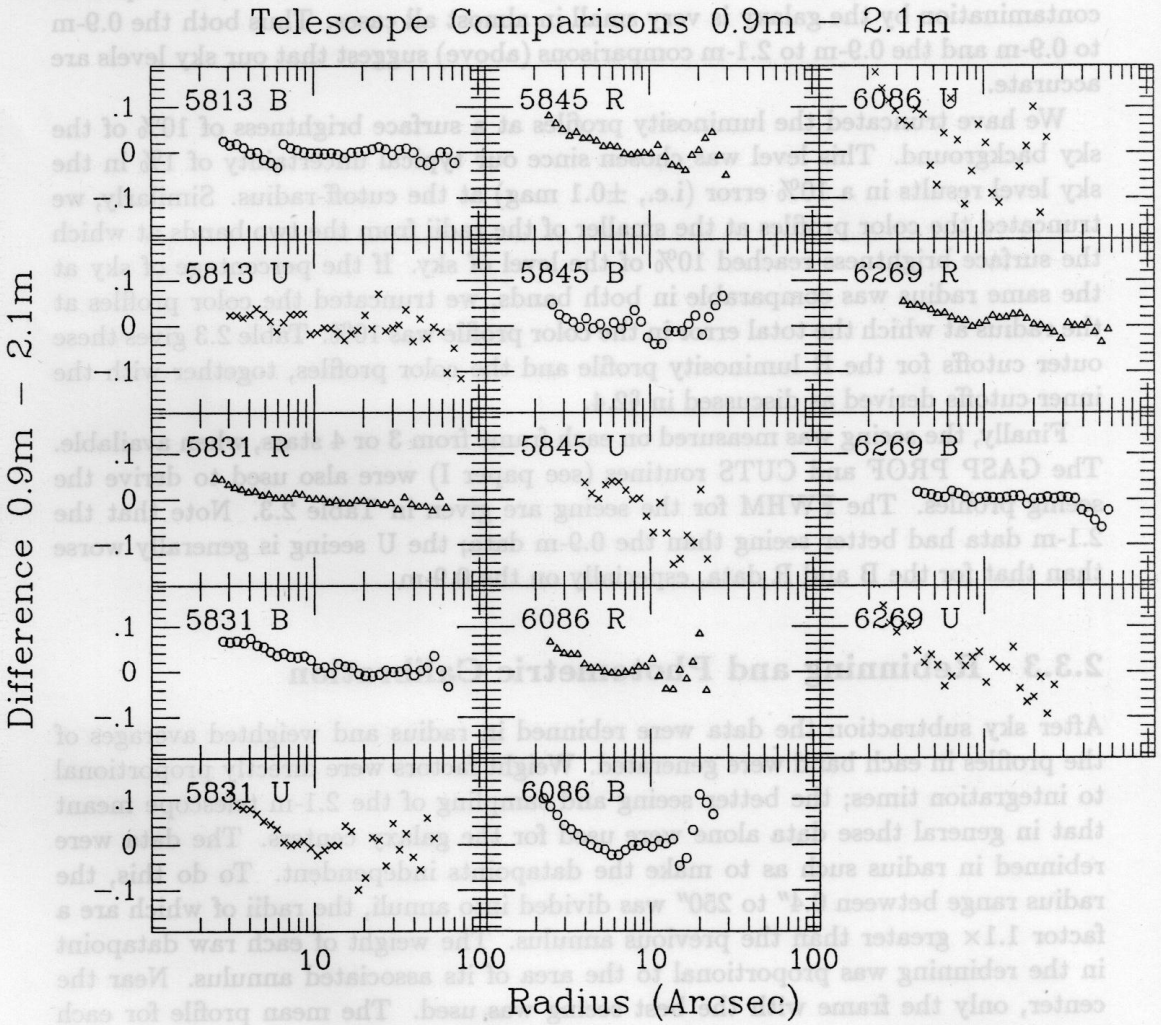

Figure 2.2: *Continued.*

have different integration times. The sky level was determined independently on each frame, and the surface brightness profile obtained from PROF. The differences between the profiles determined from these separate frames are shown in Figure 2.3. Except for systematic effects due to seeing differences near the nucleus, the subtracted profiles show no systematic trends with radius. Of course, some systematic problems could still occur since the frame size remained the same and the sky was determined in the same way in each frame. However, as noted above, the expected contamination by the galaxy is very small in almost all cases. Thus both the 0.9-m to 0.9-m and the 0.9-m to 2.1-m comparisons (above) suggest that our sky levels are accurate.

We have truncated the luminosity profiles at a surface brightness of 10% of the sky background. This level was chosen since our typical uncertainty of 1% in the sky level results in a 10% error (i.e., ± 0.1 mag) at the cutoff-radius. Similarly, we truncated the color profiles at the smaller of the radii from the two bands at which the surface brightness reached 10% of the level of sky. If the percentage of sky at the same radius was comparable in both bands, we truncated the color profiles at the radius at which the total error in the color profile was 10%. Table 2.3 gives these outer cutoffs for the R luminosity profile and the color profiles, together with the inner cutoffs derived as discussed in §2.4.

Finally, the seeing was measured on each frame from 3 or 4 stars, when available. The GASP PROF and CUTS routines (see paper I) were also used to derive the seeing profiles. The FWHM for the seeing are given in Table 2.3. Note that the 2.1-m data had better seeing than the 0.9-m data; the U seeing is generally worse than that for the B and R data, especially on the 0.9-m.

2.3.3 Rebinning and Photometric Calibration

After sky subtraction the data were rebinned in radius and weighted averages of the profiles in each band were generated. Weight factors were directly proportional to integration times; the better seeing and sampling of the 2.1-m telescope meant that in general these data alone were used for the galaxy centers. The data were rebinned in radius such as to make the datapoints independent. To do this, the radius range between 0.4″ to 250″ was divided into annuli, the radii of which are a factor 1.1× greater than the previous annulus. The weight of each raw datapoint in the rebinning was proportional to the area of its associated annulus. Near the center, only the frame with the best seeing was used. The mean profile for each parameter ($\mu(r)$, ϵ, etc.) was derived by averaging in this way. The profiles were not necessarily sampled at the same radii, so we had to interpolate in radius to generate color profiles. We used a fifth-order polynomial interpolation. Since the profiles were well-sampled in radius there was no loss of information.

Systematic differences in scale between the images in the three bands could have caused systematic errors in the measured color gradients. In paper I we showed that scale differences at the #1 0.9-m were insignificant. The scale differences were determined again by measuring the accurate positions of stars on glass copies of the

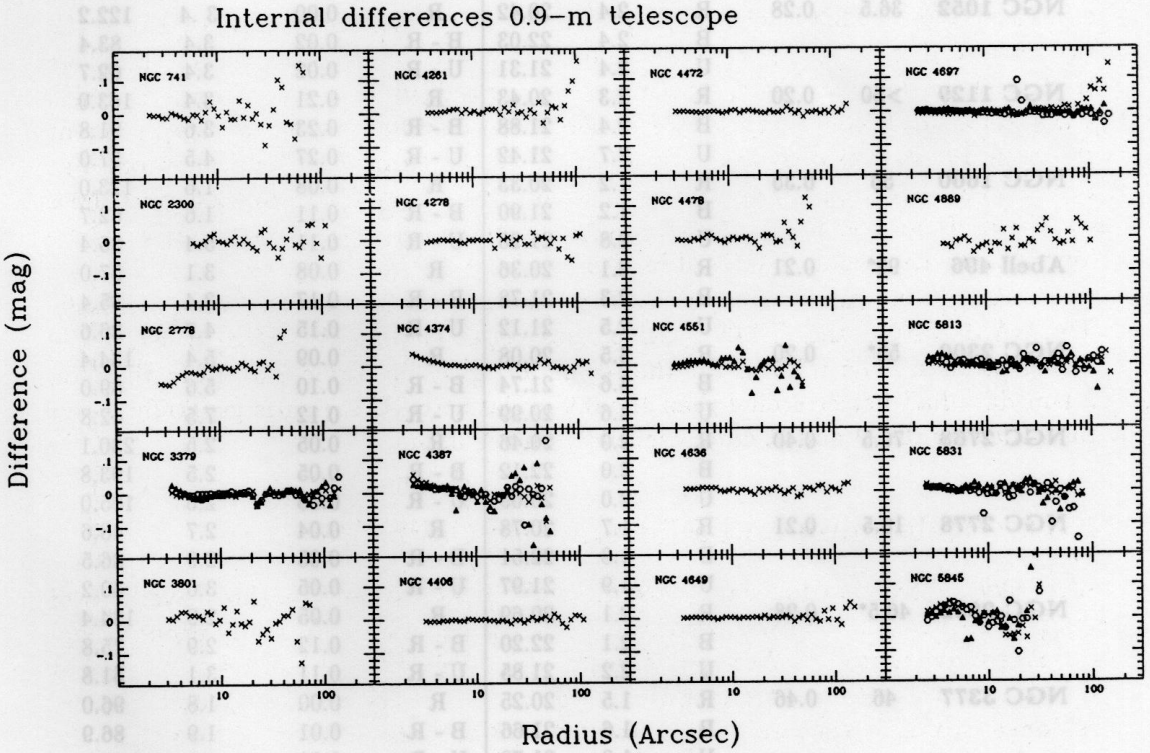

Figure 2.3: *Comparison of the profiles obtained independently from different R frames on the 0.9-m. The cutoff radii have been set by the seeing (in the center, §2.4) and by the sky uncertainty at large radii (§2.3.2). Different symbols indicate comparisons with different R-frames.*

Table 2.3: Seeing, background and cutoff radii

Galaxy	r_e ″	ϵ at 10″	Band	Seeing ″	Sky	Profile	Ext. + K Correction	Inner Cutoff	Outer Cutoff
(1)	(2)	(3)	(4)	(5)	(6)	(7)	(8)	(9)	(10)
NGC 315	68	0.26	R	2.3	20.59	R	0.08	3.2	122.2
			B	3.0	22.12	B - R	0.11	6.3	57.0
			U	3.5	21.72	U - R	0.12	7.7	57.0
NGC 720	52	0.40	R	2.1	20.34	R	0.01	2.6	163.0
			B	2.1	21.88	B - R	0.02	2.6	111.1
			U	2.4	20.84	U - R	0.01	4.0	69.0
NGC 741	57.5	0.17	R	1.4	20.10	R	0.02	2.1	83.4
			B	1.4	21.67	B - R	0.07	2.1	51.8
			U	2.8	21.14	U - R	0.05	7.0	32.2
NGC 1052	36.5	0.28	R	2.4	20.42	R	0.00	3 .4	122.2
			B	2.4	22.03	B - R	0.02	3.4	83.4
			U	2.4	21.31	U - R	0.02	3.4	62.7
NGC 1129	>50	0.20	R	2.3	20.43	R	0.21	3.4	163.0
			B	2.4	21.88	B - R	0.23	3.6	91.8
			U	2.7	21.42	U - R	0.27	4.5	57.0
NGC 1600	56	0.35	R	1.2	20.33	R	0.08	1.6	123.0
			B	1.2	21.90	B - R	0.11	1.6	62.7
			U	2.8	21.25	U - R	0.11	5.4	35.4
Abell 496	93*	0.21	R	2.1	20.36	R	0.08	3.1	57.0
			B	2.3	21.78	B - R	0.17	3.4	35.4
			U	2.5	21.12	U - R	0.15	4.7	26.6
NGC 2300	55*	0.20	R	3.5	20.08	R	0.09	5.4	134.4
			B	3.6	21.74	B - R	0.10	5.6	69.0
			U	4.6	20.99	U - R	0.12	7.5	42.8
NGC 2768	76.5	0.40	R	2.0	20.46	R	0.05	2.5	230.1
			B	2.0	22.12	B - R	0.05	2.5	193.8
			U	2.0	20.69	U - R	0.05	2.5	105.0
NGC 2778	18.5	0.21	R	1.7	20.78	R	0.04	2.7	48.6
			B	1.8	22.51	B - R	0.05	2.9	36.5
			U	1.9	21.97	U - R	0.05	3.0	30.2
NGC 2832	46.5*	0.28	R	2.1	20.69	R	0.05	2.9	134.4
			B	2.1	22.20	B - R	0.12	2.9	75.8
			U	2.2	21.85	U - R	0.11	3.1	51.8
NGC 3377	46	0.46	R	1.5	20.25	R	0.00	1.8	96.0
			B	1.6	21.66	B - R	0.01	1.9	86.9
			U	1.9	21.72	U - R	0.01	4.9	86.9
NGC 3379	37.5	0.10	R	2.0	20.41	R	0.00	3.3	170.0
			B	3.4	22.17	B - R	0.01	6.6	127.8
			U	2.1	21.64	U - R	0.01	3.5	105.6
NGC 3605	22.5	0.40	R	2.3	20.53	R	0.00	2.9	39.7
			B	2.0	22.10	B - R	0.01	2.9	32.8
			U	2.3	21.49	U - R	0.01	2.9	27.1
NGC 3665	65.5*	0.38	R	2.2	20.87	R	0.01	2.8	178.9
			B	2.1	22.56	B - R	0.02	2.8	111.1
			U	2.2	21.92	U - R	0.02	2.8	83.4
NGC 3801	44.5*	0.30	R	2.1	20.81	R	0.01	2.9	86.9
			B	2.6	22.41	B - R	0.04	4.9	65.2

Table 2.3: Seeing, background and cutoff radii

Galaxy	r_e	ϵ	Band	Seeing	Sky	Profile	Ext. + K	Inner	Outer
	$''$	at 10$''$		$''$			Correction	Cutoff	Cutoff
(1)	(2)	(3)	(4)	(5)	(6)	(7)	(8)	(9)	(10)
			U	3.2	22.23	U - R	0.03	7.0	59.3
NGC 4261	42.5	0.24	R	2.5	20.68	R	0.01	3.7	125.9
			B	2.6	22.28	B - R	0.02	3.8	78.2
			U	2.7	22.10	U - R	0.02	4.0	64.7
NGC 4278	35	0.14	R	2.0	20.71	R	0.00	3.2	160.0
			B	1.7	22.21	B - R	0.01	3.3	108.1
			U	2.7	21.87	U - R	0.01	5.1	89.4
NGC 4374	57	0.20	R	1.6	20.65	R	0.00	2 .4	164.0
			B	1.8	22.48	B - R	0.01	3.3	163.3
			U	4.0	22.15	U - R	0.01	6.3	112.0
NGC 4387	20	0.40	R	1.8	20.76	R	0.00	2.3	60.0
			B	2.2	22.10	B - R	0.01	2.8	44.0
			U	1.9	21.57	U - R	0.01	2.4	33.0
NGC 4406	104.5	0.18	R	2.0	20.65	R	0.00	3.0	175.0
			B	2.1	22.36	B - R	0.01	3.2	158.8
			U	2.7	21.89	U - R	0.01	6.4	108.5
NGC 4472	114	0.20	R	2.0	20.40	R	0.01	3.0	172.0
			B	2.3	22.05	B - R	0.01	3.9	156.0
			U	2.9	21.43	U - R	0.01	7.0	155.3
NGC 4478	15.5	0.20	R	1.9	20.95	R	0.00	3.1	69.3
			B	2.0	22.47	B - R	0.02	3.3	57.7
			U	2.3	22.08	U - R	0.02	3.9	43.5
NGC 4486	110	0.03	R	2.5	20.19	R	0.00	4.3	163.0
			B	2.5	22.06	B - R	0.01	4.3	148.0
			U	2.5	21.40	U - R	0.01	4.3	147.8
NGC 4551	21	0.26	R	1.8	20.70	R	0.00	2.7	57.8
			B	1.8	22.30	B - R	0.01	2.7	43.5
			U	2.2	21.96	U - R	0.01	3.3	39.2
NGC 4636	117	0.05	R	2.1	20.43	R	0.00	3.5	166.0
			B	2.4	21.81	B - R	0.01	4.0	165.3
			U	2.9	21.04	U - R	0.01	6.7	102.6
NGC 4649	82	0.15	R	2.0	20.29	R	0.00	3 .1	185.0
			B	2.4	21.76	B - R	0.01	4.8	167.8
			U	2.9	20.92	U - R	0.01	7.0	104.2
NGC 4697	94.5	0.39	R	1.7	20.37	R	0.00	2.2	188.0
			B	2.2	21.89	B - R	0.02	5.6	153.1
			U	2.2	21.51	U - R	0.02	5.6	126.5
NGC 4874	66.5	0.07	R	2.1	20.67	R	0.02	3.4	91.8
			B	2.1	22.52	B - R	0.10	3.4	51.8
			U	2.1	22.12	U - R	0.07	3.4	35.4
NGC 4889	39	0.35	R	2.7	20.54	R	0.02	3.6	122.2
			B	2.5	22.25	B - R	0.10	3.6	75.8
			U	2.7	21.83	U - R	0.07	3.6	51.8
NGC 5638	29.5	0.10	R	1.7	21.07	R	0.00	2.8	80.0
			B	2.0	21.59	B - R	0.02	3.4	54.0
			U	2.2	21.20	U - R	0.02	4.0	49.1
NGC 5813	56	0.23	R	1.9	20.85	R	0.02	2 .8	173.0

Table 2.3: Seeing, background and cutoff radii

Galaxy	r_e	ϵ	Band	Seeing	Sky	Profile	Ext. + K	Inner	Outer
	"	at 10"		"			Correction	Cutoff	Cutoff
(1)	(2)	(3)	(4)	(5)	(6)	(7)	(8)	(9)	(10)
			B	1.9	22.28	B - R	0.04	2.8	122.2
			U	2.0	21.79	U - R	0.05	2.9	76.0
NGC 5831	28	0.28	R	1.7	20.71	R	0.02	2.4	91.8
			B	1.8	22.09	B - R	0.04	2.6	58.5
			U	2.0	21.84	U - R	0.05	2.9	48.4
NGC 5845	4.55	0.35	R	1.6	20.76	R	0.03	2.4	36.1
			B	1.6	22.33	B - R	0.04	2.4	27.1
			U	2.3	21.94	U - R	0.04	3.7	20.4
IC 1101	114.5	0.44	R	2.1	21.06	R	0.08	2.5	76.0
			B	2.2	22.61	B - R	0.30	2.7	30.1
			U	1.8	22.09	U - R	0.23	4.1	27.4
NGC 6051	25.5	0.29	R	2.0	20.95	R	0.06	2.9	60.0
			B	2.1	22.56	B - R	0.15	3.0	55.0
			U	2.3	21.91	U - R	0.13	3.3	33.5
NGC 6086	25	0.30	R	1.6	21.19	R	0.06	2.2	92.0
			B	1.5	22.55	B - R	0.15	2.2	47.1
			U	1.5	21.98	U - R	0.13	2.2	26.6
NGC 6269	47.5*	0.25	R	2.2	20.77	R	0.08	3.2	85.1
			B	2.6	22.18	B - R	0.18	4.4	48.0
			U	1.5	21.49	U - R	0.17	6.2	24.6
NGC 7626	41.5	0.12	R	2.0	20.23	R	0.04	3.2	91.8
			B	2.1	21.99	B - R	0.04	3.4	62.7
			U	2.1	21.19	U - R	0.03	3.4	38.9

Notes to Table 2.3:
Column (2) gives the effective radius from Burstein *et al.*(1987), and where indicated by *, from the RC2. The Burstein *et al.*value has been transformed to major axis effective radii, using ellipticities in column (3) that were measured from the data. Column (5) lists the FWHM of the seeing in arcseconds, and column (6) the surface brightness of the sky in mag arcsec^{-2}. Column (8) gives the correction for galactic extinction and redshift together, applied to the R, B-R and U-R profiles. Columns (9) and (10) list the inner and outer cutoff radius used in the tabulation and presentation of the data. These radii were derived from the measured seeing and sky background level, as discussed in the text.

For a few galaxies the data were of poor quality and/or the galaxy was limited by the frame size to higher surface brightnesses than normally used for the cutoff. For these we truncated the profiles at the outer radii shown below:

Galaxy	Color cutoff (% of sky)	Outer cutoff (% of sky)
NGC 1600	15	10
NGC 4261	20	10
NGC 4406	20	10
NGC 4874	20	10

Palomar Sky Survey for $\approx$ 20 galaxies using the Sony measuring machine at the Sterrewacht, Leiden. The scale ratios on the 0.9-m between the different bands were

$$U/R = 1.0013 \pm 0.0013, \quad B/R = 1.0000 \pm 0.0010.$$

On the 2.1-m telescope the ratios were

$$U/R = 1.0002 \pm 0.0063, \quad B/R = 1.0004 \pm 0.0012.$$

We used absolute scales of 0.86″ per pixel on the 0.9-m and determined a scale ratio of 2.265 between the 0.9-m and 2.1-m telescopes, giving 0.38″ pixels on the 2.1-m.

We found small, but systematic offsets in position angle for the same galaxy observed during different runs. These differences were typically 1-2°, but were sometimes 4-5°. We attribute these differences to small changes from run to run in the orientation of the dewar on the telescope. By measuring stars on the CCD frames and on the Palomar Sky Survey plates all position angle measurements have been corrected and are given from North through East.

To provide an absolute calibration for the profiles (i.e., to transform CCD counts to magnitudes on the Cousins UBR$_C$ system), we used published aperture photometry from Burstein *et al.* (1987) for 30 galaxies and the catalogs of Longo and De Vaucouleurs (1983, 1985) for the remainder. The data used from the latter catalogs came primarily from Sandage and Visvanathan (1978) and Persson, Frogel and Aaronson (1979). The transformations used are given in Paper I. For IC 1101 no published aperture photometry was available in any band, nor for NGC 2778 and NGC 5845 in U, and so we used the calibration from other galaxies that were observed on the same night. For galaxies for which the Burstein *et al.* tabulated colors are given as $V - R_J$, we derived $V - R_C$ values by using the transformation

$$V - R_C = 0.73(V - R_J) - 0.03$$

from Bessell (1979). For galaxies for which $V - R$ was not available, we used the mean $(V - R_J) - (B - V)$ relation for ellipticals from Burstein *et al.* and the transformation above to give

$$V - R_C = 0.613(B - V) + 0.021.$$

From the scatter in the aperture measures for individual galaxies we estimate that this transformation did not introduce errors larger than 0.03 mag. From the internal scatter in the aperture measurements, we estimate that an accuracy of the zero-point of ± 0.1 mag in U,B and R is realistic. Since our main goal is to measure luminosity and color profiles, an accurate zero-point is desirable, but not essential.

Galactic extinction and K-corrections were dealt with in the same way as described in paper I. Reddening corrections (from Persson *et al.*, 1979) are of the form $A_V = 0.1\ (cosec|b| - 1)$ $(b < 50°)$, $A_V = 3.05\ E_{B-V}$, $E_{U-V} = 1.71\ E_{B-V}$, and $E_{V-R} = 0.80\ E_{B-V}$. The K-corrections (from Whitford, 1971) were determined from $\Delta V = 2z$, $\Delta(U - V) = 2z$, $\Delta(B - V) = 3z$, and $\Delta(V - R) = -z$, where z is the redshift of the galaxy.

2.4 Seeing Simulations

Previous studies of the effects of seeing on galaxy profiles (Schweizer, 1979, 1981, Djorgovski, 1983, Lauer, 1985) have emphasized the way in which seeing modifies core parameters. The goal of these studies has been to derive the true parameter values by generating corrections to the seeing-convolved parameters. The seeing in our data was generally not good enough to make such an approach fruitful. Here we investigate the effects of seeing on the profiles to establish the radius beyond which they are accurate (until sky errors become a major factor). We simulated galaxies with a De Vaucouleurs $r^{1/4}$-law luminosity profile and a range of constant ellipticities to determine the radii beyond which the error due to seeing is $\Delta m < 0.05$ mag for the luminosity and color profiles, and beyond which the ellipticity error $\Delta\epsilon < 0.02$. Elliptical galaxies are rarely as centrally concentrated as an $r^{1/4}$-law, and so this approach is likely to generate a conservative (upper limit) radius beyond which the profile should be accurate to the above tolerances. The simulated images were convolved with Gaussian seeing profiles covering the range of seeing-to-galaxy length-scale ratios present in the data. A seeing profile with exponential wings (as in Schweizer, 1979) was also tried and produced results which were rather similar; the effects of different point spread functions (PSFs) have been explored by the authors quoted above.

PROF was run on these simulation frames to measure luminosity and ellipticity profiles. These were then compared with the original profiles to assess the effect of seeing on the luminosity profile. Comparisons between profiles measured from galaxy models convolved with different seeing values were made to assess the effect of seeing on the color profiles. We assumed no intrinsic color gradient for the purposes of this simulation. This assumption is reasonable since the magnitude of the color gradients, even over a factor 10 in radius, is small. Seeing redistributes the light in the center of the galaxy from small radii to larger radii, reducing the central surface brightness and correspondingly increasing the surface brightness at intermediate radii, beyond which the profiles become identical. We then measured the major axis radius beyond which the difference between the original and the seeing-convolved profiles was smaller than the above limits (i.e., $\Delta m < 0.05$ mag and $\Delta\epsilon < 0.02$).

The results can be seen in Figs 2.4a, 2.4b and 2.4c. The radii at which the effects of seeing become less than the adopted limits of $\Delta\epsilon = 0.02$, $\Delta m_L = 0.05$ and $\Delta m_C = 0.05$ are plotted against the seeing. Both the radii and the seeing are normalized by the galaxies effective radius r_e. D_S is the seeing FWHM in 4a and 4b, and the smaller of the two seeing FWHM in Fig. 2.4c, while D_L is the larger of the seeing FWHM. D_e is the effective diameter (twice the effective radius along the major axis). The radius cutoffs are shown for a range of ellipticities. These figures demonstrate that:

1. The *major axis* luminosity-profiles are affected more by seeing when the ellipticity is low than when the ellipticity is high. This is because there is less light off the major axis in an elongated galaxy than in circular one, to 'contaminate' the light on the major axis.

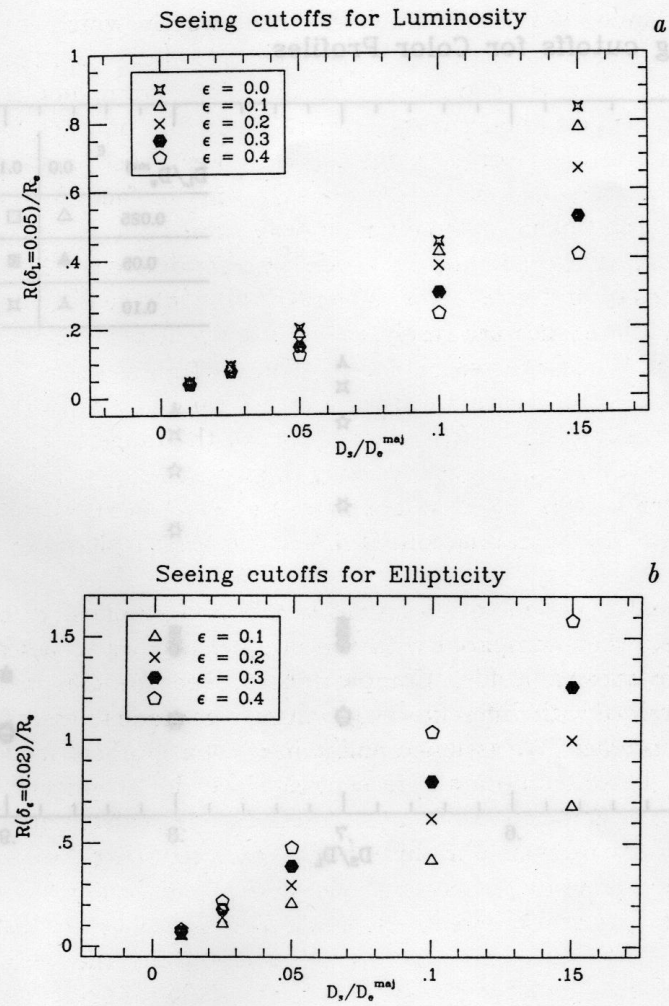

Figure 2.4: *Seeing cutoffs from simulations where model galaxies were convolved with Gaussian seeing point spread functions (PSFs) for a range of ellipticities* ϵ. *The cutoff radii are normalized to* r_e *and are determined to be those beyond which the error from seeing effects on a* $r^{1/4}$*-law profile are (2.4a)* < 0.05 *mag in the surface brightness profile, (2.4b)* < 0.02 *in the ellipticity, and (2.4c)* < 0.05 *mag in the color profile.* D_S *is the seeing PSF FWHM in 2.4a and 2.4b, and the smaller of the two seeing FWHM in 2.4c, while* D_L *is the FWHM of the larger seeing PSF.* D_e *is the effective diameter (twice the effective radius* r_e *along the major axis).*

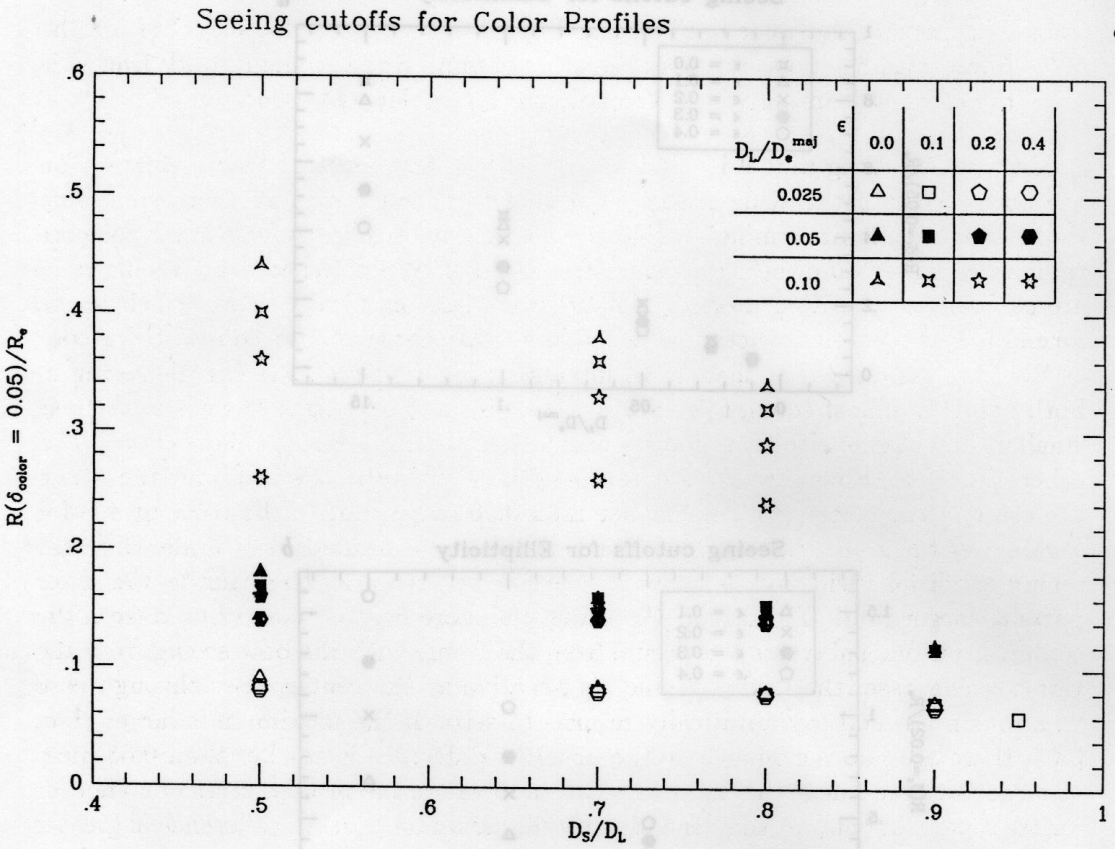

Figure 2.4: *Seeing cutoff for the color profile (2.4c). See also the caption for Fig. 2.4a*

2. Ellipticity profiles are affected more when the ellipticity is high. The radial extent over which seeing affects the ellipticity is much larger than we had expected.

3. The error in the color profile caused by seeing arises predominantly from the frame with the poorer seeing; the error is small if the seeing in both frames is the same, but initially varies rapidly as D_S/D_L decreases from unity.

If we take a King model instead of an $r^{1/4}$-law, the effect of seeing depends on the core radius of the King model. For core radii much smaller than the seeing radius, the results are similar to that for an $r^{1/4}$-law profile. As expected, for core radii much larger than the seeing any effect is small. When the core and seeing radii are comparable the King model fit is perturbed less than the $r^{1/4}$-law fit, since the former is less centrally concentrated and less light is available to be redistributed.

We have assumed that there is no intrinsic color gradient. Then, if the seeing in both bands is almost equal, the error resulting from the seeing in the color profile is smaller than that in either luminosity profile, because both errors almost cancel each other. For this reason, we have determined independently the radii outside which the error in the color profile is smaller than 0.05 magnitudes. The color profile for a galaxy with no intrinsic color gradient derived from frames taken under different seeing conditions will not be constant. Seeing redistributes the light in the inner parts to larger radii. The larger the seeing, the more light is redistributed from the center. So if one subtracts the profile from the frame with the best seeing from the worst seeing case, the "color profile" is negative at the center, rises through zero to a maximum and asymptotically returns to zero. If the maximum is larger than 0.05, there are two regions where the absolute difference is smaller than 0.05 mag: at large radii, and near the point at small radii where the profiles cross one another before separating at still smaller radii. If the maximum positive difference is greater than our chosen tolerance, namely 0.05 magnitudes, there will be two points where the locus of the difference crosses the value +0.05 and one, at a small radius, where the locus crosses the value -0.05 magnitudes.

In Fig. 2.4c, we show the radius beyond which the luminosity profile of the frame with the poorer seeing is less than 0.05 magnitudes brighter than the frame with the better seeing. We have used only the most conservative prescription in generating Fig. 2.4c, so that once the maximum positive difference falls below 0.05 magnitudes, no symbol is plotted. Note that for round galaxies the plotted radius is larger than for flattened ones. For galaxies with non-zero color gradients, the error in the color profile will not converge to zero if both seeings are equal.

We applied the results from these simulations to our galaxies, and determined the radius beyond which the profiles were essentially unaffected by seeing. The effective diameters needed for this were taken from Burstein *et al.* (1987), and converted to major-axis effective diameters. The central ellipticity was taken to be that at $\approx 10''$, beyond the worst effects of the seeing. In Table 2.3 we present this ellipticity and the effective radii. With these values and our seeing estimates we determined the inner cutoff-radii for the surface brightness, ellipticity and the color profiles by

interpolating across the values from the simulations. To avoid large errors caused by interpolating near $D_S/D_e = 0$, effective diameters larger than 100″ were truncated to 100″ . The radial cutoffs determined from the simulations have been applied to the final tabulated and plotted data in Table 2.9 and Figure 2.17 in Appendix A.

The simulations show that the ellipticity is significantly affected by seeing out to quite large radii. As a result we have tabulated values for the ellipticity from half the inner cutoff radius determined from the simulations. For some highly flattened galaxies the ellipticity appears to decrease in the center. For example, in NGC 3377 and NGC 4697 the ellipticity decreases monotonically at radii less than 10 arcseconds. The simulations show that this entire effect can be attributed to the seeing and that the data are consistent with the ellipticity remaining constant at the value observed at radii greater than 10 arcseconds (see Fig. 2.5). We caution the reader that the ellipticities are accurate to 0.02 only beyond radii that are twice as large as that for the first ϵ value in Table 2.7. The error in the position angle increases $\propto 1/\epsilon$ as the ellipticity tends to zero, and so can become very large (an example of a galaxy subject to this effect would be NGC 4486).

Franx, Illingworth and Heckman (1989b) give analytic formulas for errors in the photometric parameters, calculated by using a few terms of the Taylor expansion of the intensity profile that is convolved with a non-circular seeing profile. They note, in particular, the effect of a non-circularly symmetric seeing point-spread function on the position angles for round galaxies. Their main conclusions agree with the results of our simulations.

2.5 Results and Comparisons with other Studies

The results from this program are shown and tabulated fully in Appendix A. The R-band surface brightness profile plus the ellipticity and major axis position angle profiles in U, B and R, as well as the $B-R$ and $U-R$ color gradients, are tabulated (Table 2.9) and plotted (Figure 2.17) there for each of the 39 galaxies in our sample. In addition, the sin and cos 3θ and 4θ terms are also plotted in Figure 2.17. Specific comments on individual galaxies are given in Appendix B for characteristics that are distinct from the norm.

In order to characterise the properties of these galaxies from the surface photometry, we have calculated 'effective' or 'characteristic' parameters for each galaxy. We have derived logarithmic gradients for the color, ellipticity and position angle profiles, i.e., we have made a linear regression of these parameters on the logarithm of the radius. We have used all the data values within the inner and outer cutoff radii. The colour profiles are well represented by a linear fit against log radius, and so can be characterised quite accurately by such a relation. This is less true of the ellipticity and position angle profiles. However, the logarithmic gradients of ϵ and θ are a useful characterisation for the purpose of correlations between the parameters and so are given here. The limitation of such a representation should be kept in mind. The gradients are weighted somewhat towards changes near the core, since

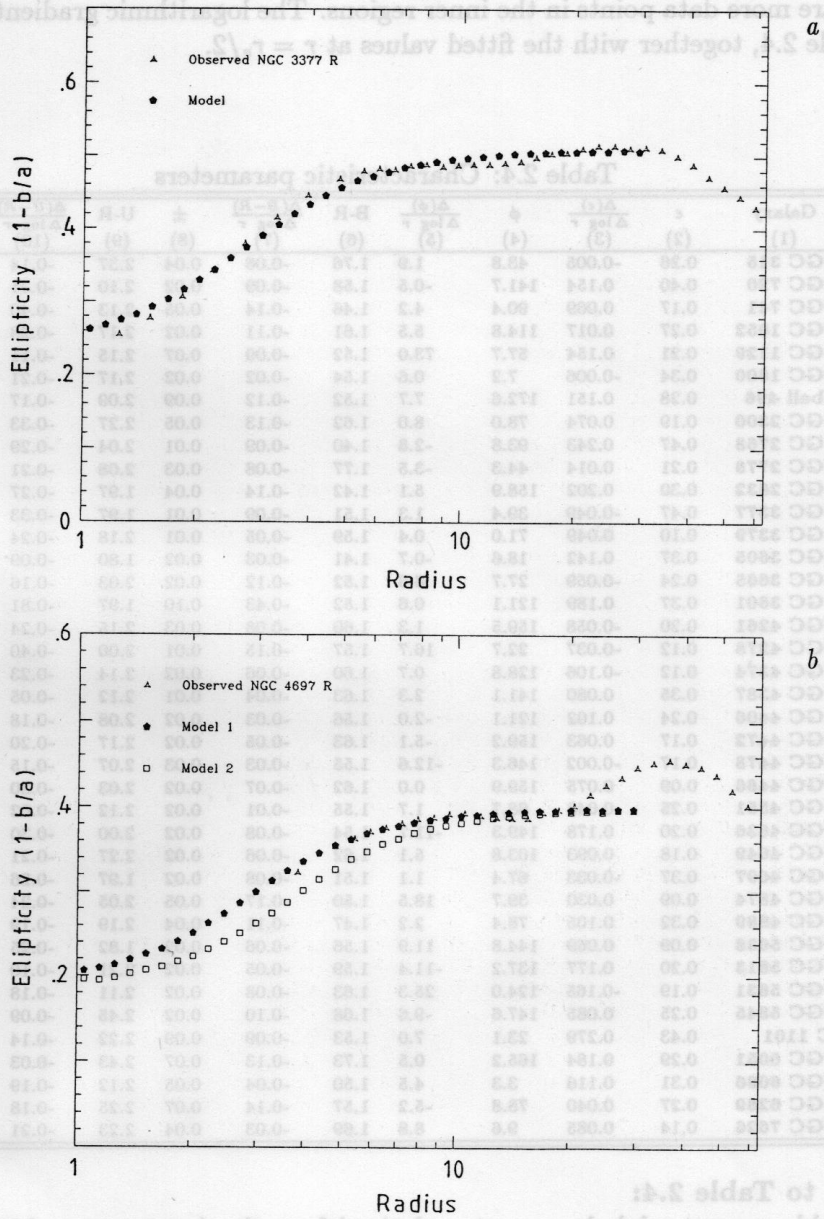

Figure 2.5: *Ellipticity profiles for NGC 3377 (2.5a) and NGC 4697 (2.5b) in R. No radius cutoffs have been applied. Model profiles are overlaid. They are derived from a galaxy with a De Vaucouleurs luminosity profile and a fixed ellipticity, convolved with circular Gaussian seeing. For the effective radii we took the values from Table 2.3 for NGC 3377 and for model 1 for NGC 4697, and set $r_e = 50''$ for NGC 4697 for model 2. The figure shows that the decrease in the ellipticity into the core is consistent with a constant ellipticity profile degraded by the seeing.*

there are more data points in the inner regions. The logarithmic gradients are given in Table 2.4, together with the fitted values at $r = r_e/2$.

Table 2.4: Characteristic parameters

Galaxy	ϵ	$\frac{\Delta(\epsilon)}{\Delta \log r}$	ϕ	$\frac{\Delta(\phi)}{\Delta \log r}$	B-R	$\frac{\Delta(B-R)}{\Delta \log r}$	$\pm$	U-R	$\frac{\Delta(U-R)}{\Delta \log r}$	$\pm$
(1)	(2)	(3)	(4)	(5)	(6)	(7)	(8)	(9)	(10)	(11)
NGC 315	0.26	-0.005	43.8	1.9	1.76	-0.06	0.04	2.37	-0.14	0.09
NGC 720	0.40	0.154	141.7	-0.5	1.58	-0.09	0.02	2.10	-0.31	0.05
NGC 741	0.17	0.069	90.4	4.2	1.46	-0.14	0.05	2.13	-0.40	0.16
NGC 1052	0.27	0.017	114.8	5.5	1.61	-0.11	0.02	2.17	-0.28	0.02
NGC 1129	0.21	0.154	57.7	73.0	1.52	-0.09	0.07	2.15	-0.11	0.06
NGC 1600	0.34	-0.006	7.2	0.6	1.54	-0.02	0.02	2.17	-0.21	0.06
Abell 496	0.28	0.151	172.6	7.7	1.52	-0.12	0.09	2.09	-0.17	0.10
NGC 2300	0.19	0.074	78.0	8.0	1.62	-0.13	0.05	2.27	-0.33	0.12
NGC 2768	0.47	0.243	93.8	-2.8	1.40	-0.09	0.01	2.04	-0.29	0.06
NGC 2778	0.21	0.014	44.3	-3.5	1.77	-0.08	0.03	2.08	-0.21	0.03
NGC 2832	0.30	0.202	158.9	5.1	1.42	-0.14	0.04	1.97	-0.27	0.05
NGC 3377	0.47	-0.049	39.4	1.3	1.51	-0.09	0.01	1.97	-0.33	0.03
NGC 3379	0.10	0.049	71.0	0.4	1.59	-0.05	0.01	2.18	-0.24	0.01
NGC 3605	0.37	0.142	18.6	-0.7	1.41	-0.03	0.02	1.80	-0.09	0.04
NGC 3665	0.24	-0.059	27.7	6.6	1.52	-0.12	0.02	2.03	-0.16	0.03
NGC 3801	0.37	0.189	121.1	0.6	1.52	-0.43	0.10	1.97	-0.81	0.15
NGC 4261	0.20	-0.058	159.5	1.3	1.60	-0.08	0.03	2.15	-0.24	0.05
NGC 4278	0.12	-0.037	22.7	16.7	1.57	-0.15	0.01	2.00	-0.40	0.05
NGC 4374	0.12	-0.106	128.8	0.7	1.60	-0.06	0.02	2.14	-0.23	0.01
NGC 4387	0.35	0.080	141.1	2.3	1.63	-0.04	0.01	2.12	-0.05	0.02
NGC 4406	0.24	0.102	121.1	-2.0	1.56	-0.03	0.02	2.08	-0.18	0.02
NGC 4472	0.17	0.063	159.2	-5.1	1.63	-0.05	0.02	2.17	-0.20	0.04
NGC 4478	0.17	-0.002	146.3	-12.6	1.55	-0.03	0.03	2.07	-0.15	0.05
NGC 4486	0.09	0.075	159.9	0.0	1.62	-0.07	0.02	2.03	-0.30	0.05
NGC 4551	0.25	0.048	68.7	1.7	1.55	-0.01	0.02	2.12	-0.02	0.02
NGC 4636	0.20	0.178	149.3	-11.7	1.54	-0.08	0.02	2.00	-0.30	0.05
NGC 4649	0.18	0.093	103.8	5.1	1.62	-0.06	0.02	2.27	-0.21	0.03
NGC 4697	0.37	-0.033	67.4	1.1	1.51	-0.08	0.02	1.97	-0.26	0.04
NGC 4874	0.09	0.030	39.7	18.5	1.50	-0.17	0.05	2.05	-0.24	0.07
NGC 4889	0.32	0.105	78.4	2.2	1.47	-0.11	0.04	2.19	-0.19	0.04
NGC 5638	0.09	0.069	144.8	11.9	1.56	-0.06	0.02	1.82	-0.25	0.05
NGC 5813	0.20	0.177	137.2	-11.4	1.59	-0.05	0.02	2.21	-0.10	0.03
NGC 5831	0.19	-0.165	124.0	25.3	1.63	-0.08	0.02	2.11	-0.18	0.03
NGC 5845	0.25	0.085	147.6	-9.6	1.68	-0.10	0.02	2.45	-0.09	0.02
IC 1101	0.43	0.279	23.1	7.0	1.53	-0.09	0.09	2.22	-0.14	0.11
NGC 6051	0.29	0.184	165.2	0.5	1.73	-0.13	0.07	2.43	-0.03	0.05
NGC 6086	0.31	0.116	3.3	4.5	1.50	-0.04	0.05	2.12	-0.19	0.06
NGC 6269	0.27	0.040	78.8	-5.2	1.57	-0.14	0.07	2.25	-0.18	0.12
NGC 7626	0.14	0.085	9.6	8.8	1.69	-0.03	0.04	2.23	-0.21	0.07

Notes to Table 2.4:

This table presents global parameters derived from the data presented in Table 2.9. We have fitted linear relations to ellipticity, position angle, $B - R$ and $U - R$ as a function of the logarithm of radius. The slope and intercept of these logarithmic gradients are given, with the intercepts being derived for $r=r_e/2$. In columns (2) and (3) we present the fits for the ellipticity $1 - b/a$, in columns (4) and (5) those for the position angle of the major axis, in columns (6),(7) and (8) the logarithmic gradient for the $B - R$ color, and in columns (9),(10) and (11) that for the $U - R$ color gradient. The color gradients are given in mag arcsec^{-2} per dex in radius.

2.5.1 Comparison with other Studies: Luminosity Profiles and Isophote Shapes

The surface photometry of the three galaxies presented in Paper I was compared extensively with the results of other authors to establish the validity of the techniques used. For this sample we have chosen not to compare our results with all the available surface photometry in the literature, but only with a number of studies that present large bodies of data. We have compared our results with those of King (1978, hereafter KI), Michard (1985, MI), Kent (1984, KE), Djorgovski (1985, hereafter DJ), Lauer (1985, LA), and Jedrzejewski (1987, JE); the first two authors worked with photographic data, while the last four authors used CCDs. The comparisons were made between the major axis surface brightness profiles using our data in the band closest to the above author's published band. DJ and LA used an R band with a larger effective wavelength than used by us; KE used the Gunn r band, which is narrower than Cousins R, but has the same effective wavelength. JE worked in Johnson B and R. We have compared the photographic magnitudes of KI and MI with our B measurements. The bands were sufficiently close and the color gradients in ellipticals small enough that no corrections were necessary before comparison. The magnitude of the zero point differences due to the use of Cousins system instead of the Johnson system can be derived from the transformation given in Paper I, i.e.,

$$R_J = R_C - 0.12(B-R)_C - 0.07.$$

For comparison with the KI and MI data we corrected our profiles to correspond to their 45° profiles.

The comparisons in B are shown in Fig. 2.6a and those in R are shown in Fig. 2.6b.

Some aspects of these comparisons are noteworthy. In the R-band, agreement with LA and KE is excellent; any trend present in the data appears to be ≤ 0.1 mag arcsec^{-2} over the radial extent of the data. The sense of the differences is random, and the zero points are different in a way that is consistent with the different filter combinations used. The R data of JE exhibit surface brightness gradients which are systematically less steep than our profiles; his galaxies always appear too bright in the outer parts. The effect is unlike that expected from a systematic error in sky background level, since it extends smoothly to small radii. The R differences are also too large to be caused by the different R filter. We have performed a linear regression on the difference profile in magnitudes as a function of log radius (excluding the three galaxies where the difference does appear to be due to uncertainties in the sky, i.e., NGC 3377, NGC 5638 and NGC 5845), and find a systematically smaller gradient in the JE data of 0.07 ± 0.01 mag per dex in radius. In B the agreement with JE is good; the regression yields a formally insignificant result.

The data of DJ were obtained using the same equipment as the data of LA, but extend to larger radii. In general, DJ reports fainter surface brightnesses than both we and LA find at these large radii. It seams likely that the sky background values of many of the galaxies reported by DJ have been overestimated. In many cases the galaxies filled the field of his CCD, which could have led him to overestimate the

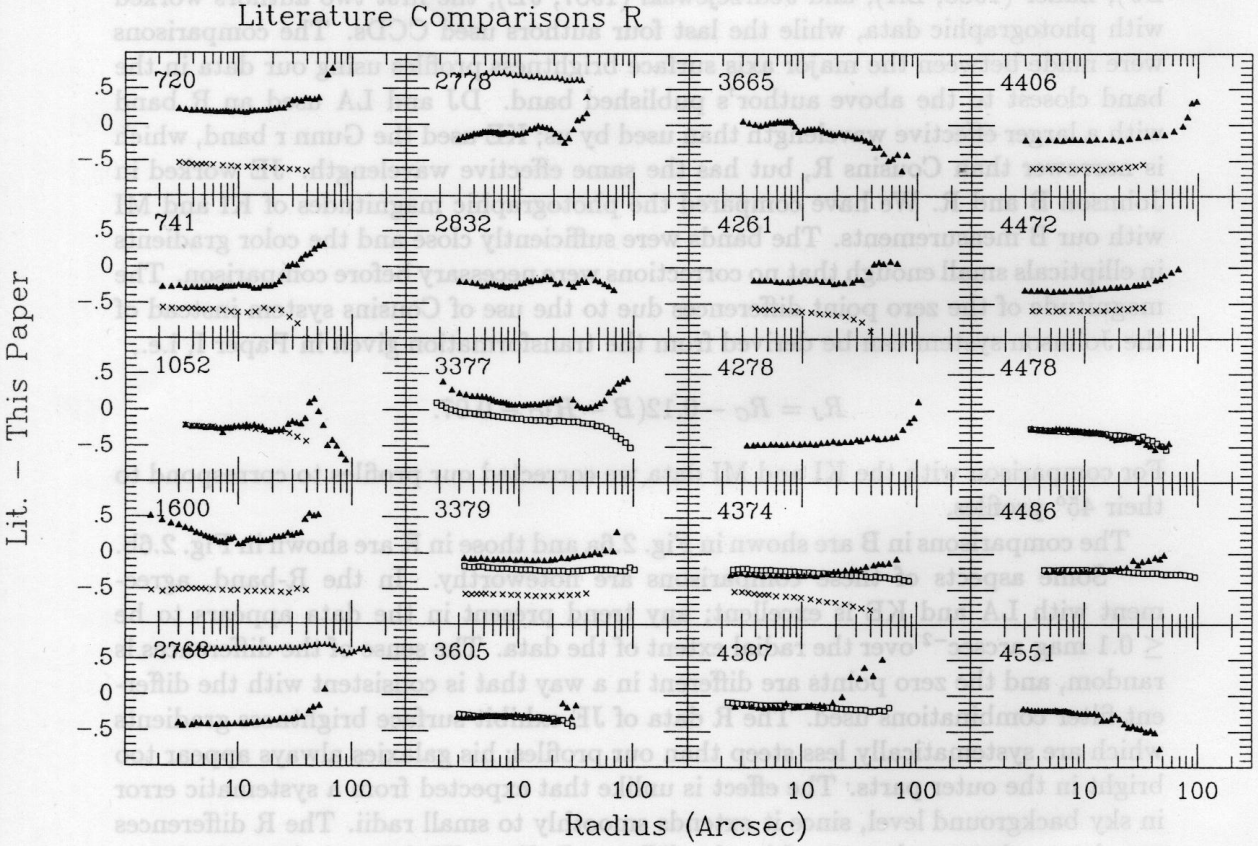

Figure 2.6: *Comparisons with other authors over the range defined by our cutoff radii. The sources corresponding to the symbols are: open pentagons - (King, 1978); open squares - (Jedrzejewski, 1987); open triangles - (Kent, 1984); filled squares - (Michard, 1985); filled triangles - (Djorgovski, 1985); crosses - (Lauer, 1985). Corrections have not been applied for zero-point differences.*

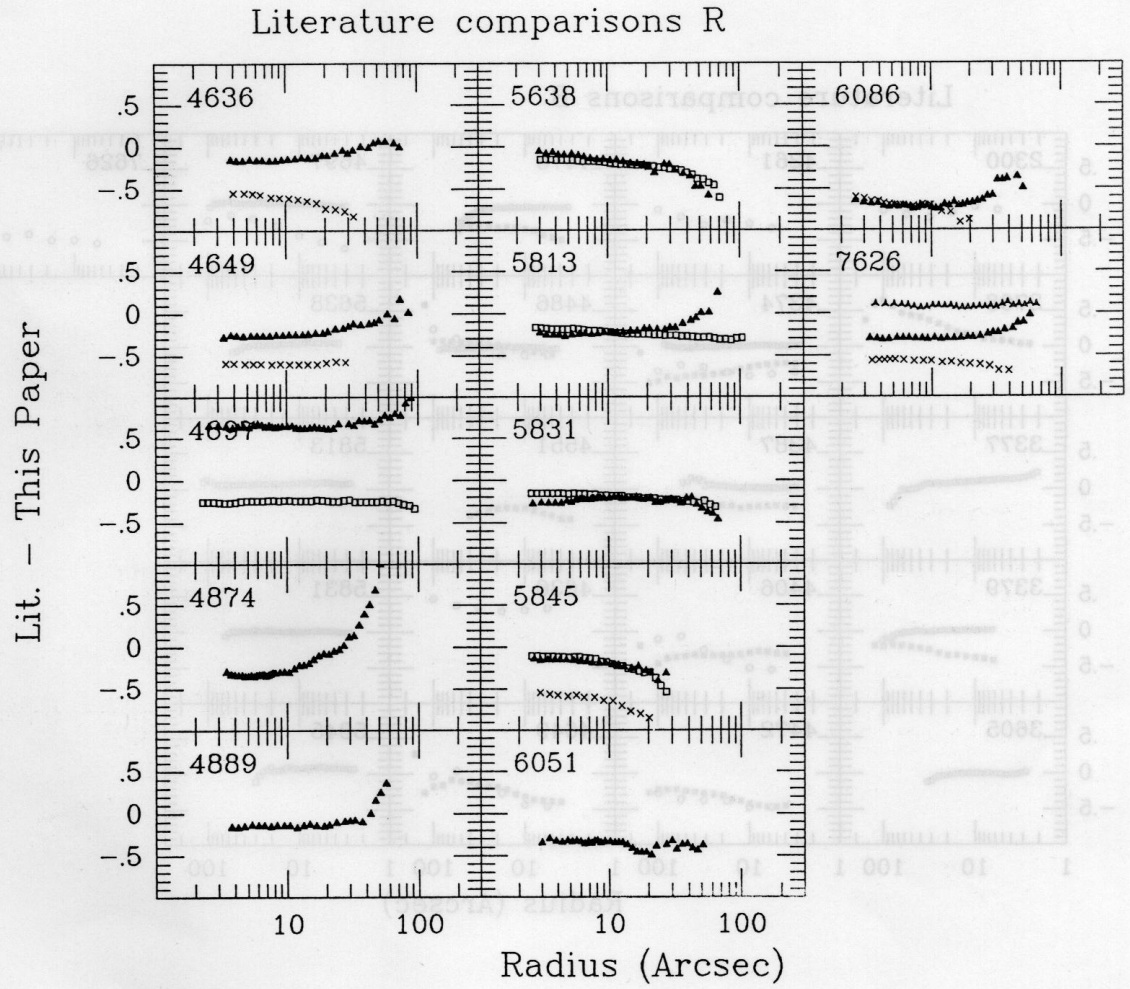

Figure 2.6: *Continued.*

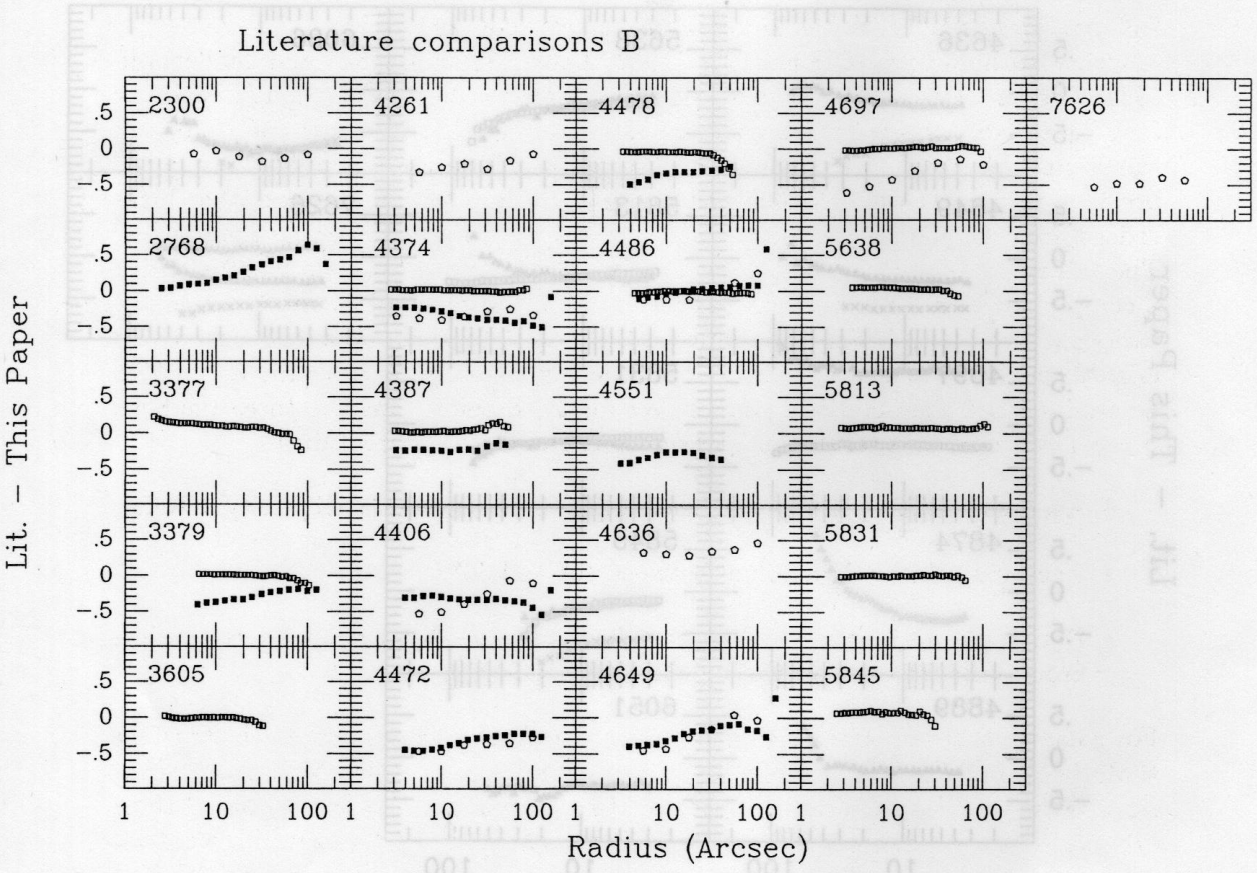

Figure 2.6: *Continued.*

brightness of the sky. In this case, one might expect the most discrepant galaxies to be the large ones, and the smaller ones to be in better agreement; this does not appear to be uniformly true. With the exception of NGC 2768, for which there is a large difference with the data of MI, the comparisons with KI and MI show that our respective data sets agree well. The problem with NGC 2768 may be due to its large ellipticity and the derivation of the 45° profile in the presence of large quantities of dust.

The ellipticity and position angle profiles generally agree quite well. The differences with LA, for example, are small, usually being within 0.02 and 2°, respectively. Differences with DJ are often larger, and systematic in a few cases.

Other authors (e.g., Carter, 1978, 1987; Lauer, 1985; Bender and Möllenhoff, 1987; Bender *et al.*, 1988) have also derived higher order terms, though typically they have taken a more limited approach and have just derived the cos 4θ-term, and sometimes the cos 3θ-term. Our sin and cos $n\theta$ profiles agree well with those in the previous references. To determine characteristic values for C4 and the other high-order terms (C3, S3, S4) for each galaxy, we have tried a few different approaches. The values were determined separately for the B and for the R data sets, after which a comparison was made between the results from the two bands, and between the various approaches. Differences between the results from the R and B data could arise through the presence of dust, or because of the way in which the algorithms determined the characteristic values. We found, though, that the three methods below gave consistent results for galaxies that had little apparent dust:

- Averaging all the data values between the inner and outer ellipticity cutoffs;
- Averaging all the data values between 10″ and 30″ ;
- Deriving a peak value (in fact, the absolute value) by averaging a few points around the maximum amplitude in each high-order term.

For galaxies that contained significant dust the profiles showed so much structure that these methods did not give very meaningful results. The high-order terms from these galaxies were not included in the subsequent analysis. While all three approaches gave consistent results, we decided to adopt the third method, since the values obtained were not a function of rather arbitrary observational limits. The final values are presented in Table 2.5. We have also tabulated the radius of the peak for the cos 4θ term (C4), since this is the term that has attracted the most interest because of its probable correlation with other properties of the galaxies.

The C4 values were compared with those from Bender *et al.* (1989). Figure 2.7 shows that the agreement is excellent. Bender *et al.* use a slightly different definition, with different normalization: if there is a maximum (or minimum), they select the peak value, as we do, but if the profile is monotonically increasing or decreasing, they take the value at one effective radius. However, for the 19 galaxies we have in common, only 2 have monotonically increasing or decreasing profiles. For this reason we would expect the C4-values to be the same, but on the average

Table 2.5: Effective higher order terms

Galaxy	C3	S3	C4	r_{C4}	S4
				"	
(1)	2	3	4	5	6
NGC 315	0.002	-0.001	-0.006	12	-0.002
NGC 720	0.002	-0.001	-0.003	12	-0.004
NGC 741	0.003	0.001	0.002	16	-0.002
NGC 1052	0.003	-0.002	0.000	10	-0.001
NGC 1129	-0.014	0.008	-0.008	22	-0.002
NGC 1600	-0.001	0.000	-0.015	11	-0.002
Abell 496	-0.007	-0.003	0.006	13	0.005
NGC 2300	0.006	0.003	0.011	38	0.003
NGC 2768	0.002	-0.001	0.006	48	0.005
NGC 2778	-0.001	-0.002	-0.003	22	0.000
NGC 2832	0.000	-0.008	-0.004	16	0.008
NGC 3377	0.007	0.002	0.019	6	-0.002
NGC 3379	-0.005	0.003	0.003	16	0.006
NGC 3605	0.002	0.002	-0.012	14	-0.004
NGC 3665	0.002	-0.003	-0.002	50	0.000
NGC 3801	-0.016	-0.012	-0.092	5	0.030
NGC 4261	0.003	-0.004	-0.019	11	0.005
NGC 4278	0.005	-0.011	0.000	–	-0.007
NGC 4374	0.003	0.000	-0.006	14	-0.002
NGC 4387	0.002	-0.001	-0.010	8	-0.005
NGC 4406	0.002	0.000	-0.010	17	-0.004
NGC 4472	-0.001	-0.003	-0.004	20	0.004
NGC 4478	0.002	-0.002	-0.015	25	0.013
NGC 4486	0.001	-0.002	0.001	–	0.001
NGC 4551	-0.003	0.002	-0.011	10	0.002
NGC 4636	-0.002	-0.002	-0.001	4	0.004
NGC 4649	0.004	0.004	-0.005	25	-0.006
NGC 4697	0.001	0.003	0.026	22	0.002
NGC 4874	0.010	0.004	-0.004	45	-0.012
NGC 4889	-0.001	0.001	-0.002	9	0.002
NGC 5638	0.000	0.000	0.001	–	-0.002
NGC 5813	0.002	0.002	0.001	30	-0.002
NGC 5831	0.002	0.001	0.008	16	-0.005
NGC 5845	0.006	-0.002	0.013	10	-0.006
IC 1101	-0.002	0.002	0.002	7	-0.002
NGC 6051	0.001	0.000	-0.002	7	0.002
NGC 6086	0.002	0.003	0.010	25	-0.005
NGC 6269	-0.002	-0.002	0.005	32	0.002
NGC 7626	-0.006	-0.005	0.004	6	0.004

Notes to Table 2.5:
In columns (2), (3), (4) and (6) we give the C3, S3, C4 and S4 terms, averaged as explained in the text. In column (5) we list the radius at which the maximum or minimum in C4 is reached.

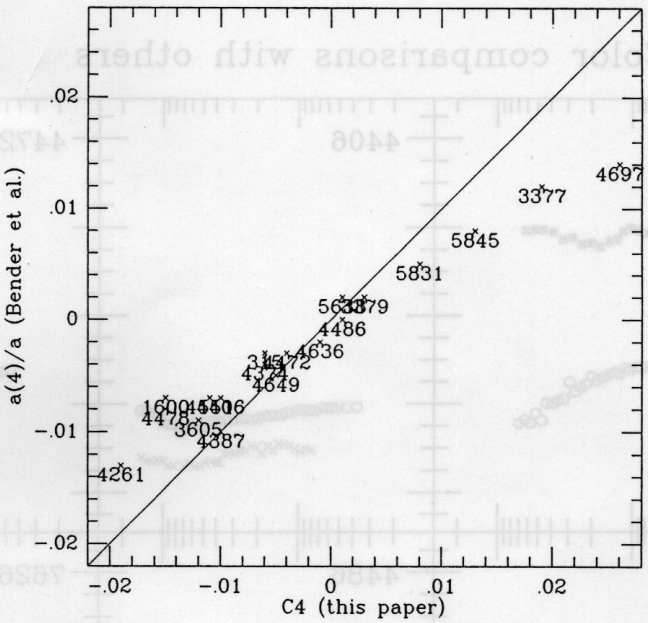

Figure 2.7: *A comparison between our C4 values and the a(4)/a parameter from Bender et al. (1988) for all those galaxies in common between the two samples.*

our C4-values are systematically larger by ≈40% than theirs. This is a result of the different normalization used.

We also show (§2.5.3) the high-order terms in a way that more clearly demonstrates what is happening to the isophotes in the galaxy. Instead of giving the values for C3 and S3, or C4 and S4, we plot the phase and amplitude of the deviations. Franx, Illingworth and Heckman (1989b) showed that such a representation makes it easier, in many cases, to understand the nature of the structure that contributes to the deviations from elliptical isophotes.

2.5.2 Comparison with other Studies: Color Gradients

A number of authors have published color gradients, usually for a small set of galaxies. A comparison with the color profiles of several authors is made in Fig. 2.8. The results are not encouraging. In general, the agreement is still not as good as one would like. However, the difficulty of measuring color changes of a few percent over a range in surface brightnesses of several decades should not be underestimated. In the mean, most authors with CCD data are consistent, finding small negative gradients in ellipticals, consistent with those found from the concentric aperture measures, and so the reality of gradients of this form is probably well-founded, even if individual cases should be treated with some scepticism. The advantage of the larger sensitivity of $U - R$ is apparent.

Boroson *et al.* (1983) determined color gradients in several bands for NGC 2300, 2768 and 4486 using the drift scan method on the Palomar 60-in telescope. Compar-

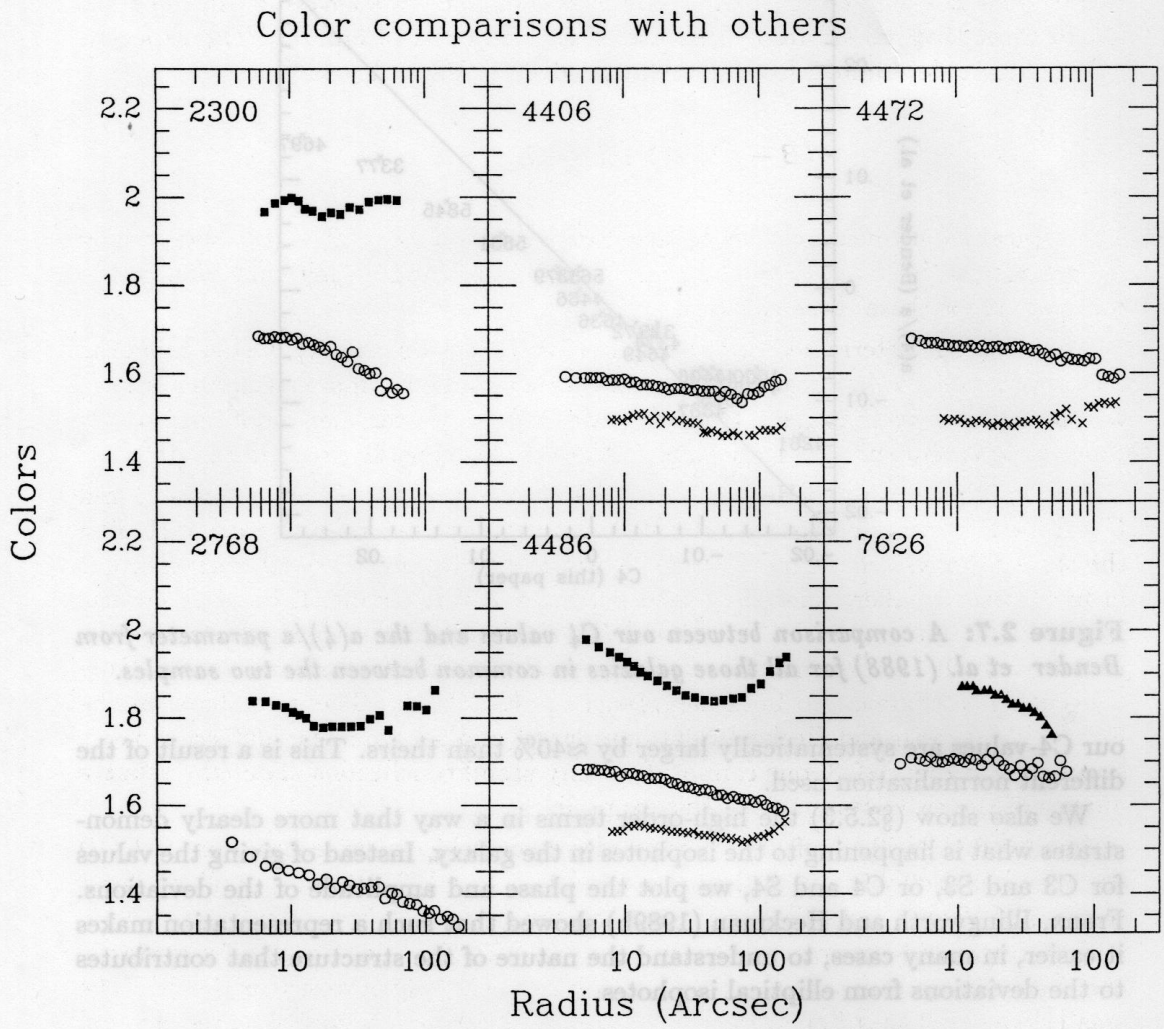

Figure 2.8: *Color gradient comparisons with other authors. The Boroson et al. (1983) $B-R_J$ data are shown as filled squares, the Franx, Illingworth and Heckman (1989b) $B-R_J$ data as filled triangles, and the Cohen (1986) $g-r$ data as crosses. We have added 1 to the g-r data from Cohen. No correction has been made for the zero point differences in the bands. The expected differences others − us are ≈0.25 mag for the Boroson, Thompson, and Shectman data and the Franx, Illingworth and Heckman data, and ≈-1.1 mag for the Cohen data. Our data have been plotted with open circles.*

ison of their $B - R_J$ gradients with ours shows that they are consistent in the sense of the offset that results from their use of R_J compared to our R_C. The expected offsets can be determined from the relation given in Paper I, i.e.,

$$(B - R)_J = 1.14(B - R)_C + 0.04.$$

The typical color difference should therefore be $(B - R)_J - (B - R)_C = 0.25$ mag for galaxies with $(B - R)_C = 1.6$, which is a little smaller than that seen in the comparison for these three galaxies.

Cohen (1986) determined color gradients for NGC 4406, 4472 and 4486 using the four-shooter on the Palomar 5 m. She finds small gradients in $g - r$ (Gunn system), which are broadly consistent with what we find. However, her data consistently show a slight reddening at large radii, unlike what is generally seen in our data.

Franx, Illingworth and Heckman (1989b) obtained color gradients in $B - R$ and $U - R$ for 17 southern elliptical galaxies, using the same general approach, including the same filter system. The range for which they have obtained color gradients is in most cases smaller, since they used detectors with a smaller field. The general trend they see is the same: $B - R$ and $U - R$ both become bluer with increasing radius, with the gradients in $U - R$ being much larger than those in $B - R$. Only one galaxy is common to both samples, i.e., NGC 7626. The error bars on the Franx, Illingworth and Heckman data are large, and so, while the difference looks significant in Figure 2.8, one cannot draw any useful conclusions about the relative quality of the two datasets from this example.

Bender and Möllenhoff (1987) have also undertaken a large program of CCD surface photometry in which they measured $V - I$ and $R - I$ color gradients for a number of Virgo ellipticals. They also find that ellipticals typically become bluer with radius, and have noted that structure occurs in the color profiles; for example, the change in slope in the color gradient in NGC 4472 (which we see in $B - R$). The small slopes that they find in their $V - I$ and $R - I$ profiles are similar to those found by us in $B - R$, as would be expected since the sensitivity to population/metallicity changes is comparable in these bands. Their results confirm the value of $U - R$ with its much enhanced sensitivity to metallicity and population changes.

Recently more color profiles have become available from Vigroux *et al.* (1988) in B and R, using CCD-photometry. In a paper interpreting these color gradients Vader *et al.* (1988) tabulate the color gradients they find in $B - R_J$ per decade in radius. In Figure 2.9 a comparison is made for the 9 galaxies we have in common. Our gradients have been converted to the Johnson system by multiplying them by a factor 1.14. The agreement is reasonably good; all points lie close to the line of equal gradients, except NGC 5638, for which Vader *et al.*'s gradient is much larger than the value we found. These authors do not fully take into account the effects of seeing. In addition, their estimate of the errors in the sky background determination are apparently too small. Together these effects, seeing and sky determination, could be responsible for the scatter in Fig. 2.9.

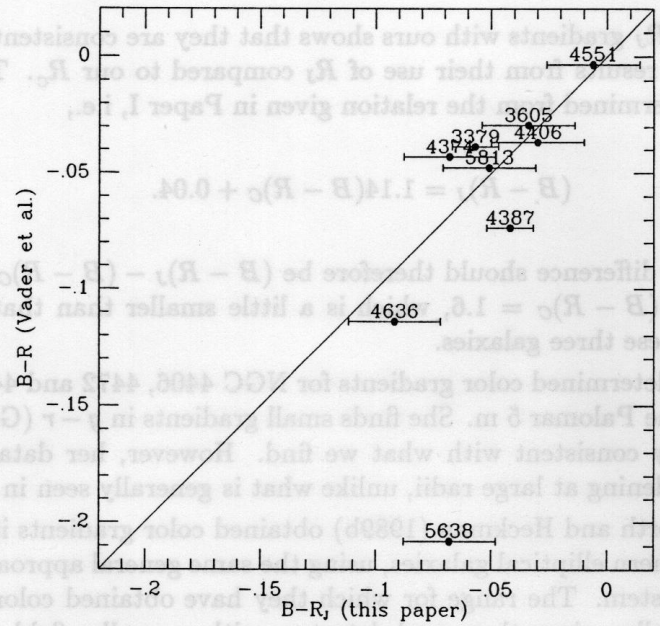

Figure 2.9: *A comparison of the logarithmic gradients in color in mag per decade in radius between Vader et al. (1988) and us. Our values have been transformed to the Johnson system.*

2.5.3 Deviations from Elliptical Isophotes

In general the isophotes of these galaxies are very close to ellipses. However, as noted by several authors (e.g., Carter, 1978; Lauer, 1985; Bender *et al.*, 1988) deviations are common at the 1% level. With rare exceptions, primarily of galaxies that contain substantial quantities of dust, the maximum deviations from ellipses are 1.5-2%, with 0.5% being a more typical value. Although small, the 3θ and 4θ terms given here are real; they agree between B and R, as well as with the results of other authors (e.g., Bender *et al.*, 1988).

While we have represented these deviations by the amplitudes of the cos and sin 3θ and 4θ terms (those tabulated in Table 2.9 and plotted in Figure 2.17) another representation, as shown by Franx, Illingworth and Heckman (1989b), may also prove more useful for understanding the structure(s) that contribute to the deviations from ellipses. Phases and amplitudes of 3-fold and 4-fold symmetry, i.e., the 3θ and 4θ terms, are plotted instead of the cos and sin terms. As Franx, Illingworth and Heckman also noted, some of these features occur at fixed position angles, even in galaxies whose apparent major axis twists. Such structures can be clearly seen in this phase-amplitude representation. All those galaxies for which the 3θ or 4θ terms show significant non-zero amplitudes are plotted in Figure 2.10. The phases are plotted with respect to the major axis position angle. The amplitudes and phases are also tabulated in Table 2.6. The tabulated amplitudes were determined in the same way as the S3, S4 and C3, C4 values in Table 2.5, i.e.; the A(r) data

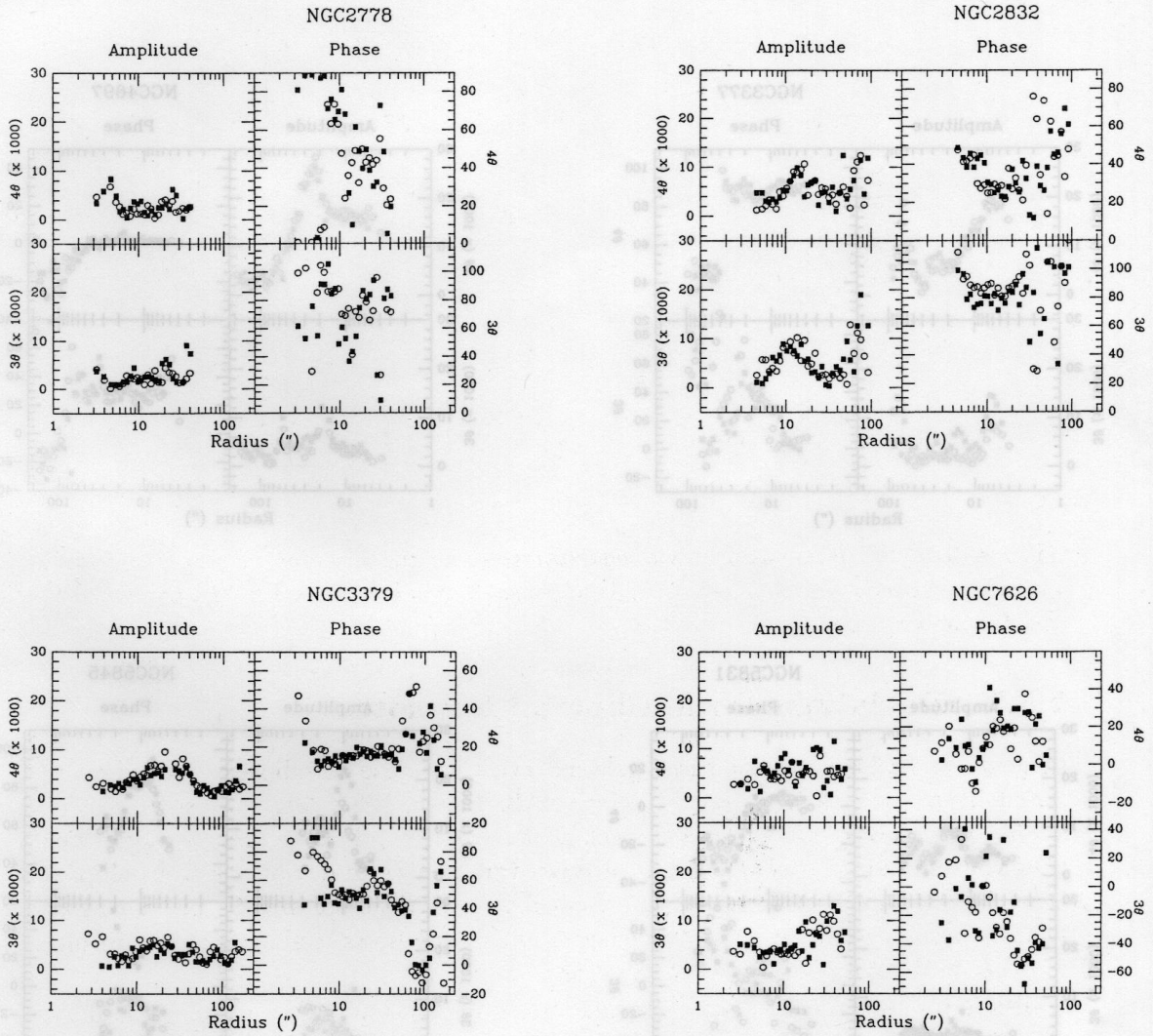

Figure 2.10: *The 3θ and 4θ Fourier terms presented as fractional amplitudes (in units of 0.001) and phases in degrees with respect to the major axis. The results for all galaxies are shown, except for most of the cDs and those few galaxies which do not have any significant non-zero terms. The sample has been subdivided into "box-like" galaxies, "disk-like" galaxies, and the exceptions, as noted in §2.5.3. B data are shown as open circles, while R data are given as filled squares.*

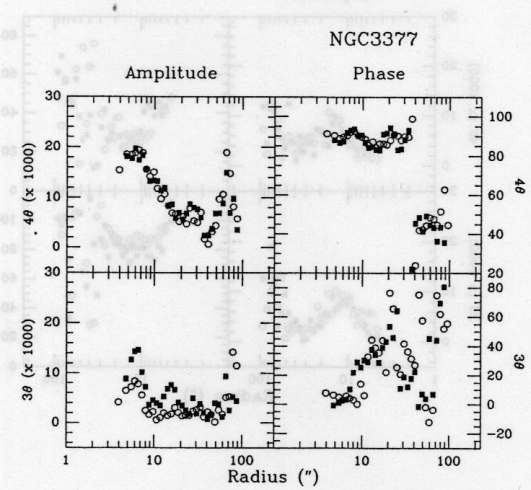
NGC3377
Amplitude
Phase
4θ (x 1000)
3θ (x 1000)
4θ
3θ
Radius (")

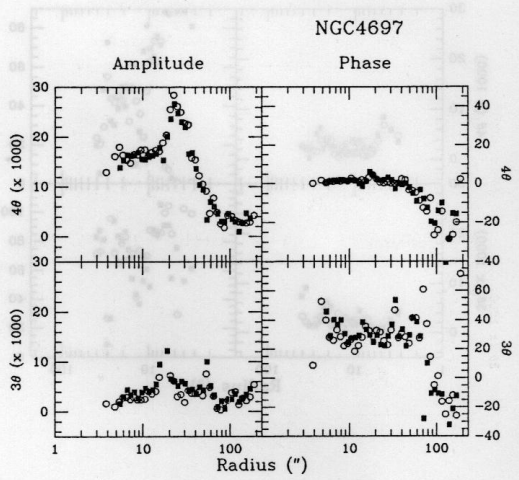
NGC4697
Amplitude
Phase
4θ (x 1000)
3θ (x 1000)
4θ
3θ
Radius (")

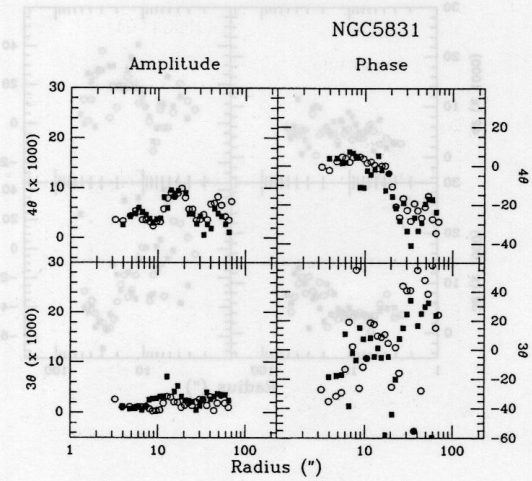
NGC5831
Amplitude
Phase
4θ (x 1000)
3θ (x 1000)
4θ
3θ
Radius (")

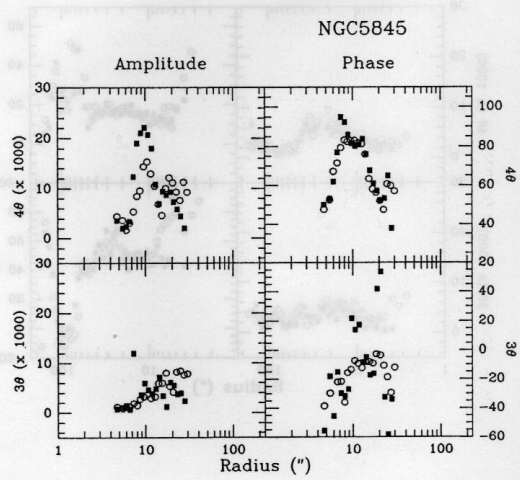
NGC5845
Amplitude
Phase
4θ (x 1000)
3θ (x 1000)
4θ
3θ
Radius (")

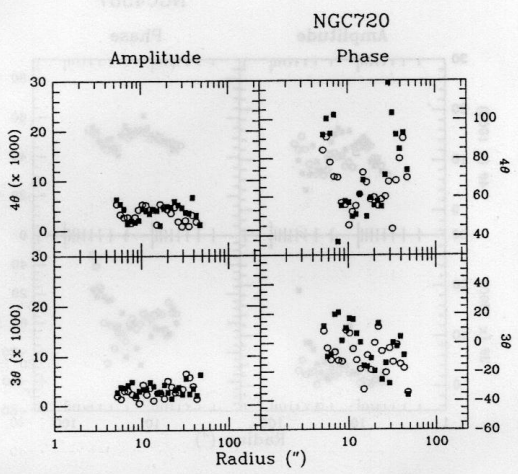
NGC720
Amplitude
Phase
4θ (x 1000)
3θ (x 1000)
4θ
3θ
Radius (")

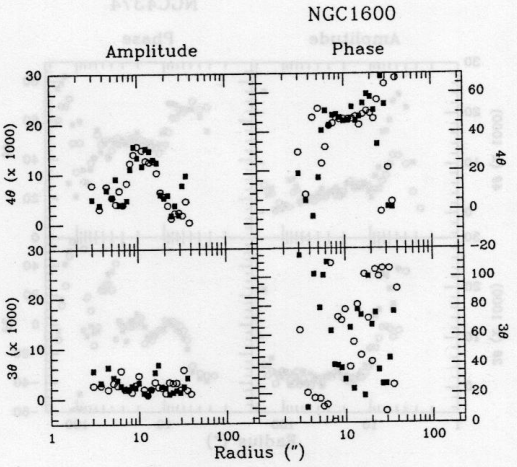
NGC1600
Amplitude
Phase
4θ (x 1000)
3θ (x 1000)
4θ
3θ
Radius (")

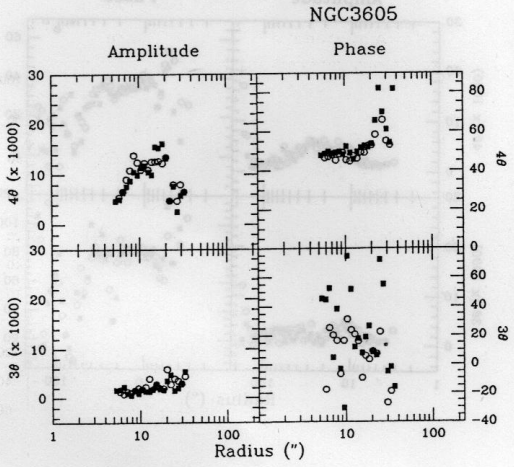
NGC3605
Amplitude
Phase
4θ (x 1000)
3θ (x 1000)
4θ
3θ
Radius (")

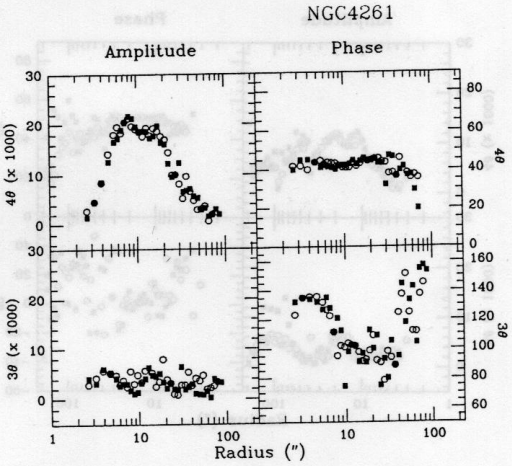
NGC4261
Amplitude
Phase
4θ (x 1000)
3θ (x 1000)
4θ
3θ
Radius (")

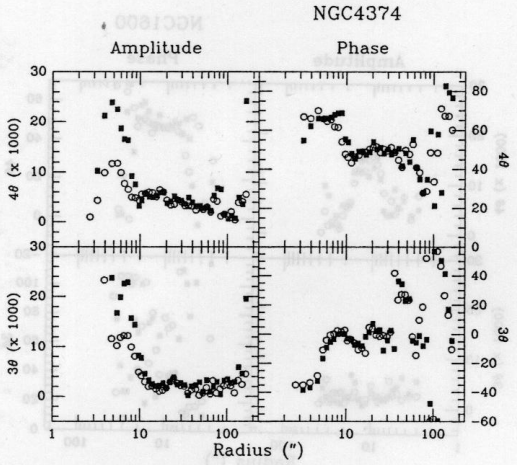
NGC4374
Amplitude
Phase
4θ (x 1000)
3θ (x 1000)
4θ
3θ
Radius (")

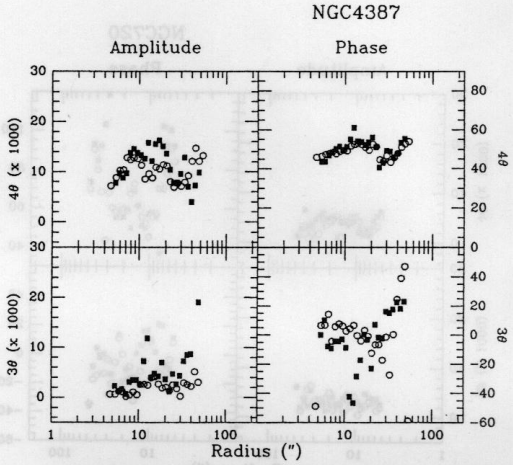
NGC4387
Amplitude
Phase
4θ (x 1000)
3θ (x 1000)
4θ
3θ
Radius (")

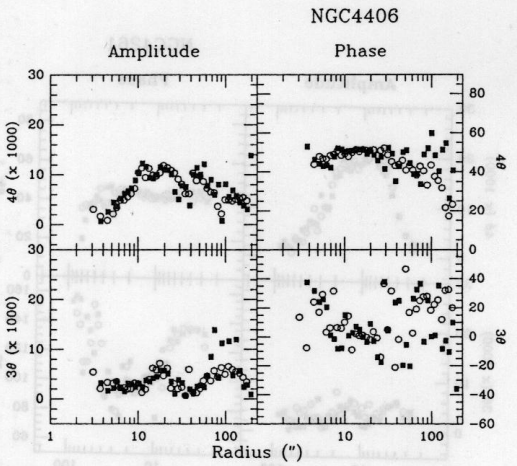
NGC4406
Amplitude
Phase
4θ (x 1000)
3θ (x 1000)
4θ
3θ
Radius (")

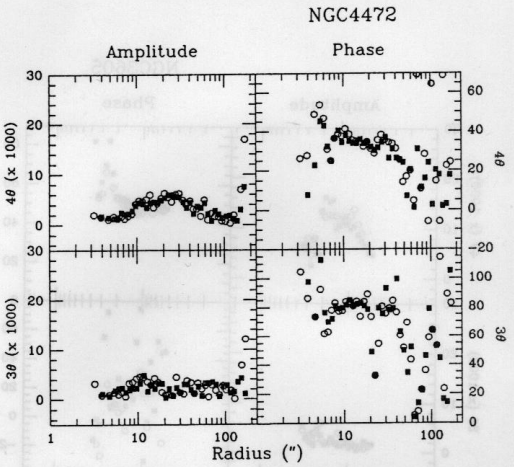
NGC4472
Amplitude
Phase
4θ (x 1000)
3θ (x 1000)
4θ
3θ
Radius (")

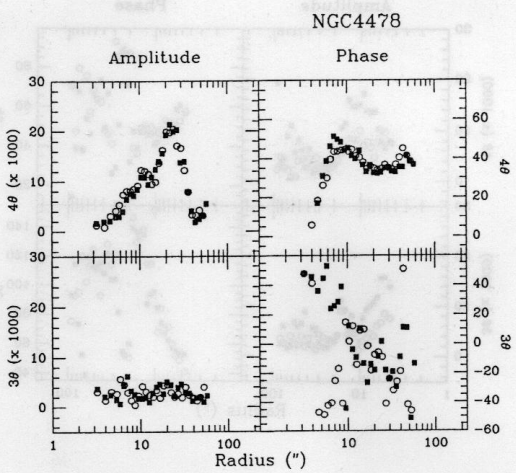
NGC4478
Amplitude
Phase
4θ (x 1000)
3θ (x 1000)
4θ
3θ
Radius (")

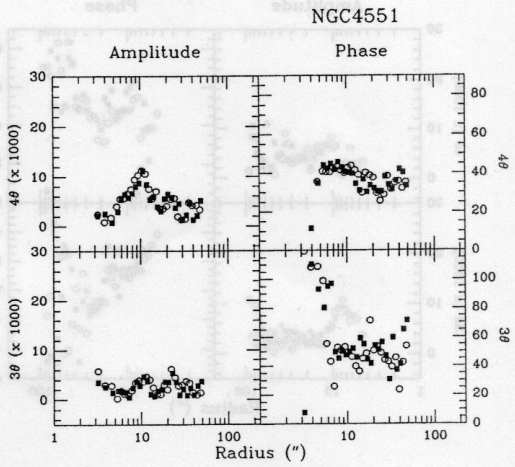
NGC4551
Amplitude
Phase
4θ (x 1000)
3θ (x 1000)
4θ
3θ
Radius (")

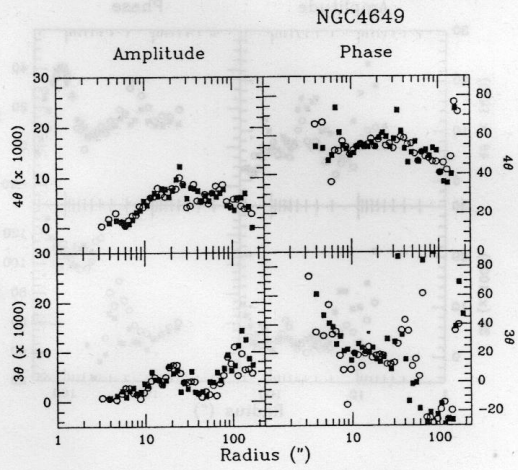
NGC4649
Amplitude
Phase
4θ (x 1000)
3θ (x 1000)
4θ
3θ
Radius (")

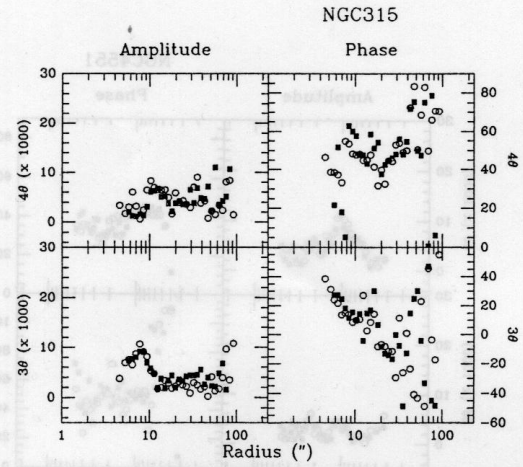
NGC315
Amplitude
Phase
4θ (x 1000)
3θ (x 1000)
4θ
3θ
Radius (")

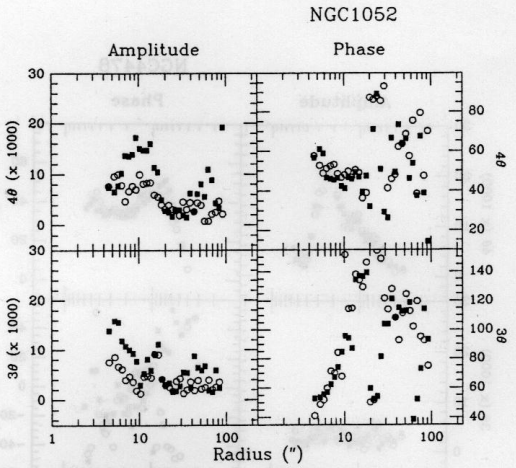
NGC1052
Amplitude
Phase
4θ (x 1000)
3θ (x 1000)
4θ
3θ
Radius (")

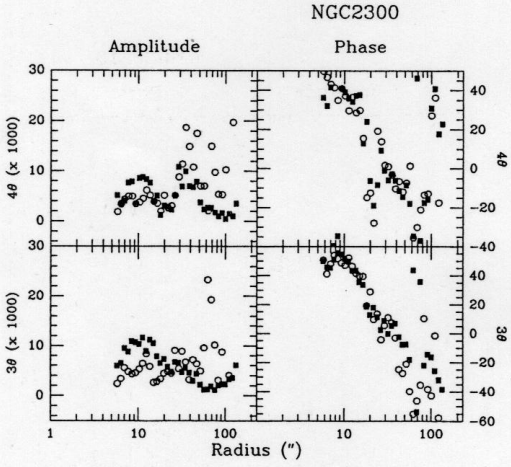
NGC2300
Amplitude
Phase
4θ (x 1000)
3θ (x 1000)
4θ
3θ
Radius (")

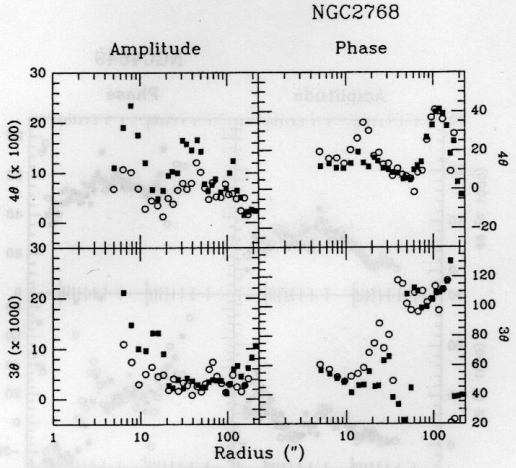
NGC2768
Amplitude
Phase
4θ (x 1000)
3θ (x 1000)
4θ
3θ
Radius (")

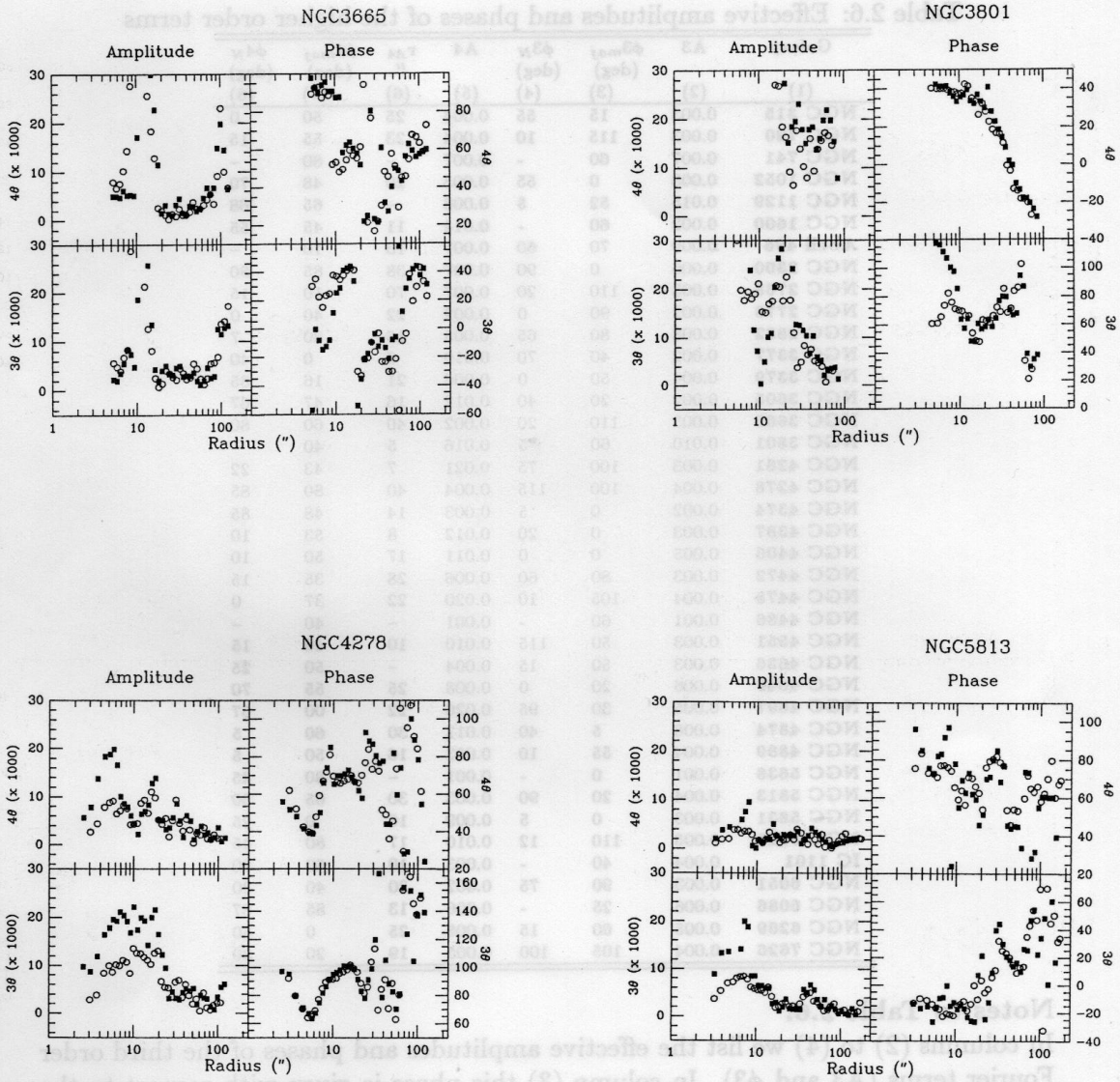
NGC3665
Amplitude
Phase
4θ (x 1000)
3θ (x 1000)
4θ
3θ
Radius (")
NGC3801
Amplitude
Phase
4θ (x 1000)
3θ (x 1000)
4θ
3θ
Radius (")
NGC4278
Amplitude
Phase
4θ (x 1000)
3θ (x 1000)
4θ
3θ
Radius (")
NGC5813
Amplitude
Phase
4θ (x 1000)
3θ (x 1000)
4θ
3θ
Radius (")

were smoothed and the peak amplitude determined. The radius of the 4th-order peak is also given.

Table 2.6: Effective amplitudes and phases of the higher order terms

Galaxy	A3	$\phi 3_{maj}$ (deg)	$\phi 3_N$ (deg)	A4	r_{A4} "	$\phi 4_{maj}$ (deg)	$\phi 4_N$ (deg)
(1)	(2)	(3)	(4)	(5)	(6)	(7)	(8)
NGC 315	0.003	15	55	0.004	25	50	0
NGC 720	0.003	115	10	0.004	23	55	15
NGC 741	0.007	60	-	0.007	–	80	–
NGC 1052	0.003	0	55	0.003	20	48	70
NGC 1129	0.015	52	5	0.008	–	65	68
NGC 1600	0.002	60	-	0.014	11	45	55
Abell 496	0.009	70	60	0.007	13	10	–
NGC 2300	0.006	0	90	0.007	38	85	80
NGC 2768	0.003	110	20	0.007	70	10	15
NGC 2778	0.002	90	0	0.002	22	40	0
NGC 2832	0.008	80	65	0.005	16	30	7
NGC 3377	0.002	40	70	0.019	6	0	40
NGC 3379	0.004	50	0	0.006	21	16	85
NGC 3605	0.002	20	40	0.012	16	47	67
NGC 3665	0.003	110	20	0.002	40	60	80
NGC 3801	0.010	60	5	0.016	5	40	–
NGC 4261	0.003	100	75	0.021	7	43	22
NGC 4278	0.004	100	115	0.004	40	80	85
NGC 4374	0.002	0	5	0.003	14	48	85
NGC 4387	0.003	0	20	0.012	8	53	10
NGC 4406	0.005	0	0	0.011	17	50	10
NGC 4472	0.003	80	60	0.006	28	35	15
NGC 4478	0.004	105	10	0.020	22	37	0
NGC 4486	0.001	60	-	0.001	–	40	–
NGC 4551	0.003	50	115	0.010	10	40	15
NGC 4636	0.003	50	15	0.004	–	50	25
NGC 4649	0.006	20	0	0.008	25	55	70
NGC 4697	0.005	30	95	0.026	22	00	67
NGC 4874	0.008	5	40	0.012	30	60	5
NGC 4889	0.004	55	10	0.003	16	50	5
NGC 5638	0.001	0	-	0.001	–	80	45
NGC 5813	0.004	20	90	0.003	30	65	30
NGC 5831	0.003	0	5	0.009	16	0	25
NGC 5845	0.005	110	12	0.010	17	80	45
IC 1101	0.004	40	-	0.003	10	60	80
NGC 6051	0.003	90	75	0.002	20	40	30
NGC 6086	0.006	25	-	0.006	13	85	87
NGC 6269	0.005	60	15	0.005	25	0	80
NGC 7626	0.004	105	100	0.005	19	20	30

Notes to Table 2.6:
In columns (2) to (4) we list the effective amplitudes and phases of the third order Fourier terms (A3 and $\phi 3$). In column (3) this phase is given with respect to the major axis, and in column (4) with respect to a fixed position angle (i.e., North). Columns (5),(7) and (8) list the same data for the 4th-order terms. We also tabulate (in column (6)) the radius at which A4 reaches its maximum or minimum. The angles in columns (3) and (4) are modulo 120°, while those in columns (7) and (8) are modulo 90°.

Differences in B and R are also a useful diagnostic of the presence of dust. Non-zero 3θ terms are often found at the radius where a galaxy is known to have dust

absorption; for example, in NGC 315 (Butcher *et al.*, 1980, Kormendy and Stauffer, 1987), NGC 1052 (Davies and Illingworth, 1986), NGC 2768 (Strom *et al.*, 1978), NGC 3665 (Kotanyi, 1979), NGC 3801 (Heckman *et al.*, 1983), NGC 4278 (Gunn, 1979), and NGC 4374 (Hansen *et al.*, 1984).

Again, a diagnostic for the presence of dust is that the 3θ and 4θ terms differ in B and R. The integrated colors of these galaxies are no redder than dust free ellipticals so it appears that the amplitude of the 3θ terms and the differences seen between B and R are much more sensitive indicators of the presence of small quantities of dust than integrated colors. Therefore, many of the other galaxies with significant non-zero 3θ terms and differences in the 3θ and 4θ terms may also be dusty. A way of confirming this could be through color maps (see e.g., the maps of NGC 1052 in Davies and Illingworth, 1986). Possible candidates for dust from our sample that have either significant 3θ terms or notable differences in the amplitudes in B and R would be NGC 2300, NGC 2832, NGC 3377, and NGC 5813.

For the remaining galaxies the non-zero 3rd and 4th order terms presumably represent non-elliptical distortions in the stellar densities. Even for those with modest amounts of dust, some of the structure may well be intrinsic to the stellar component. One other class of galaxies needs to be distinguished in the discussion that follows. These are the large, often cD galaxies, Abell 496, IC 1101, NGC 741, NGC 1129, NGC 4874, NGC 4889, NGC 6051, NGC 6086 and NGC 6269, which are strongly contaminated by close companion galaxies, and are often of low surface brightness. For these galaxies the data are noisy and have had the many companions removed, rendering the data generally unsuitable for deriving deviations from ellipses.

There are only three galaxies in our sample which are consistent with having truly elliptical isophotes. They are NGC 4486, NGC 4636 and NGC 5638. Omitting the regions with dust it might be possible to add NGC 5813 and NGC 3665 to this group. For the remaining galaxies, with the exception of the large (cD?) galaxies noted above, we have plotted 3rd and 4th-order amplitudes and phases in Fig. 2.10. They can be usefully "classified" into three groups as follows:

1. **"Box-shaped" galaxies.** These galaxies show a significant negative cos 4θ term, and usually a small sin 4θ term. Equivalently, they show significant 4th-order amplitude with a phase of 45° (modulo 90°), and have a boxy appearance. They occur frequently (cf., Bender *et al.*, 1988). This group contains NGC 720, 1600, 3605, 4261, 4374, 4387, 4406, 4472, 4478, 4551 and NGC 4649. Its members have small 3rd-order amplitudes, except for NGC 4374 which contains dust and the outer parts of NGC 4649, where the influence of its companion, NGC 4647, is noticed. The degree of "boxyness" usually varies with radius. It is interesting to note that nearly half of these galaxies are low-luminosity elliptical companions (NGC 3605, 4387, 4478 and 4551) to giant ellipticals – out of a sample that is strongly biased towards luminous objects.

2. **"Disk-like" galaxies.** The galaxies in this group have positive cos 4θ terms, that have been interpreted as being due to an embedded faint disk component. This disk is not comparable with those seen in S0 galaxies, since the

contribution of this disk anywhere to the surface brightness never amounts to more than a few percent. The 4th-order amplitudes are large, with phases of 0° (modulo 90°). Members of this group are NGC 2768, 3377, 4697, 5831 and NGC 5845. NGC 3377 and NGC 4697 are excellent examples of ellipticals with weak disks, whose presence is very apparent in the amplitude-phase data shown in Figure 2.10. See also the comments on NGC 4697 and Figure 2.16 in Appendix B. There is overlap with the dusty group, since NGC 2768 and NGC 5845 contain dust on their major axis, while NGC 3377 has some in its inner areas, but not on its major axis. *It is noteworthy that in the outer regions of all five galaxies, where the relative contribution of the disk has decreased considerably, the appearance of the isophotes changes*: NGC 3377 and NGC 2768 become boxy, while the *phase* of the other three changes to ≈65°, intermediate between "box-like" and "disk-like".

3. **Exceptions.** Along with the dusty galaxies, this group consists of NGC 2778, 2832, 3379 and 7626. The amplitudes in this group are small, but still significantly non-zero. The structures are complex and not as easily interpreted as the two "classes" above. The 3rd and 4th-order deviations in NGC 2832 are probably caused by its close companion, NGC 2831. NGC 3379 is noteworthy. The 3rd and 4th-order amplitudes at 50° and 15°, respectively, indicate a complex shape, with a "diamond-like" character.

While generally small, there are good indications that these terms do convey useful information about the dynamical properties and dynamical history of ellipticals (e.g., Bender *et al.*, 1989). This is discussed further in §2.6.

For those galaxies where the high-order deviations could be determined to large radii (i.e., excluding those galaxies whose outer parts were contaminated by companions/superpositions typical of the large galaxies in clusters), it is striking to note that most of the amplitudes in 3θ and 4θ peak at radii comparable to r_e or smaller.

Franx, Illingworth and Heckman (1989b) also noted that plotting the phases against a fixed position angle (PA), as opposed to the major axis position angle enabled one to readily identify features that do not follow the major axis, i.e., they do not twist. They show a striking example of a skew "disk-like" structure in NGC 1700. We have plotted the phases against North for our galaxies. Comparing the constant-PA phases with the phases plotted against the major axis position angle, structures can occasionally be seen which do not follow the major axis. In our sample we have found two examples of this. They are NGC 1129 and NGC 5831. The amplitudes of the 3rd and 4th-order terms and their phases with a fixed zero-point are plotted in Figure 2.11 (compare to the same galaxies in Figure 2.10). Both galaxies have a large position angle twist; NGC 1129 by 90°! NGC 1129 is a large elliptical in a small cluster. Such galaxies have probably grown by digesting their neighbors – the structure in NGC 1129 could have resulted from a recent such acquisition. The position angle twist in NGC 1129 is so dramatic that we could even be seeing the result of a merger of two comparable ellipticals. On the other hand, if the galaxy is triaxial with different axial ratios, this twist might be intrinsic, and

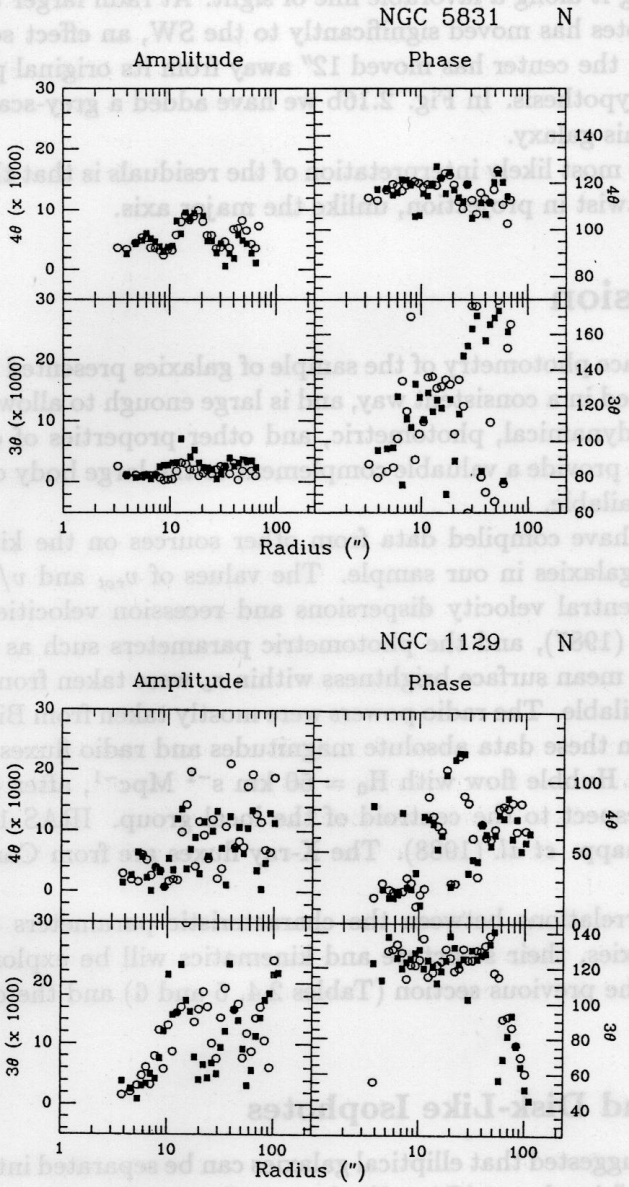

Figure 2.11: *As for Figure 2.10, but with respect to North for NGC 1129 and NGC 5831. In the former the position angle of the 3θ structure remains constant, while in the latter it is the 4θ structure that remains at constant position angle while the major axis twists.*

the result of viewing it along a favorable line of sight. At radii larger than 30″ , the center of the isophotes has moved significantly to the SW, an effect seen in both B and R. By r=100″ , the center has moved 12″ away from its original position. This favors the merger hypothesis. In Fig. 2.16b we have added a grey-scale map of the central regions of this galaxy.

In NGC 5831 the most likely interpretation of the residuals is that there is a weak disk that does not twist in projection, unlike the major axis.

2.6 Discussion

The multicolor surface photometry of the sample of galaxies presented here has been acquired and analysed in a consistent way, and is large enough to allow us to explore the correlations of dynamical, photometric, and other properties of ellipticals. In addition, these data provide a valuable complement to the large body of kinematical data that is now available.

In Table 2.7 we have compiled data from other sources on the kinematics and photometry of the galaxies in our sample. The values of v_{rot} and $v/\bar{\sigma}$ were taken from DEFIS, the central velocity dispersions and recession velocities were taken from Davies *et al.* (1987), and the photometric parameters such as the apparent magnitude, and the mean surface brightness within r_e were taken from Burstein *et al.* (1987), when available. The radio powers were mostly taken from Birkinshaw and Davies (1985). From these data absolute magnitudes and radio fluxes were derived assuming a uniform Hubble flow with $H_0 = 50$ km s^{-1} Mpc^{-1}, after correcting for the velocity with respect to the centroid of the local group. IRAS 100 μm fluxes were taken from Knapp *et al.* (1988). The X-ray fluxes are from Canizares *et al.* (1987).

A number of correlations between the characteristic parameters of the stellar populations of galaxies, their structure and kinematics will be explored using the data assembled in the previous section (Tables 2.4, 5 and 6) and the collected data of Table 2.7.

2.6.1 Box- and Disk-Like Isophotes

Bender (1988) has suggested that elliptical galaxies can be separated into two classes: those with "box-like" isophotes (C4 < 0), that are flattened by anisotropic velocity dispersions, and those with "disk-like" isophotes (C4 > 0) that are flattened by rotation. In Figure 2.12a we plot $(v/\sigma)^*$ vs. C4 for our sample, after removing the ellipticals with dust and the brightest cluster galaxies (including cD's) (see §2.5). Our data show a similar distribution to that shown by Bender, with some detailed differences. It appears that for galaxies that are within a factor of two of being rotationally-flattened (for which $(v/\sigma)^* \approx 1$), $(v/\sigma)^*$ is independent of C4. That is, for rotationally-flattened ellipticals, there are roughly comparable numbers of elliptical galaxies with boxy as with disk-like isophotes. Bender's sample lacked the galaxies with boxy isophotes and $(v/\sigma)^* > 0.5$, such as NGC 2778, 3605, 4261, 4387,

Table 2.7: Global parameters from the literature

Galaxy	r_e	$(\sigma)_m$	$\left(\frac{v}{\sigma}\right)^*$	B_T	M_{B_T}	SB_e	F_{100}	log P_{5GHz}	log ΔL_X
	kpc	km s^{-1}		mag	mag	mag arcsec^{-2}	mJy	W Hz^{-1}	erg s^{-1}
(1)	(2)	(3)	(4)	(5)	(6)	(7)	(8)	(9)	(10)
NGC 315	35	352	0.17	12.50	-23.59	22.36	360± 90	23.09	41.91
NGC 720	8.7	247	0.47	11.15	-21.53	21.14	<56	<19.02	41.06
NGC 741	30	280	0.75	12.05	-23.10	21.64	1000± 96	22.39	--
NGC 1052	5.0	206	0.70	11.53	-20.94	21.11	1400± 60	21.96	--
NGC 1129	>26	335	--	11.25	-23.68	--	--	--	--
NGC 1600	26	321	0.13	12.01	-23.14	22.17	170± 65	21.24	41.81
Abell 496	>47	354	0.11	13.42	-23.16	--	--	--	--
NGC 2300	12	260	--	11.99	-21.54	21.51	<81	--	41.10
NGC 2768	10.1	198	0.48	10.92	-21.16	21.56	1220± 56	19.93	--
NGC 2778	3.4	166	1.11	12.50	-19.51	21.38	450± 85	<19.21	--
NGC 2832	31	354	0.21	12.39	-22.86	--	1330± 137	--	--
NGC 3377	3.0	131	0.80	11.10	-19.50	20.76	310± 57	<17.90	<39.60
NGC 3379	2.5	201	0.63	10.33	-20.20	20.16	<96	18.31	<39.80
NGC 3605	2.3	120	0.70	13.06	-18.34	21.42	--	<18.18	--
NGC 3665	13.4	205	1.20	11.75	-21.36	--	6690± 163	20.96	--
NGC 3801	13.8	168	0.85	13.00	-21.33	--	2490± 78	--	--
NGC 4261	8.7	294	0.78	11.38	-21.78	21.25	130± 43	22.69	--
NGC 4278	2.6	266	0.78	11.13	-19.87	20.60	1650± 53	21.18	--
NGC 4374	5.9	287	0.23	10.23	-21.53	20.81	1030± 109	22.02	40.79
NGC 4387	2.1	84	0.72	12.95	-18.79	20.80	<158	<18.38	--
NGC 4406	10.9	250	0.22	10.02	-21.79	21.65	290± 59	<18.39	41.58
NGC 4472	11.9	287	0.37	9.32	-22.34	21.40	<94	20.46	41.71
NGC 4478	1.7	149	1.05	12.15	-19.52	19.87	<66	<18.83	--
NGC 4486	11.5	361	0.18	9.62	-22.14	21.60	360± 91	23.49	--
NGC 4551	2.2	100	0.69	12.85	-18.94	20.95	<137	<18.36	--
NGC 4636	12.2	191	0.32	10.50	-21.46	22.23	<152	20.06	41.64
NGC 4649	8.5	341	0.41	9.83	-21.89	21.10	970± 57	19.89	41.40
NGC 4697	9.9	165	0.82	10.11	-21.63	21.41	1100± 67	<18.40	40.27
NGC 4874	45	245	--	12.90	-23.40	23.24	<95	--	--
NGC 4889	26	381	0.11	12.57	-23.23	21.96	<61	20.23	--
NGC 5638	4.6	159	1.31	12.20	-20.47	21.28	400± 106	<18.74	--
NGC 5813	9.1	238	0.07	11.57	-21.23	21.82	<88	19.35	--
NGC 5831	4.5	166	0.58	12.46	-20.33	21.42	--	<18.83	--
NGC 5845	0.7	251	1.20	13.10	-19.27	18.38	200± 87	<18.83	--
IC 1101	>110	375	0.08	13.93	-24.40	--	--	--	--
NGC 6051	25	243	--	13.49	-22.95	--	490± 296	--	--
NGC 6086	24	304	--	13.50	-22.95	--	<172	--	--
NGC 6269	50	228	--	13.02	-23.63	--	--	--	--
NGC 7626	15	234	0.21	12.17	-22.35	21.87	<113	21.79	41.30

Notes to Table 2.7: In column (2) we present the major axis effective radii in kpc, using effective radii from Table 2.3 and group velocities from Davies *et al.* (1987), corrected for the motion with respect for the centroid of the local group. The mean velocity dispersion in column (3) in km s^{-1} and the $(v/\sigma)^*$ in column (4) are taken primarily from DEFIS and Malumuth and Kirshner (1985). The total blue luminosity in column (6) (in mag) is derived from the apparent blue luminosities given by Burstein *et al.* (1987) (in column 5), using $H_0 = 50$km s^{-1} Mpc^{-1}. The mean blue surface brightness inside an effective radius was derived using the luminosities and effective radii here, and tabulated in column (7) in mag arcsec^{-2}. The IRAS 100 μm fluxes in column (8) were taken from Knapp *et al.* (1988) and are given in mJy. The radio powers (in W/Hz) were mostly taken from Birkinshaw and Davies (1985). The X-ray fluxes in erg/s are from Canizares *et al.* (1987).

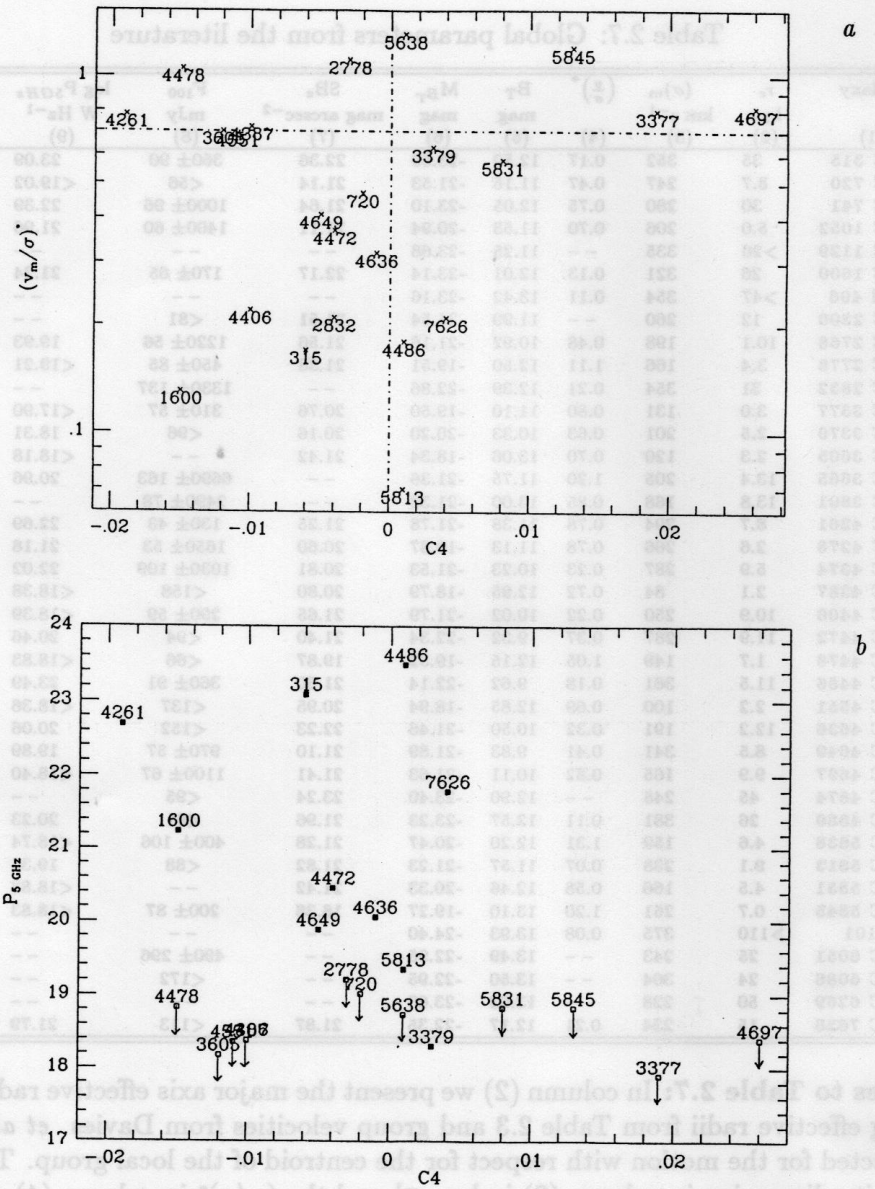

Figure 2.12: *Global parameters against C4 and A4. The data plotted against C4 ranges from $(v/\sigma)^*$, a measure of the amount of rotational support, in 2.12a, to the radio continuum power at 5 GHz in 2.12b, the total blue luminosity in magnitudes in 2.12c, the logarithmic color gradient in $B-R$ in 2.12d, and finally to the logarithmic color gradient in $U-R$ in 2.12e. The 4th-order Fourier amplitude A4 is plotted against ellipticity at 10″ in 2.12f.*

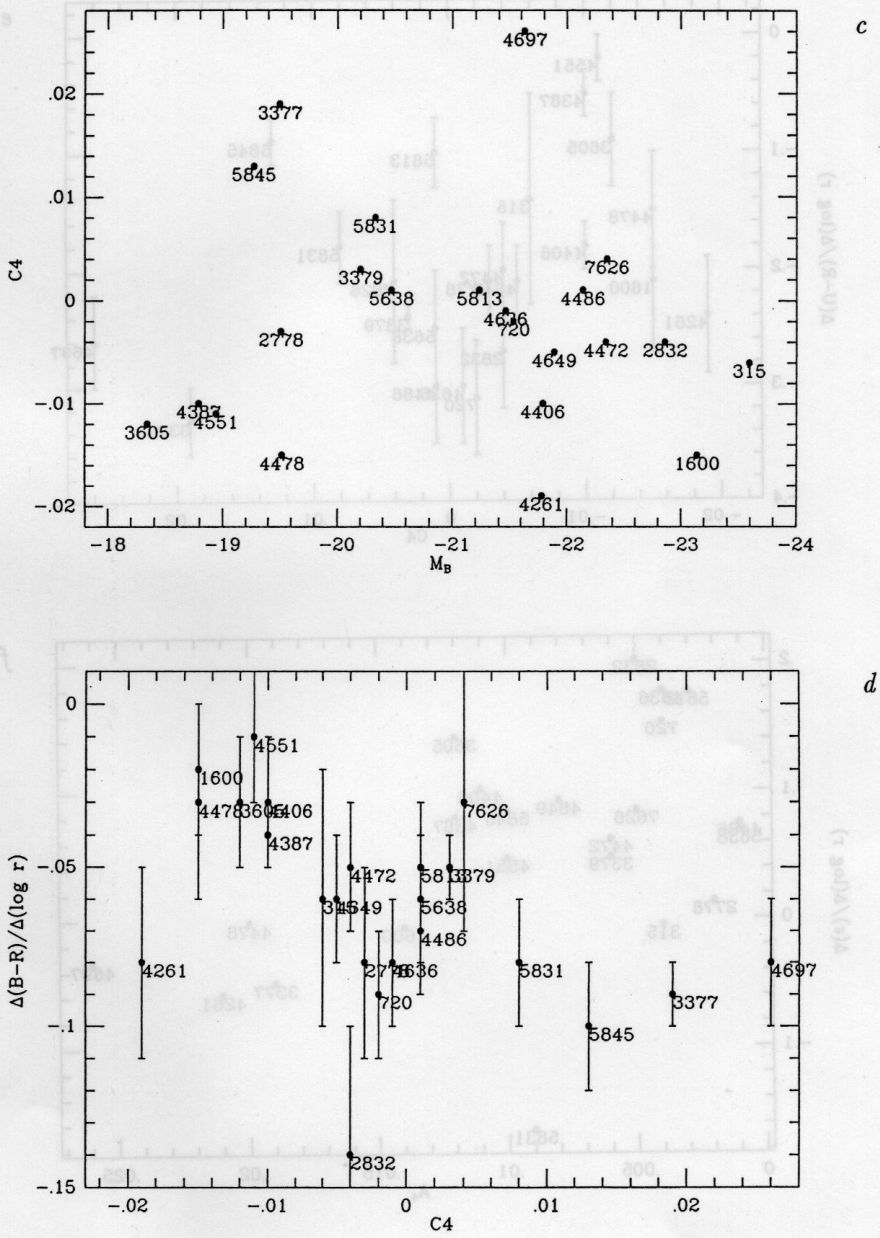

Figure 2.12: *Continued*

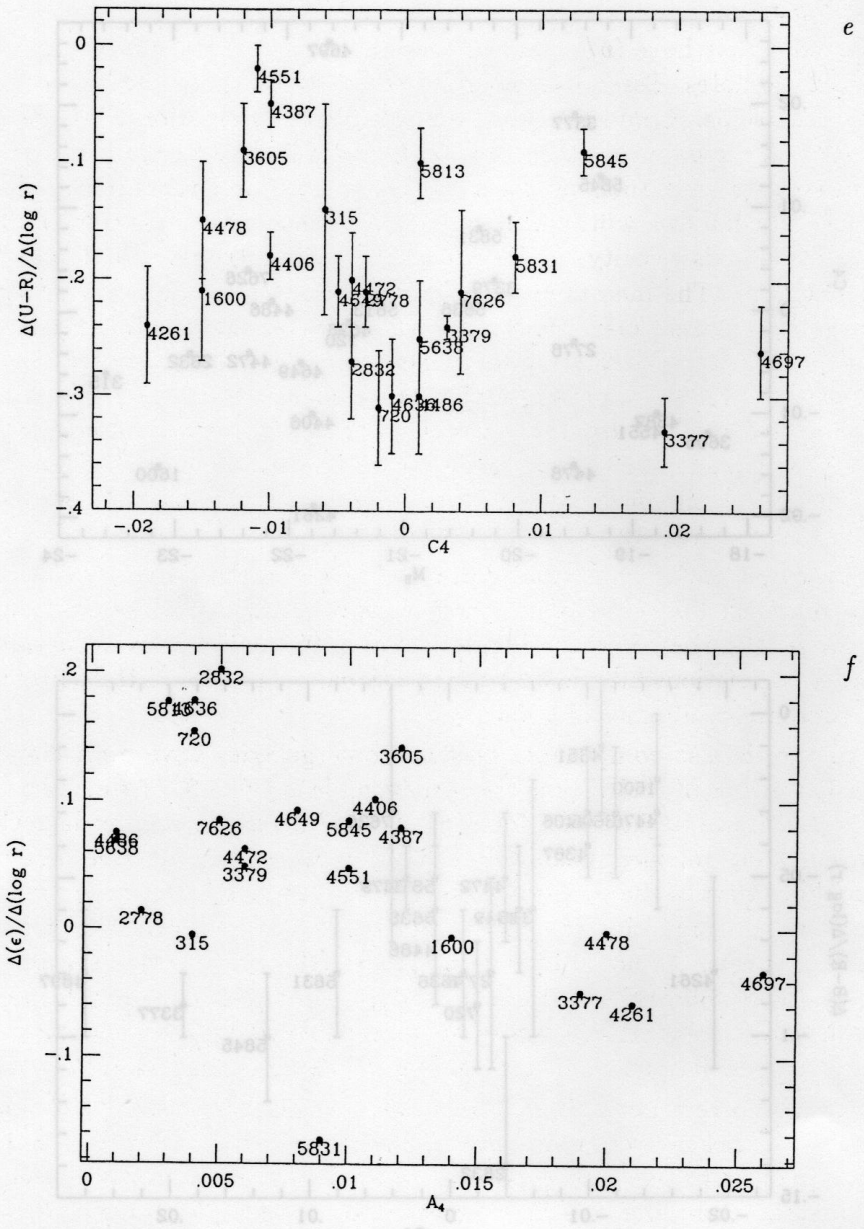

Figure 2.12: *Continued*

4478 and 4551. It is interesting to note that 4 of these : NGC 3605, 4387, 4478 and 4551 are low-luminosity companions to luminous ellipticals, and that NGC 2778 has a close companion.

For galaxies that have $(v/\sigma)^* < 0.5$ there appears to be a strong preference for box-shaped isophotes. Essentially no galaxies are found that have low rotation and disk-like distortions. Could this be the result of an observational selection effect? As Bender and others have noted, the existence of isophote residuals from ellipses that have positive amplitude for the cos 4θ term, C4, is indicative of the presence of a weak disk. Such a disk will typically be rotating much faster than the body of the elliptical. Major axis velocity profiles will then have contributions from both the disk and the elliptical. The measurement of velocities in multicomponent systems with Fourier or CCF (Cross-Correlation) is known to be biased towards the narrow-lined, and thus the more rapidly-rotating component (see, e.g., Whitmore, 1980, and Franx and Illingworth, 1988). Thus the major-axis velocity in such a composite system would be biased towards higher values, leading to an overestimate of $(v/\sigma)^*$ (cf. Figure 2.3 of Bender (1988) and Figure 2.12a). An example of an elliptical where the velocity drops significantly away from the major axis is NGC 4697 (Binney, Davies and Illingworth, 1989).

This may be a factor in the distribution of values in the C4 vs $(v/\sigma)^*$ plane, but does not diminish the remarkable correlations of C4 with radio power and X-ray luminosity seen in these data by Bender *et al.* (1989). The relevant parameter for these other correlations may not be the rotational properties of the elliptical body, but the presence or absence of a disk.

The picture is also complicated because some galaxies have both disk-like and box-like distortions of their isophotes. An example is NGC 3377 which has positive C4 for $r < 40''$ and negative C4 for $r > 40''$. What is the appropriate C4 to use in Figure 2.12a in galaxies such as NGC 3377? We used the inner value, but this is rather ad hoc. Part of the problem here is using C4 alone to describe the 4th-order residuals, and thus ignoring the sin 4θ component – or, alternatively, ignoring the phase of the effects. As noted by Franx, Illingworth and Heckman (1989b), certain structures do not follow the major axis, and so use of the phase-amplitude form for the 3 and 4θ terms may subsequently prove to be more useful in understanding the source of these deviations from ellipses. We will explore this in a future paper.

We have also investigated other correlations. We find no correlation in this sample of elliptical galaxies between ellipticity and C4; there are as many flattened galaxies in our sample with box-shaped isophotes as with disk-like perturbations. Our sample is too small to show the V-shaped distribution noted by Bender *et al.* (1989). Initial inspection of Fig. 2.12b indicates no correlation between C4 and luminosity, although there is a deficit of luminous galaxies with disk-like isophotes. However, if one excludes the galaxies that are close companions of giant ellipticals, the trend for luminous galaxies to be boxy, and for less luminous ones to be disk-like becomes clearer. Since the companion galaxies have other distinct properties, namely minimal or zero color gradients and appear to be rotationally-flattened, they may well form a physically separate group of objects.

We also show the correlation with radio power in Figure 2.12c, as did Bender *et al.* (1987), and Bender *et al.* (1989). The lack of powerful radio galaxies amongst those with positive C4 is striking. Within the subset of galaxies with negative C4, there is no relation at all with $(v/\sigma)^*$, with radio flux or with luminosity (see Figure 2.12a, 2.12b, and 2.12c).

Other correlations have been made. There is a slight tendency for galaxies with larger negative C4 to have smaller color gradients, both in $B-R$ and in $U-R$ (Figures 2.12d and 2.12e). This effect disappears when one removes the low-luminosity companions to bright ellipticals. If boxy isophotes arise from mergers or accretion events, as has been suggested by Binney and Petrou (1985), one might expect boxy galaxies to show smaller gradients. However, it would be unexpected if the lowest luminosity galaxies were the ones that most strongly showed the effects of merging or accretion.

One correlation which did arise was between the logarithmic gradient of the ellipticity and the 4th-order amplitude (from Figure 2.10 and Table 2.6 in §2.5). Ellipticals with large 4th-order amplitudes, with the exception of NGC 5831 appear to have small ellipticity gradients (Figure 2.12f). The implications of this correlation are not clear.

2.6.2 Color Gradients

The colors of the galaxies in this sample become bluer with radius in both $U-R$ and $B-R$, with an occasional profile remaining constant in color. The color gradients do not depend upon ellipticity, IRAS $100\mu m$ flux (after removing the dusty ellipticals), or the twist in position angle. After removing NGC 3801, a particularly dusty galaxy, we find that the logarithmic gradient in $U-R$, i.e., $\Delta(U-R)/\Delta(\log\ r)$ is -0.20 ± 0.02 mag per dex in radius, and is -0.09 ± 0.02 mag per dex in radius in $B-R$. The $B-R$ and $U-R$ gradients correlate with each other (Figure 2.13), but with some scatter. While recent star formation and/or age differences could be responsible for some of the scatter, it is most likely that the scatter arises from observational errors introduced by the uncertainty in the sky levels. We have made an attempt to determine this error. Since the sky uncertainties affect the outermost points, in a non-linear way, the error in the gradient is dependent on the outer cutoff radius. However, since the colour profiles are usually linear, when plotted against the logarithm of radius, the gradient can be determined in a region where the sky errors are less important. We have estimated our errors in the gradients in the following way: we made three colour profiles, namely the original, and two in which the color in the outermost point was 0.1 mag bluer and redder, as a result of the expected uncertainty in the sky (10%). From these profiles we used all data points up to $0.5r_e$, and determined the gradients using a least squares method. The final error was a combination of the differences between these gradients with respect to each other and with respect to the original gradient, calculated using all the points. Typically, they are $\approx$0.03 mag in $B-R$ and 0.05 mag in U-R. Most of the scatter

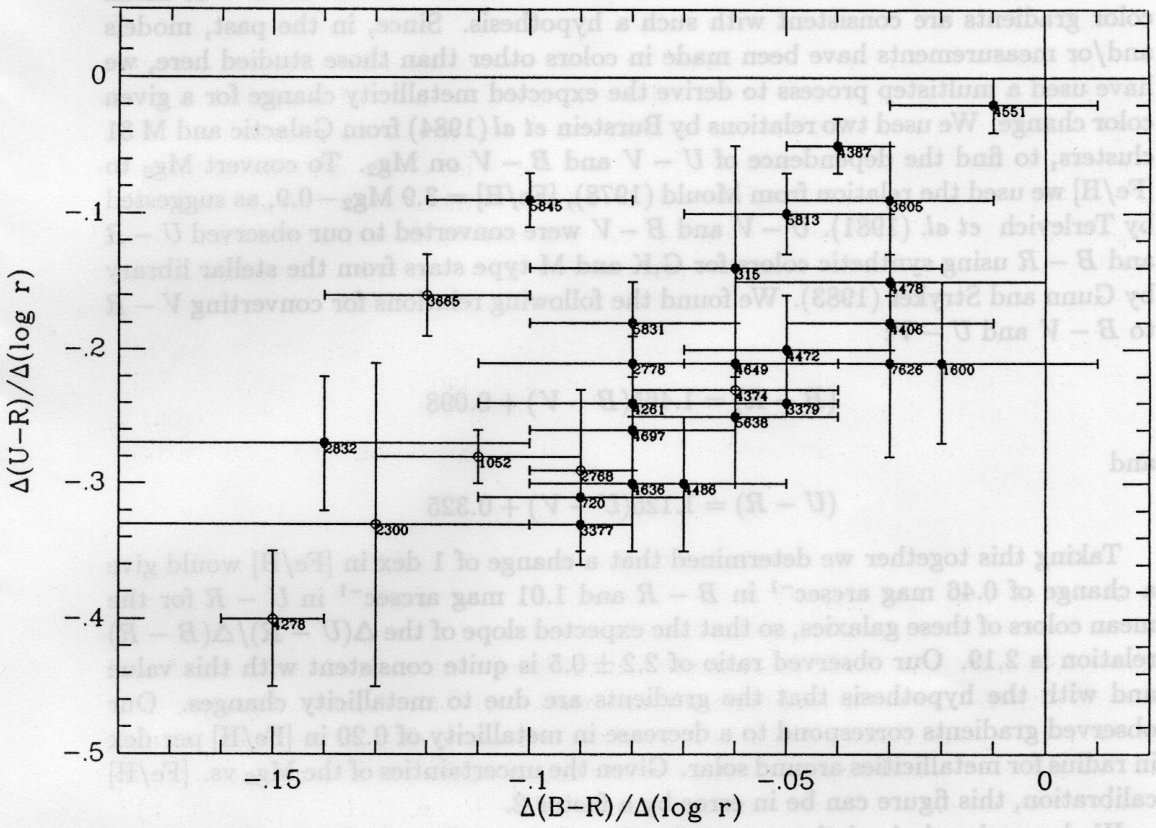

Figure 2.13: *Logarithmic color gradients in $U - R$ in mag dex^{-1} against color gradients in $B - R$. There is a correlation, but it is weaker than might be expected. This is mainly due to the large scatter in the $B - R$ gradient from observational uncertainty.*

in Figure 2.13 could be caused by these uncertainties, but for a few galaxies, like NGC 5845 and NGC 3665, other factors appear to be playing a role.

Assuming that the color gradients are due to metallicity changes (decreasing metallicity), it is of interest to see if the ratio of the $U-R$ to the $B-R$ mean color gradients are consistent with such a hypothesis. Since, in the past, models and/or measurements have been made in colors other than those studied here, we have used a multistep process to derive the expected metallicity change for a given color change. We used two relations by Burstein *et al* (1984) from Galactic and M 31 clusters, to find the dependence of $U-V$ and $B-V$ on Mg_2. To convert Mg_2 to [Fe/H] we used the relation from Mould (1978), [Fe/H] = 3.9 $Mg_2 - 0.9$, as suggested by Terlevich *et al.* (1981). $U-V$ and $B-V$ were converted to our observed $U-R$ and $B-R$ using synthetic colors for G,K and M-type stars from the stellar library by Gunn and Stryker (1983). We found the following relations for converting $V-R$ to $B-V$ and $U-V$:

$$(B-R) = 1.465(B-V) + 0.098$$

and

$$(U-R) = 1.125(U-V) + 0.325$$

Taking this together we determined that a change of 1 dex in [Fe/H] would give a change of 0.46 mag arcsec^{-1} in $B-R$ and 1.01 mag arcsec^{-1} in $U-R$ for the mean colors of these galaxies, so that the expected slope of the $\Delta(U-R)/\Delta(B-R)$ relation is 2.19. Our observed ratio of 2.2 ± 0.5 is quite consistent with this value and with the hypothesis that the gradients are due to metallicity changes. Our observed gradients correspond to a decrease in metallicity of 0.20 in [Fe/H] per dex in radius for metallicities around solar. Given the uncertainties of the Mg_2 vs. [Fe/H] calibration, this figure can be in error by a factor 2.

We have also derived the expected value of the $\Delta(U-R)/\Delta(B-R)$ ratio by using the artificial colors from Peletier *et al.* (1989). They calculated integrated colors for composite stellar systems using the Yale (Green *et al.*, 1987) isochrones. For systems without a blue horizontal branch contribution, their values for $\Delta(U-R)/\Delta(B-R)$ are given in Table 2.8.

These values while lower than what we derive, are certainly within the uncertainty of our mean ratio of 2.2 ± 0.5. Increasing the horizontal branch contribution in the outer parts results in larger numbers, as would be expected, and would give ratios closer to the observed value. Together these two approaches suggest that the observed ratios are consistent with the assumption that the color gradients are caused by a change in metallicity.

One should not infer too much from this conclusion, however, since the observational errors are large. The results from different authors are not as consistent as one would like. The differences are often comparable to the gradients, particularly in $B-R$. While difficult to measure, U band data are very valuable since the gradients seen in $U-R$ are large enough that observational uncertainties do not dominate as they can in $B-V$ and $B-R$. We believe that the reality of color gradients is not

Table 2.8: Gradient ratios

age	range in Z	$\frac{\nabla(U-R)}{\nabla(B-R)}$
(1)	(2)	(3)
20 Gyr	0.04 – 0.01	1.79
	0.01 – 0.001	1.73
16 Gyr	0.04 – 0.01	1.71
	0.01 – 0.001	1.64

Notes to Table 2.8: In column (3) we list the expected gradient ratio between $U - R$ and $B - R$ for integrated stellar populations for two different ages and two different metallicities (from Peletier *et al.*, 1989).

now in question, and that the most likely explanation for them is a decrease in the metal abundance with radius. However, the detailed form of this variation is still rather poorly determined.

Vigroux *et al.* (1988) and Vader *et al.* (1988) have measured $B - R$ color gradients for 36 early-type galaxies. For their luminous galaxies, with measured kinematics, they found that galaxies with large $(v/\sigma)^*$, i.e., rotationally-supported galaxies (see, e.g. DEFIS), have large color gradients. In the mean, as noted in §2.5, their gradients agree with ours. In Figure 2.14a and b we plot our $B - R$ and $U - R$ gradients against $(v/\sigma)^*$ for our whole sample, with the exception of the largest galaxies (typically cD's and first-ranked cluster members). The correlation noted by Vader *et al.* does not appear with this sample. There is a hint in Figure 2.14 that those with larger $B - R$ gradients may be more rotationally-supported, but the opposite might be suggested by the $U - R$ data; neither "trend" is at all significant.

Color gradients (and absolute colors) can provide invaluable constraints on the formation processes for ellipticals. They have particular utility for what they can tell us about the role of gaseous interactions and star formation. The luminosity dependence of color gradients is a good discriminant amongst various models of galaxy formation. If galaxies were formed purely by dissipation, the most massive galaxies would have the largest color gradients (Carlberg, 1984). Mergers on the other hand cause initial color gradients to decrease (e.g., White, 1980). Thus, the luminosity dependence may provide clues as to the importance and frequency of mergers and/or accretions. The number of mergers which a galaxy has undergone would be expected to increase with luminosity, leading one to expect color gradients to diminish with increasing luminosity.

There is also no indication that galaxies change shape with photometric passband. There are no consistent, large scale differences in the ellipticity profiles. The ellipticity profiles overlap in the different colors, except in the cases where dust is present. In such cases the dust usually manifests itself as rather irregular differences in the color ellipticity profiles, and in the 3θ and 4θ terms. This is also true of the

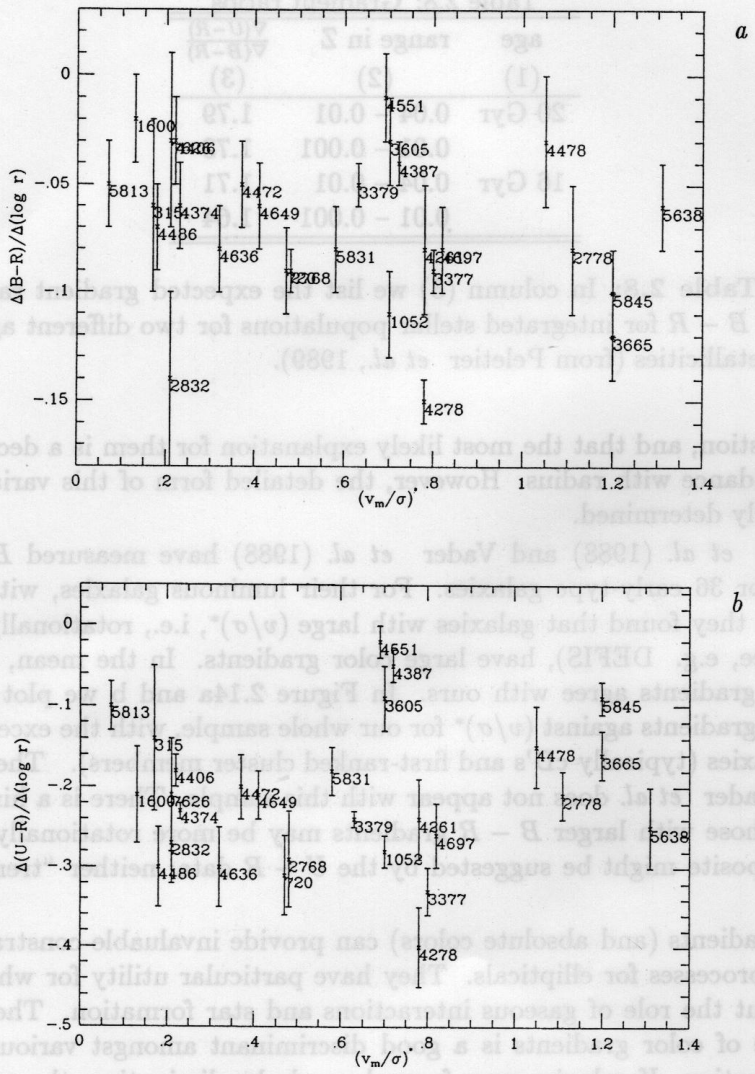

Figure 2.14: *Global parameters against color gradients. $(v/\sigma)^*$ is plotted against the color gradients in $B-R$ in 2.14a, and against the $U-R$ gradient in 2.14b. These figures show that there is no strong relation between the color gradient and the total amount of rotational support. The same color gradients have been plotted against total blue luminosity in 2.14c and 2.14d. The data from this paper and Davis et al. (1985) are plotted with filled symbols. Dusty galaxies are indicated by triangles, while the brightest galaxies (including cD's) are shown as pentagons, and the remainder as squares. The data from Vader et al. (1988) are shown as open squares, and the Franx, Illingworth and Heckman (1989b) data as crosses.*

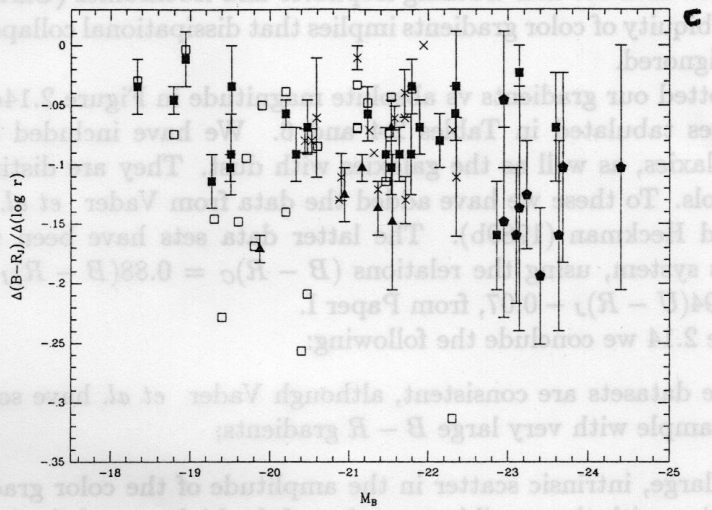

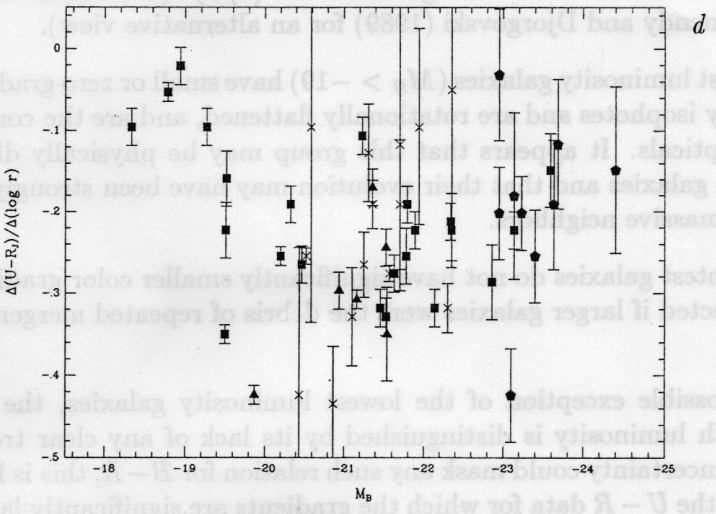

Figure 2.14: *Continued*

noisier U-band ellipticity profiles. The differences in NGC 4697 and 5845 can be explained by dust-absorption along the major axis. This result makes it unlikely that elliptical galaxies were formed in a simple one-stage dissipational collapse, because one should then see non-tracking isophotes and isochromes (Carlberg, 1984). However, the ubiquity of color gradients implies that dissipational collapse/accretion should not be ignored.

We have plotted our gradients vs absolute magnitude in Figure 2.14c and 2.14d, using the values tabulated in Tables 2.4 and 6. We have included the cD and first-ranked galaxies, as well as the galaxies with dust. They are distinguished by different symbols. To these we have added the data from Vader *et al.* and Franx, Illingworth and Heckman (1989b). The latter data sets have been transformed to the Cousins system, using the relations $(B-R)_C = 0.88(B-R)_J - 0.04$ and $(U-R)_C = 0.94(U-R)_J - 0.07$, from Paper I.

From Figure 2.14 we conclude the following:

- The three datasets are consistent, although Vader *et al.* have some galaxies in their sample with very large $B-R$ gradients;
- There is large, intrinsic scatter in the amplitude of the color gradients at all luminosities, with the possible exception of the highest and the lowest;
- There is no significant relation between color gradient and luminosity, nor is there a relation between color gradient and $(v/\sigma)^*$ (cf., Vader *et al.* (1988) and Kormendy and Djorgovski (1989) for an alternative view).
- The lowest luminosity galaxies ($M_B > -19$) have small or zero gradients. They have boxy isophotes and are rotationally flattened, and are the companions of giant ellipticals. It appears that this group may be physically distinct from the other galaxies and that their evolution may have been strongly influenced by their massive neighbors.
- The brightest galaxies do not have significantly smaller color gradients, unlike that expected if larger galaxies were the debris of repeated mergers of smaller galaxies.

With the possible exception of the lowest luminosity galaxies, the correlation of gradient with luminosity is distinguished by its lack of any clear trend. While observational uncertainty could mask any such relation for $B-R$, this is less likely to be the case for the $U-R$ data for which the gradients are significantly larger. Given that there is a trend of color with luminosity, and that color gradients are ubiquitous, it is noteworthy that color gradients themselves do not vary systematically with luminosity.

2.6.3 Other Relations

Position angle twisting appears to depend only upon the intrinsic orientation of the galaxy, and not on luminosity or any other parameters. In Figure 2.15 we have

plotted the amount of position angle twist per dex in radius against ellipticity at $r_e/2$ for all galaxies except the brightest cluster galaxies and the cDs. We see clearly

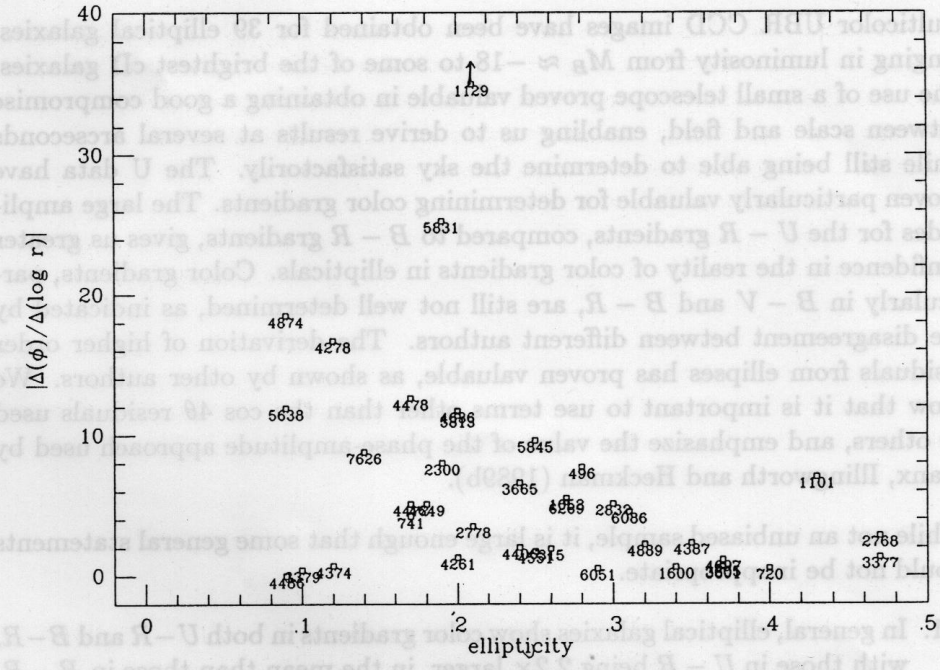

Figure 2.15: *Absolute position angle twist against ellipticity at $r_e/2$, showing that large position angle twists are not seen in flattened galaxies.*

that position angle twists are larger for round galaxies. This is what one would expect for triaxial galaxies. If position angle twists were mainly caused by tidal interactions, flattened galaxies would also have rather large position angle twists.

As was seen in Djorgovski's (1985) thesis data, both ellipticity and major axis position angle vary a lot with radius. An extreme example is NGC 1129, for which we have measured a position angle twist of almost 90°. Such large twists, while rare, are possible for projected triaxial figures for special viewing orientations. In general, galaxies become rounder at smaller radii, even accounting for the effect of seeing. However, the sharp drop towards the center that is seen, e.g., in NGC 4697 and NGC 3377, can be explained entirely by seeing, indicating that it is certainly possible for a galaxy to have very elongated isophotes close to the center.

2.7 Conclusions

With the advent of wide dynamic range linear detectors, surface photometry is beginning to play an important role in delineating the properties of ellipticals. This is particularly true of multicolor surface photometry from which color gradients and

maps can be derived. These data have particular relevance for formation models which involve gaseous processes.

The highlights of this program are:

- Multicolor UBR CCD images have been obtained for 39 elliptical galaxies, ranging in luminosity from $M_B \approx -18$ to some of the brightest cD galaxies. The use of a small telescope proved valuable in obtaining a good compromise between scale and field, enabling us to derive results at several arcseconds while still being able to determine the sky satisfactorily. The U data have proven particularly valuable for determining color gradients. The large amplitudes for the $U-R$ gradients, compared to $B-R$ gradients, gives us greater confidence in the reality of color gradients in ellipticals. Color gradients, particularly in $B-V$ and $B-R$, are still not well determined, as indicated by the disagreement between different authors. The derivation of higher order residuals from ellipses has proven valuable, as shown by other authors. We show that it is important to use terms other than the cos 4θ residuals used by others, and emphasize the value of the phase-amplitude approach used by Franx, Illingworth and Heckman (1989b).

- While not an unbiased sample, it is large enough that some general statements would not be inappropriate.

  1. In general, elliptical galaxies show color gradients in both $U-R$ and $B-R$, with those in $U-R$ being 2.2× larger, in the mean than those in $B-R$. The gradients are always negative, except for a few cases where they are consistent with zero, i.e., the center is always redder than the outer parts. The mean logarithmic gradient in $U-R$, i.e., $\Delta(U-R)/\Delta \log\ r$, is -0.20 ± 0.02 mag per dex in radius, while that in $B-R$ is -0.09 ± 0.02 mag per dex in radius.
  2. $U-R$ gradients correlate with those in $B-R$. The mean of the ratio of the gradients in $U-R$ and $B-R$ is consistent with a decreasing metallicity profile, with a change of metallicity of Δ(Fe/H) of 0.20 per dex in radius.
  3. There is virtually no correlation between absolute magnitude and color gradient, with the possible exception of smaller gradients in the lowest luminosity ellipticals. The scatter at any luminosity is intrinsic, being less than the observational uncertainty, particularly in $U-R$.
  4. Some ellipticals have ellipticity profiles that are consistent with being quite flattened at small radii, i.e., at radii of the order of 1-200 pc (less than a few arcseconds, typically). This effect is often masked by seeing which can effect ellipticity profiles out to large radii (5 – 10 seeing radii).
  5. Dust is common in ellipticals, and may explain some of the reddening in the centers of ellipticals, but not all since line strength gradients provide strong evidence for metallicity changes.

6. Ellipticity, position angle and the higher-order terms show no color dependence, except when the complicating effect of dust is present. While the sensitivity to differences is low, there is no evidence for isochromes to be more flattened than isophotes.
7. Elliptical galaxies have elliptical isophotes, with the high-order (3rd and 4th-order Fourier components) residuals usually not exceeding 1% in amplitude. More typical values are 0.5%, with 4th-order component occurring more commonly. Occasional galaxies, particularly dusty ones, have larger residuals. The more common form for the residuals is a box-shaped distortion characterised by a negative cos 4θ residual, or alternatively by a 4th-order maximum phase-shifted by 45° from the major axis. This appears to be particularly common amongst low-luminosity ellipticals.
8. We confirm that galaxies with disk-like distortions, i.e., positive cos 4θ residuals, or alternatively 4th-order maxima aligned with the major axis show strong rotation and are not strong radio sources. We note that such relations could be biased by the preferential detection of the weak, but rapidly-rotating disk component in those galaxies with disk-like isophotes, and also by the enhancement of both the rotation and the amplitude of the high-order terms in edge-on galaxies.
9. We suggest that the low luminosity ellipticals that are companions to giant elliptical galaxies may form a physically distinct group. They appear to have small or zero color gradients, boxy isophotes and rotation velocities sufficient to account for their flattening. This combination of properties distinguishes them from other ellipticals. Perhaps their evolution has been strongly influenced by the presence of their massive neighbor.

Acknowledgements

The authors want to thank Tjeerd van Albada, Jeanette Barnes, Marijn Franx, Robert Jedrzejewski, Edwin Valentijn and Tim de Zeeuw for their valuable advice and help with this work. We thank S. Djorgovski and Robert Jedrzejewski for access to their unpublished data. RFP acknowledges travel support from the Leids Kerkhoven Bosscha Fonds, and thanks KPNO for its hospitality and support during two visits. The authors are grateful to the director of KPNO for generous allocations of telescope time. This chapter is partially based on observations collected at the European Southern Observatory.

Appendix A: Figures and Tables for Individual Galaxies

The surface brightness, color, ellipticity, and position angle profiles, as well as the sin and cos 3θ and 4θ profiles, resulting from the reduction, calibration and analysis

described in §§2.2-2.5 are plotted in Figure 2.17 for the 39 galaxies studied in this program. The surface brightness, ellipticity, position angle and $B-R$ and $U-R$ color profile data are also tabulated in Table 2.9. The seeing FWHM in arcseconds and the sky background level in R mag arcsec^{-2} are shown on the plots. The seeing FWHM in the three bands is given at the top of each figure. The sky surface brightness in each band is given in Table 2.3. Error bars have not generally been plotted since the major sources of error are systematic. For the $n\theta$ terms where the systematic errors are probably not dominant, an estimate of the uncertainty can be obtained from the scatter of the points. For the color profiles where the errors are systematic and probably comparable to the size of the gradient in many cases (particularly $B-R$), we give the uncertainty that results from a 1% error in the sky level. Since the uncertainty from the sky is most likely highly correlated between the different bands, these error bars represent upper limits to the actual uncertainty. They serve, however, as a useful guide to the confidence level that one can place on the results.

We have not tabulated the 3θ and 4θ terms. If desired these numbers can be obtained from the first author, either in tabulated or in computer-readable form.

Appendix B: Notes on the Individual Galaxies

NGC 315. A bright star at 200″ NW of the galaxy caused a gradient in the background across the frame. The galaxy was offset from the center of the frame so that the star itself did not fall on the frame. A model of the stellar profile of the form $I(r) = I_0(r/r_o)^{-1.5}$ was subtracted in B and R.

NGC 720. This galaxy is quite isolated. We have data from Oct 1982 only. This run generated less reliable data than those of January 1984 and April 1984. The shape parameters were kept constant for r>100″ to allow accurate determination of the luminosity profile.

NGC 741. The data for this galaxy consists of KPNO data in R and U, and B and R frames from the 1.54 m ESO telescope at La Silla, Chile. The ESO-data had considerably better seeing, so that there is a large seeing difference between U on one hand and B and R on the other hand. A star at 9″ N of the core was masked out, as was NGC 742, a companion galaxy 50″ to the North.

NGC 1052. We used the same data from Oct. 1982 as was used in Paper I. The 3θ and 4θ terms show considerable structure inside 20″ ; this probably results from the dust present in this galaxy (see e.g., the detailed study by Davies and Illingworth, 1986).

NGC 1129(AWM 7). This is a very luminous galaxy in a small group. Four companion galaxies in a chain to the south from 25″ to 50″ were masked out causing the galaxy profile to be noisier in this radius range. Note the large position angle twist which is seen in all bands and occurs where the ellipticity

passes through a minimum. However, the twist is not apparent in the phase of the 3rd-order terms with respect to the North (see Figures 2.10 and 2.11). The large position angle twist could be the result of a recent merger between two large galaxies.

NGC 1600. The brightest galaxy in a group. Our KPNO data are of poor quality; the central regions were reobserved at ESO in B and R in December 1986, with seeing of 1.2″ . The internal consistency between both datasets is good. Note that the isophotes become significantly "boxy" between ≈ 8-20″ .

Abell 496. A 5% E-W gradient was subtracted from this galaxy in B and R before analysis. The quality of the data for this galaxy is poor despite the long integration times; the sky is probably uncertain by 2%. The U data is of particularly poor quality as the only frames we have are from the 0.9-m. The R and B frames were taken in cloudy conditions. All the companion galaxies of the central galaxy have been masked out.

NGC 2300. Poor seeing has smoothed out the inner profile. This galaxy is near the north pole so the poor image quality could be partly due to the large zenith distance. The galaxy has a lot of structure in the 3rd and 4th-order terms, probably because of the presence of dust. A 'bump' between 20″ and 60″ in both the position angle and C4 profiles is suggestive of a possible additional 'disk component' in the galaxy.

NGC 2768. This galaxy is very flattened in its outer parts, with the ellipticity rising steadily from the center. The power in the C4 term, in particular, suggests that there may be a disk-like component around 50″ . The galaxy contains a considerable amount of dust (Ebneter and Balick, 1985)). The seeing for this galaxy was estimated from other frames taken on the same night.

NGC 2778. NGC 2779 has been masked out of the frames used here. The signal-to-noise ratio has been greatly improved by the large number of galaxy frames used.

NGC 2832. This is the brightest galaxy in Abell 779. One close companion galaxy at 23″ N has been masked out, as has a disk galaxy at 80″ N. The S3 and S4 terms appear to be significant between 10-20″ .

NGC 3377. Determination of the sky was a problem since this large galaxy was only observed with the 2.1-m telescope. The sky was estimated from the corners of the frame, since the galaxy is quite elongated. The galaxy has a disk on the major axis, which is significant up to ≈30″ , and is boxy at radii larger than 40″ . The luminosity profile changes slope at the position where the galaxy changes from "disk-like" to "boxy". To see whether the isophotes in the inner 40″ were boxy as well (in addition to the presence of a disk) we looked at the higher order terms determined after having masked out the disk.

They were around zero, which means that this galaxy has elliptical isophotes in the inner regions in addition to a disk, and that the isophotes only become boxy after the disk has stopped.

NGC 3379. This galaxy was discussed extensively in paper I. We used the same data here, adding U data from April 1984. Although the amplitudes of the 4th-order terms are small, they are very significant. The deviations from elliptical isophotes are between disk-like and box-like, making the galaxy look like a diamond.

NGC 3605. This is a small galaxy close to NGC 3607. It was necessary to model NGC 3607 in U, B and R and to subtract the models from the frames. The sky determination came from the 0.9-m frames. The isophotes are "boxy" at radii less than 20″ , typical for the small companions of bright ellipticals.

NGC 3665. The strange behavior of the profiles around 10″ results from the sharp dust lane or ring, which is shown in Kotanyi (1979). Except for this feature, presumably responsible for its large IRAS flux, the galaxy looks normal.

NGC 3801. This galaxy is very dusty, with multiple dust lanes that have greatly affected the various profiles. It also has a very large color gradient in $U - R$ and in $B - R$, presumably because of the dust. Note that the amplitude scale for the 3rd and 4th-order terms has been changed to ± 0.10 in Figure 2.17.

NGC 4261. This galaxy rotates about its *major axis* (Davies and Birkinshaw, 1986). It also is the most "boxy" galaxy in this sample, with the largest amplitude for the C4-term, except for those galaxies with prominent dust lanes. Although our profiles agree very well with Bender and Möllenhoff (1987), we were not able to see the dust lane noted by them. The differences between their ellipticity profiles in the three bands suggest that their "dust lane" could have resulted from dividing two frames with non-zero ellipticity and different seeing. Kormendy and Stauffer (1987) noted an almost round patch of dust; our seeing is not good enough to confirm this.

NGC 4278. A relatively small galaxy containing dust (Ebneter and Balick, 1985), and with a large amount of HI (Raimond *et al.*, 1981). The companion to the NE was masked out.

NGC 4374. This large galaxy filled the CCD frame and since it is round in the outer parts the sky was difficult to determine and is uncertain. Note that there are considerable amounts of dust in the central regions (see e.g., Hansen *et al.*, 1984), which affected all profiles. From the 4th-order term, we conclude that NGC 4374 is slightly boxy between 10″ and 50″ . The seeing in U was much worse than the seeing in B and R. The ellipticity profile is somewhat unusual in that it decreases monitonically outward.

NGC 4387. This galaxy has very "boxy" isophotes, without any evidence for dust.

NGC 4406. Again the galaxy completely fills the CCD frame so the sky level is uncertain. NGC 4406 is also a minor-axis rotator, like NGC 4261 (Bender, 1988; Illingworth and Franx, 1989; Franx, Illingworth and Heckman, 1989a), but with a kinematically-distinct core rotating around the minor axis. Apparently the core and the main body of the galaxy are decoupled. Interestingly, the isophotes are "boxy" outside the core, just like NGC 4261.

NGC 4472. This very large elliptical, the brightest in Virgo, was offset on the 0.9-m frame to provide a better estimate of the sky. The galaxy is slightly boxy. This galaxy is rotating slowly around its minor axis, except within the core inside 5″ , where it does not rotate (Franx, Illingworth and Heckman, 1989a).

NGC 4478. A low-luminosity elliptical. A small NS gradient in the background on the B and R frames taken on the 0.9-m telescope was modelled and removed. The quality of the data is good since 2.1-m data was also available. This low-luminosity elliptical shows interesting structure from $r \approx$ 10-50″ , with significant 4th-order terms peaking around 23″ , outside which the position angle changes drastically. This galaxy, a companion to NGC 4486, has very small color gradients.

NGC 4486. This galaxy has been discussed in paper I. The $U - R$ profile flattens in the center, as the bluer nuclear component begins to contribute. This is the roundest galaxy in the sample, and is truly elliptical, since it is one of the only three galaxies in this sample with higher-order terms that are consistent with zero. Since the ellipticity close to the centre is very low, the accuracy of the position angle determination is reduced significantly, especially in U.

NGC 4551. A low luminosity elliptical. Neither the 0.9-m nor the 2.1-m data shows a color gradient in this galaxy. The isophotes are "boxy" between 5-15″ . A spiral companion, NGC 4550, was masked out.

NGC 4636. This galaxy is large and the radius at which the galaxy is only 5% of the night sky surface brightness was not reached. Although very similar to NGC 4649, its isophotes are very elliptical.

NGC 4649. A spiral galaxy, NGC 4647, was masked out in one of the corners. The galaxy is "boxy" from $\approx$ 10″ outward. Its kinematics are regular for a galaxy of this type; it appears not to have a decoupled core (Franx, Illingworth and Heckman, 1989a).

NGC 4697. The galaxy was offset to the north to allow determination of the sky background. NGC 4697 has a very large C4 term, which has a form similar to the ellipticity profile. This indicates that NGC 4697 has a strong major-axis disk. We verified this by subtracting a smooth model from the R frame. This is shown in Figure 2.16a. There are also indications of unusual structure in the outer regions (cf. NGC 3377).

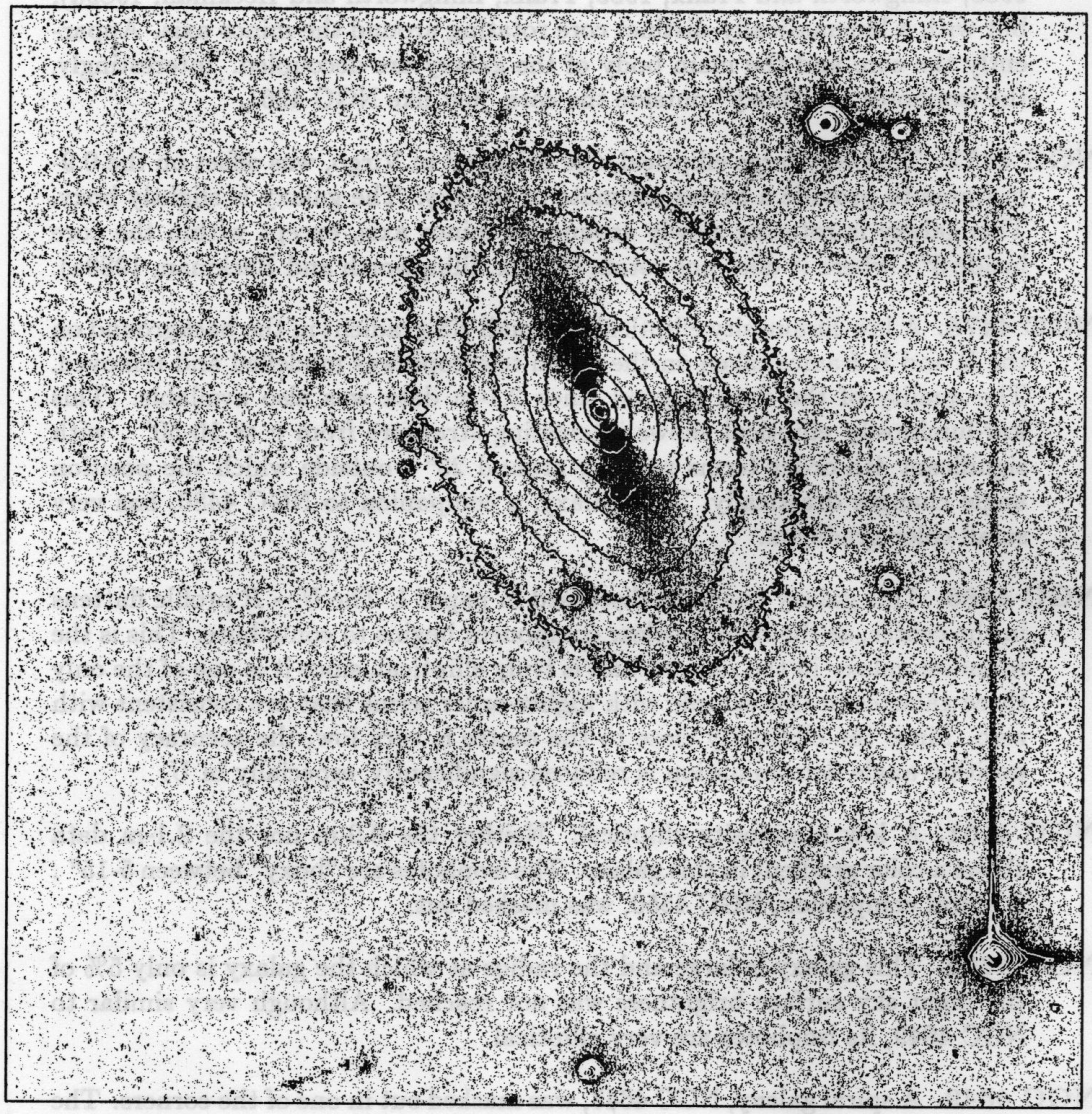

a

Figure 2.16: *A difference image for NGC 4697 (a) showing the "disk-like" structure on the major axis. A model of the galaxy, based on the surface photometry, with the assumption that NGC 4697 can be represented by ellipses, has been subtracted from the data frame, leaving the 3rd and 4th-order residual structure. In (b) we show a grey scale image of the inner parts of NGC 1129, a galaxy with a position angle twist of almost 90°.*

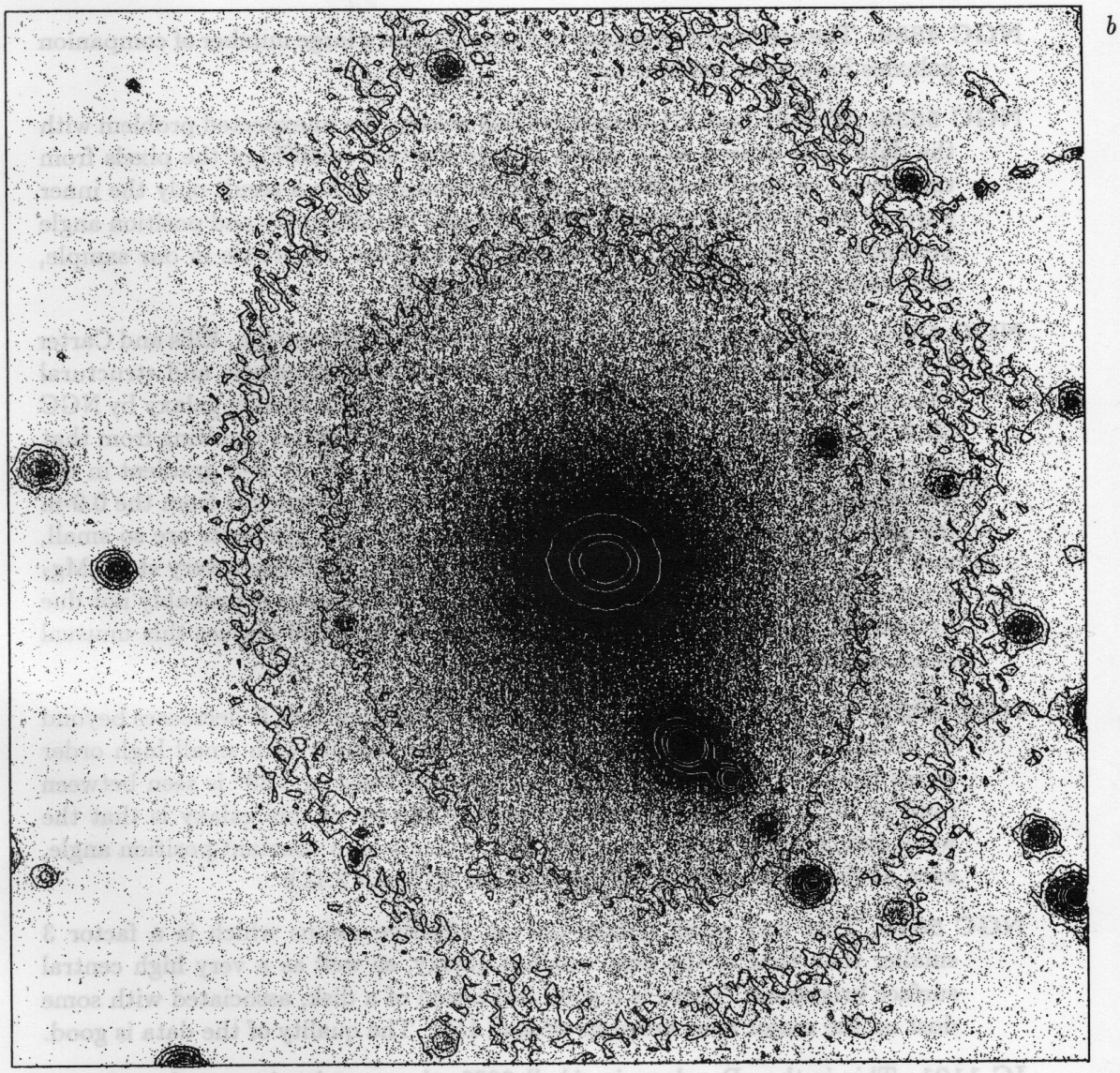

Figure 2.16: *Continued.*

NGC 4874. This elliptical is one of the two brightest in the Coma cluster. The data is of rather poor quality, due to its low surface brightness. A large number of companion galaxies have been removed, making the higher order terms difficult to interpret.

NGC 4889. The other central galaxy in Coma. Again a large number of companion galaxies have been masked out.

NGC 5638. We only have 2.1-m data for this galaxy. An unexpected problem with the data in U caused us to delete a large fraction ($\simeq$40%) of the pixels from this frame, so the U results are less than optimum. As a result only the inner parts of the $U-R$ color profile are shown and the ellipticity and position angle profiles in U are omitted. It is one of the roundest ellipticals in our sample, and shows no significant higher order structure.

NGC 5813. This galaxy has been studied previously by Efstathiou, Ellis and Carter (1982). Kormendy (1984) argued that the unusual kinematic and structural character of the core was the result of the accretion of a smaller galaxy by NGC 5813. There appear to be no large scale structural features resulting from that accretion, except for some dust in the nuclear regions. A N-S gradient in the background on the B and R frames was modeled and removed from the 0.9-m telescope frames. It is interesting that while the color gradients are so small, and are consistent between 0.9-m and 2.1-m, NGC 5813 has a very steep Mg_2 gradient (Gorgas and Efstathiou, 1987). This discrepancy is probably not due to dust. A future paper (Peletier, 1989, Chapter 6) will discuss this unusual characteristic.

NGC 5831. The ellipticity profile is somewhat unusual in that it decreases beyond 8″ , making NGC 5831 the only galaxy in the sample with small high order terms and a decreasing ellipticity. An isophote twist of >20° is seen between radii of 10-25″ . A particularly interesting feature of this galaxy is that the weak disk, initially along the major axis, remains at a constant position angle, even as the major axis skews (see Figures 2.10 and 2.11).

NGC 5845. This very small galaxy has an effective radius which is a factor 3 smaller than that of the next smallest galaxy, as well as a very high central surface brightness. There is a good indication of a disk, associated with some dust on the major axis, between $\approx$5 and 15″ . The quality of the data is good.

IC 1101. This is the cD galaxy in Abell 2029; the most luminous galaxy in our sample, at a redshift z of almost 0.08. The photometry is a compilation of a large number of frames, taken with both telescopes. The galaxy is a low surface brightness object, as can be expected for a cD. Many companion galaxies have been deleted. The ellipticity increases very rapidly outward from the center. The $n\theta$ terms are uncertain, although the agreement between B and R is good. Due to the lack of aperture photometry our absolute calibration is uncertain in U.

NGC 6051 (AWM 4) The galaxy was offset to the W on the frame to avoid a bright star. The data do not extend to very large radii, since only 2.1-m data were taken. A large number of companion galaxies have been masked out.

NGC 6086 The central galaxy in Abell 2162. The frame taken on the 2.1-m was positioned between two bright stars; one at 42″ to the SE and the other at 170″ to the SW. Many companion galaxies were masked out.

NGC 6269 (AWM 5) A highly luminous galaxy with data from both telescopes. Many companion galaxies were masked out.

NGC 7626. One of the two brightest ellipticals in the Pegasus I cluster – paired with the higher luminosity NGC 7619. The only data for this galaxy were taken in the Oct. 1982 run. It is not of the quality of the later data. Beyond 60″ the shape-parameters in B have been kept constant. Although the galaxy itself rotates quite slowly, its core rotates with an amplitude of ≈ 40 kms^{-1} (Jedrzejewski and Schecter, 1988). There is also shell structure to the east of the galaxy, indicative of an interaction/acquisition.

Addresses

Michael Cawson, Astromed, Cambridge Science Park, Cambridge, UK

Roger L. Davies, Department of Astrophysics, Nuclear Physics Laboratory, Keble Rd., Oxford, OX1 3RH, UK

Lindsey Davis, Kitt Peak National Observatory, PO Box 26732, Tucson, AZ 85726-6732, USA

Garth D. Illingworth, Lick Observatory, University of California, Santa Cruz, CA 95064, USA

Reynier F. Peletier, Kapteyn Laboratorium, University of Groningen, Postbus 800, 9700 AV Groningen, The Netherlands

Table 2.9: Galaxy parameters

NGC 315					
Radius	μ_R	ϵ	ϕ	$B-R$	$U-R$
(1)	(2)	(3)	(4)	(5)	(6)
3.8	17.84	0.207	41.0	– –	– –
4.6	18.05	0.221	41.7	– –	– –
5.3	18.21	0.225	42.1	– –	– –
5.8	18.32	0.235	42.6	– –	– –
6.4	18.44	0.249	43.5	1.80	– –
7.0	18.56	0.254	44.0	1.80	– –
7.7	18.69	0.261	43.2	1.79	2.45
8.5	18.82	0.269	43.0	1.79	2.41
9.3	18.95	0.274	43.3	1.79	2.43
10.2	19.08	0.276	42.6	1.79	2.43
11.3	19.22	0.279	42.8	1.79	2.43
12.4	19.35	0.283	42.7	1.78	2.42
13.6	19.49	0.283	42.5	1.79	2.44
15.0	19.63	0.284	42.0	1.78	2.46
16.5	19.78	0.276	42.7	1.78	2.46
18.2	19.94	0.272	42.7	1.78	2.49
20.0	20.10	0.267	42.8	1.77	2.42
22.0	20.27	0.264	42.7	1.77	2.39
24.2	20.46	0.251	43.0	1.76	2.43
26.6	20.63	0.253	42.8	1.77	2.36
29.2	20.81	0.247	43.1	1.76	2.33
32.2	20.98	0.251	43.6	1.77	2.40
35.4	21.14	0.256	45.0	1.77	2.38
38.9	21.29	0.274	44.6	1.78	2.33
42.8	21.47	0.261	46.1	1.77	2.32
47.1	21.66	0.261	43.0	1.75	2.18
51.8	21.84	0.266	44.4	1.75	2.34
57.0	22.06	0.248	45.0	1.75	– –
62.7	22.28	0.240	45.2	1.72	– –
69.0	22.51	0.226	44.3	1.71	– –
75.8	22.77	0.232	44.2	1.69	– –
83.4	22.96	0.248	44.2	– –	– –
91.8	23.16	0.251	48.2	– –	– –

Notes to Table 9:
Column (1) gives the radius along the major axis in arcsec, column (2) the surface brightness in Cousins R in mag arcsec^{-2}, and column (3) the ellipticity $1-b/a$. The position angle of the major axis measured from N through E is given in column (4), while columns (5) and (6) list the $B-R$ and $U-R$ colors in mag arcsec^{-2}.

Table 2.9: Galaxy parameters, cont.

NGC 720					
Radius	μ_R	ϵ	ϕ	$B-R$	$U-R$
(1)	(2)	(3)	(4)	(5)	(6)
3.1	16.82	– –	– –	1.67	– –
3.8	16.96	– –	– –	1.66	– –
4.6	17.12	– –	– –	1.66	2.32
5.3	17.27	0.257	141.9	1.65	2.33
5.8	17.38	0.266	142.3	1.64	2.31
6.4	17.49	0.279	142.3	1.63	2.29
7.0	17.62	0.292	142.4	1.63	2.27
7.7	17.74	0.308	142.3	1.63	2.25
8.5	17.88	0.315	142.1	1.62	2.25
9.3	18.01	0.326	141.8	1.62	2.23
10.2	18.17	0.333	142.0	1.60	2.21
11.3	18.31	0.344	141.7	1.61	2.19
12.4	18.46	0.355	141.8	1.60	2.19
13.6	18.61	0.365	141.8	1.60	2.18
15.0	18.76	0.380	142.3	1.59	2.18
16.5	18.90	0.394	141.9	1.59	2.15
18.2	19.06	0.398	142.0	1.59	2.15
20.0	19.23	0.402	142.0	1.58	2.14
22.0	19.39	0.407	141.8	1.58	2.13
24.2	19.56	0.412	141.6	1.57	2.14
26.6	19.74	0.414	141.7	1.56	2.10
29.2	19.92	0.418	142.0	1.56	2.08
32.2	20.09	0.423	141.8	1.56	2.07
35.4	20.27	0.430	141.9	1.57	2.02
38.9	20.45	0.436	141.8	1.56	1.99
42.8	20.62	0.442	141.9	1.55	2.04
47.1	20.81	0.442	138.6	1.54	1.93
51.8	21.07	0.442	138.6	1.49	1.84
57.0	21.11	0.476	140.8	1.55	2.04
62.7	21.30	0.476	140.3	1.55	1.95
69.0	21.49	0.477	141.1	1.56	2.06
75.8	21.72	0.463	141.8	1.53	– –
83.4	21.94	0.456	142.4	1.52	– –
91.8	22.17	0.456	143.8	1.52	– –
101.0	22.40	0.443	143.8	1.55	– –
111.1	22.65	0.443	145.6	– –	– –
122.2	22.91	0.437	136.4	– –	– –

Table 2.9: Galaxy parameters, cont.

NGC 741					
Radius	μ_R	ϵ	ϕ	$B-R$	$U-R$
(1)	(2)	(3)	(4)	(5)	(6)
2.5	17.80	0.056	84.4	1.58	– –
3.0	18.03	0.081	85.7	1.58	– –
3.6	18.27	0.091	89.8	1.57	– –
4.4	18.51	0.122	90.5	1.56	– –
5.1	18.70	0.134	92.5	1.56	– –
5.6	18.81	0.144	90.0	1.56	– –
6.2	18.96	0.125	88.3	1.57	– –
6.8	19.11	0.129	90.1	1.53	– –
7.5	19.24	0.134	89.6	1.53	2.36
8.2	19.37	0.140	89.1	1.52	2.34
9.0	19.52	0.144	86.7	1.52	2.29
9.9	19.64	0.157	85.5	1.53	2.34
11.3	19.83	0.158	85.8	1.51	2.22
12.4	19.94	0.169	86.3	1.51	2.22
13.6	20.09	0.175	84.7	1.48	2.32
15.0	20.22	0.182	86.6	1.56	2.28
16.5	20.33	0.188	87.6	1.55	2.27
18.2	20.50	0.183	85.8	1.48	2.17
20.0	20.66	0.170	88.7	1.54	2.16
22.0	20.82	0.167	89.2	1.58	2.19
24.2	20.97	0.175	89.9	1.47	2.15
26.6	21.17	0.157	92.2	1.42	2.12
29.2	21.36	0.159	92.6	1.41	2.18
32.2	21.54	0.150	92.6	1.45	2.07
35.4	21.71	0.150	92.5	1.42	– –
38.9	21.92	0.142	91.2	1.44	– –
42.8	22.10	0.164	88.9	1.29	– –
47.1	22.33	0.162	91.0	1.34	– –
51.8	22.55	0.163	92.1	1.40	– –
57.0	22.71	0.188	94.7	– –	– –

Table 2.9: Galaxy parameters, cont.

NGC 1052					
Radius	μ_R	ϵ	ϕ	$B-R$	$U-R$
(1)	(2)	(3)	(4)	(5)	(6)
3.8	16.75	– –	– –	1.71	2.37
4.6	17.00	0.228	113.3	1.69	2.34
5.3	17.20	0.232	111.9	1.67	2.33
5.8	17.34	0.227	111.6	1.66	2.31
6.4	17.47	0.229	112.6	1.66	2.28
7.0	17.61	0.236	112.7	1.65	2.26
7.7	17.74	0.237	112.3	1.64	2.23
8.5	17.87	0.246	112.7	1.64	2.25
9.3	17.98	0.260	113.1	1.63	2.24
10.2	18.10	0.269	113.5	1.62	2.23
11.3	18.23	0.276	113.3	1.63	2.24
12.4	18.37	0.275	114.3	1.61	2.20
13.6	18.51	0.276	113.7	1.61	2.20
15.0	18.66	0.279	114.6	1.61	2.20
16.5	18.81	0.286	115.2	1.62	2.19
18.2	18.97	0.293	114.9	1.62	2.19
20.0	19.13	0.299	114.8	1.61	2.16
22.0	19.28	0.313	114.4	1.60	2.12
24.2	19.44	0.325	114.8	1.60	2.16
26.6	19.59	0.335	115.6	1.61	2.13
29.2	19.77	0.336	115.8	1.61	2.14
32.2	19.95	0.339	115.7	1.61	2.09
35.4	20.16	0.330	116.1	1.59	2.11
38.9	20.40	0.313	116.4	1.57	2.11
42.8	20.62	0.312	116.8	1.60	2.15
47.1	20.87	0.303	117.3	1.57	2.04
51.8	21.15	0.281	117.0	1.56	1.92
57.0	21.41	0.273	117.6	1.56	1.97
62.7	21.68	0.264	117.7	1.54	1.88
69.0	21.97	0.236	117.3	1.54	– –
75.8	22.26	0.220	119.2	1.51	– –
83.4	22.52	0.210	120.1	1.54	– –
91.8	22.80	0.184	121.8	– –	– –

Table 2.9: Galaxy parameters, cont.

NGC 1129					
Radius	μ_R	ϵ	ϕ	$B-R$	$U-R$
(1)	(2)	(3)	(4)	(5)	(6)
3.8	18.67	0.181	4.1	1.58	– –
4.6	18.90	0.167	6.0	1.57	2.20
5.3	19.07	0.155	6.7	1.56	2.22
5.8	19.18	0.158	6.4	1.57	2.20
6.4	19.29	0.157	8.3	1.56	2.16
7.0	19.40	0.148	7.3	1.56	2.14
7.7	19.51	0.143	11.1	1.55	2.18
8.5	19.62	0.137	12.0	1.54	2.16
9.3	19.73	0.125	9.0	1.55	2.18
10.2	19.83	0.128	17.3	1.55	2.17
11.3	19.94	0.106	22.7	1.55	2.20
12.4	20.05	0.099	30.0	1.55	2.19
13.6	20.13	0.099	38.8	1.56	2.15
15.0	20.21	0.115	47.5	1.57	2.20
16.5	20.29	0.135	54.4	1.59	2.28
18.2	20.42	0.111	64.9	1.54	2.16
20.0	20.51	0.136	70.3	1.53	2.34
22.0	20.63	0.150	70.2	1.54	2.20
24.2	20.72	0.172	73.8	1.55	2.24
26.6	20.85	0.182	76.6	1.52	2.18
29.2	20.96	0.188	72.2	1.52	2.16
32.2	21.07	0.197	70.1	1.51	2.22
35.4	21.19	0.193	75.5	1.49	2.14
38.9	21.25	0.241	75.2	1.53	2.09
42.8	21.40	0.227	77.2	1.51	2.05
47.1	21.55	0.229	81.1	1.48	1.96
51.8	21.68	0.257	81.4	1.48	2.01
57.0	21.82	0.274	83.6	1.47	– –
62.7	21.95	0.299	82.6	1.46	– –
69.0	22.11	0.316	84.5	1.48	– –
75.8	22.26	0.330	86.1	1.47	– –
83.4	22.45	0.319	86.0	1.42	– –
91.8	22.61	0.360	86.1	1.43	– –
101.0	22.76	0.388	85.4	– –	– –
111.1	22.93	0.409	85.8	– –	– –

Table 2.9: Galaxy parameters, cont.

NGC 1600					
Radius	μ_R	ϵ	ϕ	$B-R$	$U-R$
(1)	(2)	(3)	(4)	(5)	(6)
1.7	17.32	– –	– –	1.56	– –
2.1	17.39	– –	– –	1.56	– –
2.5	17.49	– –	– –	1.55	– –
3.0	17.61	0.245	8.5	1.55	– –
3.7	17.75	0.255	8.7	1.55	– –
4.4	17.92	0.268	8.4	1.55	– –
5.1	18.06	0.283	8.7	1.54	– –
5.6	18.17	0.296	8.1	1.55	2.30
6.2	18.27	0.311	8.2	1.53	2.29
6.8	18.41	0.323	8.6	1.55	2.29
7.5	18.52	0.337	8.6	1.55	2.28
8.2	18.64	0.346	8.6	1.55	2.27
9.0	18.78	0.350	8.5	1.55	2.27
9.9	18.91	0.359	8.1	1.55	2.29
11.3	19.07	0.360	8.7	1.56	2.31
12.4	19.23	0.352	7.6	1.56	2.25
13.6	19.37	0.356	7.5	1.57	2.24
15.0	19.54	0.348	8.0	1.55	2.19
16.5	19.71	0.339	7.8	1.56	2.25
18.2	19.88	0.338	7.4	1.55	2.22
20.0	20.06	0.332	7.1	1.52	2.18
22.0	20.23	0.327	6.7	1.49	2.09
24.2	20.40	0.326	7.7	1.57	2.10
26.6	20.57	0.322	7.5	1.55	2.20
29.2	20.74	0.323	7.7	1.52	2.19
32.2	20.91	0.320	7.5	1.52	2.22
35.4	21.06	0.326	7.0	1.52	– –
38.9	21.22	0.327	6.4	1.53	– –
42.8	21.46	0.254	6.4	1.47	– –
47.1	21.59	0.295	6.4	1.54	– –
51.8	21.79	0.300	12.5	1.52	– –
57.0	21.98	0.269	8.4	1.54	– –
62.7	22.19	0.269	8.2	1.56	– –
69.0	22.44	0.272	7.2	– –	– –
75.8	22.67	0.268	7.9	– –	– –
83.4	22.80	0.304	7.9	– –	– –
91.8	22.98	0.317	7.4	– –	– –
101.0	23.22	0.317	7.4	– –	– –
111.1	23.44	0.304	8.1	– –	– –
122.2	23.85	0.314	9.2	– –	– –

Table 2.9: Galaxy parameters, cont.

Abell 496 cD					
Radius	μ_R	ϵ	ϕ	$B-R$	$U-R$
(1)	(2)	(3)	(4)	(5)	(6)
3.1	19.17	– –	– –	– –	– –
3.8	19.38	0.142	173.6	1.62	– –
4.6	19.58	0.153	173.2	1.64	– –
5.3	19.74	0.166	173.1	1.64	2.35
5.8	19.87	0.166	173.5	1.61	2.26
6.4	19.99	0.179	173.2	1.60	2.22
7.0	20.12	0.178	174.2	1.59	2.24
7.7	20.23	0.186	172.3	1.60	2.25
8.5	20.37	0.190	152.9	1.58	2.21
9.3	20.49	0.182	153.3	1.57	2.27
10.2	20.62	0.195	172.8	1.56	2.19
11.3	20.71	0.202	152.9	1.59	2.24
12.4	20.90	0.186	172.0	1.53	2.15
13.6	20.98	0.208	154.5	1.59	2.24
15.0	21.13	0.212	172.3	1.55	2.23
16.5	21.34	0.202	157.3	1.51	2.14
18.2	21.42	0.215	158.5	1.56	2.13
20.0	21.61	0.225	178.8	1.52	2.03
22.0	21.71	0.242	176.6	1.53	2.21
24.2	21.84	0.265	177.5	1.52	2.21
26.6	21.99	0.274	177.2	1.53	2.18
29.2	22.14	0.271	178.0	1.51	– –
32.2	22.29	0.282	177.3	1.55	– –
35.4	22.44	0.296	177.3	– –	– –
38.9	22.61	0.302	178.0	– –	– –
42.8	22.83	0.302	178.0	– –	– –
47.1	22.92	0.354	172.6	– –	– –

Table 2.9: Galaxy parameters, cont.

NGC 2300					
Radius	μ_R	ϵ	ϕ	$B-R$	$U-R$
(1)	(2)	(3)	(4)	(5)	(6)
5.8	17.94	0.161	73.0	1.68	– –
6.4	18.08	0.161	73.3	1.68	– –
7.0	18.23	0.163	73.0	1.68	– –
7.7	18.37	0.170	72.8	1.68	2.43
8.5	18.52	0.177	73.0	1.68	2.42
9.3	18.66	0.181	72.5	1.68	2.44
10.2	18.82	0.181	72.2	1.68	2.43
11.3	18.98	0.181	72.7	1.68	2.41
12.4	19.15	0.175	73.9	1.67	2.38
13.6	19.33	0.165	73.5	1.67	2.37
15.0	19.53	0.157	75.2	1.66	2.39
16.5	19.72	0.155	75.0	1.66	2.33
18.2	19.91	0.148	75.5	1.65	2.32
20.0	20.09	0.147	75.2	1.66	2.32
22.0	20.27	0.149	75.2	1.64	2.26
24.2	20.45	0.150	77.4	1.64	2.34
26.6	20.62	0.152	80.2	1.63	2.33
29.2	20.77	0.169	82.9	1.65	2.23
32.2	20.95	0.158	84.4	1.61	2.19
35.4	21.11	0.159	85.4	1.61	2.31
38.9	21.26	0.174	88.6	1.60	2.18
42.8	21.42	0.178	88.4	1.60	2.20
47.1	21.63	0.158	84.5	1.56	– –
51.8	21.84	0.157	79.7	1.58	– –
57.0	22.03	0.164	79.2	1.56	– –
62.7	22.19	0.179	80.6	1.56	– –
69.0	22.39	0.172	78.3	1.56	– –
75.8	22.59	0.188	72.3	– –	– –

Table 2.9: Galaxy parameters, cont.

NGC 2768					
Radius	μ_R	ϵ	ϕ	$B-R$	$U-R$
(1)	(2)	(3)	(4)	(5)	(6)
3.6	17.21	– –	– –	1.52	2.34
5.0	17.49	0.251	96.7	1.48	2.28
6.4	17.73	0.283	96.1	1.46	2.23
7.9	17.92	0.302	96.6	1.46	2.23
9.5	18.12	0.316	95.8	1.45	2.21
11.4	18.29	0.332	95.2	1.45	2.18
13.5	18.47	0.354	94.8	1.44	2.16
15.8	18.66	0.364	94.3	1.42	2.13
18.3	18.82	0.380	94.5	1.43	2.14
21.1	19.00	0.396	93.7	1.41	2.12
24.0	19.15	0.419	93.9	1.43	2.12
27.1	19.31	0.436	94.2	1.42	2.11
30.9	19.48	0.458	94.4	1.41	2.10
34.5	19.62	0.472	94.4	1.41	2.09
39.2	19.80	0.485	93.9	1.41	2.06
44.5	19.98	0.500	93.4	1.42	2.06
49.7	20.18	0.503	93.5	1.39	2.05
55.6	20.35	0.510	93.5	1.40	2.02
61.2	20.51	0.517	93.2	1.40	1.99
67.3	20.69	0.522	93.7	1.38	1.93
75.4	20.89	0.537	93.6	1.38	1.93
85.1	21.09	0.551	93.1	1.38	1.89
95.4	21.27	0.569	92.9	1.36	1.85
105.0	21.43	0.581	92.7	1.35	– –
115.4	21.58	0.594	92.5	1.36	– –
128.9	21.81	0.598	92.5	1.34	– –
144.2	22.06	0.601	92.4	1.35	– –
158.7	22.34	0.583	91.7	1.34	– –
174.4	22.63	0.572	91.6	1.32	– –
193.8	23.01	0.537	– –	1.30	– –

Table 2.9: Galaxy parameters, cont.

NGC 2778					
Radius	μ_R	ϵ	ϕ	$B-R$	$U-R$
(1)	(2)	(3)	(4)	(5)	(6)
3.2	18.29	0.148	45.8	1.81	2.18
4.0	18.58	0.178	45.6	1.80	2.15
4.7	18.82	0.205	45.4	1.80	2.15
5.4	19.04	0.220	45.8	1.80	2.11
6.0	19.20	0.218	45.3	1.79	2.09
6.6	19.36	0.214	45.2	1.79	2.10
7.2	19.52	0.209	44.5	1.78	2.11
7.9	19.68	0.206	44.2	1.78	2.10
8.7	19.83	0.206	43.6	1.77	2.07
9.6	19.98	0.204	44.0	1.76	2.09
10.6	20.13	0.207	43.9	1.77	2.07
11.6	20.28	0.212	43.5	1.76	2.07
12.8	20.43	0.216	44.3	1.76	2.05
14.1	20.59	0.218	43.3	1.76	2.03
15.5	20.76	0.222	43.3	1.74	2.07
17.0	20.92	0.229	43.7	1.74	1.97
18.7	21.10	0.239	43.2	1.74	1.99
20.6	21.30	0.236	43.1	1.73	1.97
22.7	21.52	0.230	43.1	1.72	2.04
24.9	21.75	0.227	42.4	1.69	2.00
27.4	22.03	0.216	42.6	1.68	2.08
30.2	22.36	0.207	42.6	1.66	2.05
33.2	22.71	0.214	41.9	1.68	– –
36.5	23.11	0.207	43.1	1.74	– –
40.1	23.58	0.196	42.1	– –	– –

Table 2.9: Galaxy parameters, cont.

NGC 2832					
Radius	μ_R	ϵ	ϕ	$B-R$	$U-R$
(1)	(2)	(3)	(4)	(5)	(6)
3.1	18.01	– –	– –	1.53	2.17
3.8	18.27	– –	– –	1.52	2.17
4.6	18.54	0.173	150.1	1.51	2.16
5.3	18.74	0.185	151.3	1.51	2.14
5.8	18.88	0.192	153.7	1.51	2.13
6.4	19.04	0.190	155.0	1.49	2.12
7.0	19.20	0.193	156.4	1.48	2.09
7.7	19.34	0.204	157.8	1.48	2.09
8.5	19.50	0.209	157.9	1.47	2.10
9.3	19.66	0.211	158.0	1.46	2.06
10.2	19.81	0.222	158.3	1.47	2.08
11.3	19.95	0.231	158.6	1.46	2.05
12.4	20.08	0.245	160.8	1.47	2.00
13.6	20.23	0.268	160.3	1.46	2.00
15.0	20.35	0.279	159.4	1.46	2.07
16.5	20.49	0.280	159.7	1.44	2.02
18.2	20.64	0.289	158.4	1.44	2.02
20.0	20.79	0.290	159.3	1.45	1.96
22.0	20.95	0.280	160.5	1.44	1.99
24.2	21.12	0.280	159.6	1.43	2.00
26.6	21.31	0.268	161.1	1.42	1.96
29.2	21.47	0.293	158.8	1.42	1.93
32.2	21.64	0.300	158.1	1.43	1.86
35.4	21.79	0.313	159.2	1.40	1.90
38.9	21.92	0.320	161.2	1.42	1.96
42.8	22.06	0.337	161.6	1.38	1.85
47.1	22.21	0.361	160.6	1.36	1.84
51.8	22.37	0.378	158.8	1.35	1.91
57.0	22.52	0.374	160.3	1.33	– –
62.7	22.63	0.381	163.1	1.36	– –
69.0	22.78	0.428	160.6	1.33	– –
75.8	22.95	0.431	159.7	1.27	– –
83.4	23.15	0.438	159.8	– –	– –
91.8	23.36	0.448	159.0	– –	– –

Table 2.9: Galaxy parameters, cont.

NGC 3377					
Radius	μ_R	ϵ	ϕ	$B-R$	$U-R$
(1)	(2)	(3)	(4)	(5)	(6)
1.8	15.74	– –	– –	– –	– –
2.2	15.99	– –	– –	1.58	– –
2.7	16.24	– –	– –	1.58	– –
3.2	16.49	– –	– –	1.58	– –
3.9	16.75	0.445	38.3	1.58	– –
4.7	17.01	0.468	38.7	1.58	– –
5.5	17.21	0.479	39.0	1.57	2.19
6.0	17.36	0.482	39.1	1.57	2.17
6.6	17.50	0.481	39.2	1.57	2.14
7.3	17.64	0.486	39.3	1.57	2.14
8.0	17.79	0.488	39.4	1.56	2.12
8.8	17.94	0.485	39.2	1.55	2.11
9.7	18.08	0.487	38.9	1.55	2.07
10.7	18.22	0.488	38.8	1.53	2.07
11.7	18.37	0.488	38.6	1.53	2.05
12.9	18.51	0.490	38.5	1.53	2.02
14.2	18.65	0.492	38.7	1.52	2.01
15.6	18.78	0.498	38.9	1.51	2.01
17.2	18.92	0.503	38.8	1.51	2.00
18.9	19.06	0.504	38.9	1.51	1.98
20.8	19.19	0.510	39.1	1.52	1.98
22.9	19.33	0.514	39.2	1.51	1.97
25.2	19.48	0.514	39.4	1.50	1.96
27.7	19.65	0.511	39.5	1.49	1.94
30.5	19.82	0.512	39.3	1.50	1.94
33.5	20.00	0.509	39.2	1.50	1.93
36.9	20.21	0.500	39.2	1.49	1.91
40.6	20.43	0.488	39.2	1.50	1.91
44.6	20.67	0.471	39.2	1.50	1.89
49.1	20.91	0.457	39.0	1.48	1.86
54.0	21.16	0.444	39.0	1.49	1.84
59.4	21.41	0.429	39.0	1.48	1.82
65.3	21.68	0.414	40.1	1.45	1.75
71.8	21.97	0.393	41.2	1.45	1.82
79.0	22.21	0.393	41.2	1.48	1.71
86.9	22.48	0.393	41.2	– –	– –
95.6	22.76	0.393	41.2	– –	– –

Table 2.9: Galaxy parameters, cont.

NGC 3379					
Radius	μ_R	ϵ	ϕ	$B-R$	$U-R$
(1)	(2)	(3)	(4)	(5)	(6)
4.0	16.30	0.093	67.7	1.65	2.33
4.9	16.57	0.079	73.4	1.64	2.33
5.5	16.74	0.077	74.9	1.62	2.31
6.1	16.88	0.075	75.0	1.61	2.30
6.7	17.03	0.075	73.9	1.61	2.30
7.4	17.17	0.074	74.1	1.61	2.29
8.1	17.31	0.072	74.4	1.61	2.28
8.9	17.46	0.073	73.7	1.61	2.26
9.8	17.62	0.074	73.2	1.61	2.25
10.7	17.78	0.075	72.7	1.61	2.24
11.8	17.94	0.076	72.5	1.61	2.24
13.0	18.11	0.076	71.3	1.61	2.24
14.3	18.29	0.076	70.6	1.60	2.20
15.7	18.47	0.078	70.3	1.60	2.20
17.3	18.66	0.078	70.4	1.60	2.18
19.0	18.84	0.083	69.5	1.59	2.16
20.9	19.01	0.090	69.9	1.59	2.17
23.0	19.17	0.098	70.1	1.58	2.15
25.3	19.32	0.108	70.1	1.59	2.14
27.9	19.46	0.113	69.4	1.58	2.13
30.6	19.59	0.121	69.8	1.59	2.14
33.7	19.72	0.127	69.8	1.58	2.13
37.1	19.86	0.129	69.5	1.58	2.12
40.8	20.01	0.132	69.7	1.57	2.11
44.9	20.17	0.132	70.3	1.58	2.09
49.3	20.36	0.133	70.5	1.58	2.09
54.3	20.56	0.129	70.9	1.57	2.09
59.7	20.76	0.130	71.0	1.57	2.07
65.7	20.98	0.135	69.4	1.57	2.06
72.2	21.21	0.131	69.0	1.56	2.03
79.5	21.43	0.126	70.0	1.55	1.99
87.3	21.66	0.124	70.3	1.56	2.02
96.0	21.92	0.124	70.8	1.55	2.00
105.6	22.18	0.120	71.5	1.54	1.98
116.2	22.40	0.133	70.4	1.56	– –
127.8	22.64	0.143	72.4	1.54	– –
140.6	22.85	0.158	72.5	– –	– –
154.6	23.11	0.153	78.1	– –	– –
169.5	23.31	0.148	80.2	– –	– –

Table 2.9: Galaxy parameters, cont.

NGC 3605					
Radius	μ_R	ϵ	ϕ	$B-R$	$U-R$
(1)	(2)	(3)	(4)	(5)	(6)
3.2	18.20	– –	– –	1.43	1.85
3.9	18.47	– –	– –	1.42	1.84
4.6	18.72	– –	– –	1.41	1.82
5.4	18.92	– –	– –	1.41	1.82
5.9	19.05	0.305	19.3	1.41	1.83
6.5	19.19	0.320	19.1	1.42	1.82
7.1	19.33	0.332	18.9	1.41	1.80
7.9	19.48	0.342	19.1	1.41	1.83
8.6	19.64	0.353	18.6	1.41	1.81
9.5	19.79	0.362	18.4	1.40	1.81
10.5	19.96	0.371	18.6	1.40	1.82
11.5	20.12	0.383	18.5	1.41	1.80
12.7	20.29	0.394	18.3	1.41	1.77
13.9	20.47	0.401	18.4	1.40	1.76
15.3	20.65	0.411	18.1	1.40	1.78
16.8	20.86	0.416	18.1	1.40	1.82
18.5	21.10	0.417	17.8	1.41	1.79
20.4	21.36	0.418	17.3	1.42	1.79
22.4	21.64	0.418	17.7	1.39	1.72
24.6	21.87	0.434	18.3	1.40	1.78
27.1	22.23	0.425	18.8	1.38	1.84
29.8	22.67	0.402	19.2	1.40	– –
32.8	23.09	0.384	19.4	1.37	– –

Table 2.9: Galaxy parameters, cont.

NGC 3665					
Radius (1)	μ_R (2)	ϵ (3)	ϕ (4)	$B-R$ (5)	$U-R$ (6)
3.1	17.28	– –	– –	1.62	2.17
3.8	17.50	– –	– –	1.61	2.14
4.6	17.73	– –	– –	1.61	2.13
5.3	17.90	0.359	26.7	1.61	2.14
5.8	18.03	0.365	26.6	1.61	2.15
6.4	18.16	0.372	26.3	1.62	2.15
7.0	18.28	0.377	26.3	1.62	2.15
7.7	18.42	0.378	25.5	1.61	2.12
8.5	18.57	0.357	26.4	1.59	2.11
9.3	18.78	0.049	15.5	1.52	2.06
10.2	18.86	0.079	19.2	1.57	2.12
11.3	18.94	0.117	22.8	1.63	2.19
12.4	19.03	0.152	23.8	1.64	2.17
13.6	19.14	0.183	22.7	1.61	2.14
15.0	19.28	0.203	22.5	1.59	2.13
16.5	19.42	0.214	24.0	1.56	2.09
18.2	19.57	0.225	25.0	1.54	2.08
20.0	19.72	0.232	25.4	1.54	2.07
22.0	19.88	0.234	25.3	1.54	2.05
24.2	20.05	0.231	25.0	1.54	2.04
26.6	20.23	0.227	25.5	1.52	2.03
29.2	20.41	0.226	25.1	1.52	2.02
32.2	20.57	0.231	26.7	1.52	2.01
35.4	20.75	0.233	26.3	1.52	2.00
38.9	20.93	0.232	26.8	1.51	2.02
42.8	21.11	0.235	27.2	1.52	1.98
47.1	21.30	0.232	28.0	1.51	1.98
51.8	21.51	0.227	28.3	1.48	2.04
57.0	21.69	0.226	28.7	1.49	1.99
62.7	21.89	0.228	29.2	1.48	2.01
69.0	22.09	0.228	28.4	1.46	1.94
75.8	22.29	0.227	28.5	1.47	2.03
83.4	22.51	0.222	31.0	1.45	1.89
91.8	22.70	0.224	33.4	1.49	– –
101.0	22.93	0.230	33.1	1.45	– –
111.1	23.14	0.234	35.8	1.46	– –
122.2	23.31	0.267	36.3	– –	– –
134.4	23.60	0.267	36.3	– –	– –

Table 2.9: Galaxy parameters, cont.

NGC 3801					
Radius (1)	μ_R (2)	ϵ (3)	ϕ (4)	$B-R$ (5)	$U-R$ (6)
3.2	18.68	– –	– –	– –	– –
3.9	18.83	– –	– –	– –	– –
4.7	19.05	0.408	118.8	– –	– –
5.5	19.23	0.364	119.7	1.75	– –
6.0	19.37	0.334	119.7	1.73	– –
6.6	19.50	0.313	119.9	1.74	– –
7.3	19.63	0.289	120.6	1.73	2.34
8.0	19.77	0.262	121.6	1.71	2.28
8.8	19.89	0.241	123.1	1.68	2.24
9.7	20.00	0.244	123.7	1.68	2.22
10.7	20.12	0.240	123.0	1.67	2.30
11.7	20.27	0.233	119.2	1.61	2.19
12.9	20.38	0.246	119.0	1.59	2.10
14.2	20.43	0.265	120.6	1.60	2.14
15.6	20.61	0.274	120.3	1.59	2.10
17.2	20.74	0.292	121.7	1.60	2.08
18.9	20.87	0.307	119.7	1.57	2.04
20.8	20.96	0.337	120.7	1.61	2.10
22.8	21.13	0.360	121.3	1.56	2.01
25.1	21.24	0.387	122.2	1.53	1.93
27.6	21.34	0.415	123.5	1.52	2.00
30.4	21.51	0.432	123.2	1.46	1.85
33.4	21.69	0.442	123.6	1.44	1.79
36.8	21.88	0.460	122.4	1.43	1.78
40.5	22.08	0.482	122.0	1.39	1.72
44.6	22.32	0.483	121.4	1.36	1.62
49.0	22.60	0.466	120.4	1.30	1.62
53.9	22.74	0.493	119.4	1.37	1.69
59.3	22.93	0.494	119.4	1.35	1.61
65.2	23.22	0.448	119.5	1.25	– –
71.8	23.42	0.435	121.1	– –	– –

Table 2.9: Galaxy parameters, cont.

NGC 4261					
Radius (1)	μ_R (2)	ϵ (3)	ϕ (4)	$B-R$ (5)	$U-R$ (6)
3.9	17.13	– –	– –	1.66	– –
4.7	17.37	0.235	158.8	1.65	2.28
5.4	17.56	0.238	158.6	1.64	2.27
6.0	17.69	0.239	158.4	1.64	2.28
6.6	17.83	0.242	158.7	1.64	2.28
7.2	17.98	0.241	158.3	1.64	2.27
7.9	18.12	0.242	158.5	1.63	2.26
8.7	18.26	0.246	158.7	1.64	2.25
9.6	18.40	0.249	158.2	1.63	2.24
10.6	18.54	0.251	158.3	1.63	2.23
11.6	18.68	0.251	158.4	1.63	2.24
12.8	18.81	0.248	158.1	1.62	2.22
14.1	18.96	0.240	158.1	1.62	2.20
15.5	19.11	0.232	158.3	1.62	2.19
17.0	19.27	0.223	158.1	1.62	2.18
18.7	19.45	0.208	158.7	1.61	2.18
20.6	19.62	0.202	158.3	1.61	2.21
22.7	19.82	0.191	158.6	1.61	2.18
25.0	20.00	0.183	159.0	1.61	2.17
27.4	20.20	0.179	158.8	1.59	2.13
30.2	20.39	0.176	158.7	1.58	2.08
33.2	20.59	0.167	159.2	1.57	2.08
36.5	20.77	0.164	158.6	1.58	2.12
40.2	20.95	0.165	159.4	1.56	2.08
44.2	21.09	0.174	160.7	1.59	2.08
48.6	21.30	0.161	159.3	1.53	2.03
53.5	21.44	0.156	158.8	1.55	2.01
58.8	21.61	0.154	158.6	1.56	1.98
64.7	21.78	0.149	161.0	1.54	1.94
71.1	21.95	0.147	159.9	1.54	– –
78.2	22.15	0.146	163.2	1.51	– –
86.0	22.36	0.136	164.7	– –	– –
94.6	22.56	0.143	163.7	– –	– –
104.1	22.81	0.140	161.9	– –	– –
114.5	23.01	0.150	162.9	– –	– –
125.9	23.22	0.163	161.7	– –	– –

Table 2.9: Galaxy parameters, cont.

NGC 4278					
Radius (1)	μ_R (2)	ϵ (3)	ϕ (4)	$B-R$ (5)	$U-R$ (6)
3.7	16.83	0.129	18.3	1.65	– –
4.4	17.07	0.135	17.8	1.65	– –
5.1	17.25	0.137	17.8	1.65	2.20
5.6	17.37	0.140	17.3	1.65	2.20
6.2	17.49	0.143	16.6	1.65	2.20
6.8	17.62	0.146	16.2	1.64	2.18
7.5	17.75	0.150	15.2	1.63	2.16
8.2	17.89	0.155	15.1	1.63	2.13
9.1	18.03	0.153	15.3	1.61	2.10
10.0	18.18	0.150	15.5	1.61	2.06
11.0	18.35	0.144	16.4	1.60	2.06
12.1	18.53	0.137	16.6	1.59	2.07
13.3	18.72	0.133	17.0	1.58	2.05
14.6	18.90	0.130	16.6	1.57	2.04
16.1	19.10	0.130	17.4	1.57	2.01
17.7	19.26	0.130	17.9	1.58	1.99
19.4	19.47	0.120	17.0	1.56	1.98
21.4	19.68	0.106	16.9	1.55	1.98
23.5	19.89	0.098	19.1	1.55	1.95
25.9	20.09	0.089	20.1	1.55	1.92
28.5	20.27	0.092	24.3	1.54	1.92
31.3	20.44	0.106	25.4	1.54	1.91
34.5	20.64	0.080	27.5	1.53	1.89
37.9	20.78	0.097	30.1	1.55	1.89
41.7	20.96	0.097	32.2	1.52	1.85
45.9	21.15	0.090	31.6	1.51	1.85
50.4	21.35	0.090	33.5	1.50	1.81
55.5	21.56	0.088	36.1	1.50	1.80
61.0	21.78	0.088	35.3	1.48	1.79
67.1	22.01	0.086	37.1	1.46	1.75
73.9	22.21	0.097	35.1	1.47	1.79
81.2	22.43	0.105	34.7	1.46	1.70
89.4	22.64	0.110	36.7	1.46	1.70
98.3	22.83	0.120	37.7	1.47	– –
108.1	23.05	0.115	37.7	1.47	– –
118.9	23.25	0.125	42.7	– –	– –

Table 2.9: Galaxy parameters, cont.

NGC 4374					
Radius	μ_R	ϵ	ϕ	$B-R$	$U-R$
(1)	(2)	(3)	(4)	(5)	(6)
2.7	16.04	0.183	137.5	– –	– –
3.2	16.20	0.195	137.4	– –	– –
3.9	16.40	0.191	135.2	1.65	– –
4.7	16.63	0.188	132.3	1.64	– –
5.5	16.80	0.194	129.3	1.63	– –
6.0	16.93	0.194	129.1	1.63	– –
6.6	17.06	0.194	128.5	1.63	2.29
7.3	17.20	0.193	128.1	1.63	2.28
8.0	17.33	0.192	127.5	1.63	2.27
8.8	17.47	0.189	126.9	1.62	2.26
9.7	17.62	0.182	125.9	1.62	2.24
10.4	17.73	0.170	126.5	1.63	2.23
11.4	17.89	0.166	126.2	1.62	2.23
12.6	18.05	0.159	125.9	1.62	2.22
13.9	18.21	0.155	125.9	1.62	2.21
15.2	18.38	0.153	125.8	1.61	2.19
16.8	18.54	0.150	126.1	1.61	2.19
18.4	18.69	0.147	125.9	1.61	2.20
20.3	18.85	0.147	126.0	1.61	2.19
22.3	19.00	0.145	126.0	1.61	2.17
24.5	19.15	0.141	125.2	1.61	2.18
27.0	19.31	0.134	125.2	1.60	2.16
29.7	19.48	0.125	124.9	1.60	2.15
32.7	19.64	0.118	125.0	1.60	2.13
35.9	19.81	0.113	124.1	1.60	2.14
39.5	19.98	0.110	124.9	1.59	2.12
43.5	20.15	0.106	124.4	1.60	2.12
47.8	20.33	0.102	124.2	1.59	2.09
52.6	20.52	0.096	123.6	1.59	2.10
57.8	20.71	0.085	122.9	1.57	2.06
63.6	20.92	0.076	122.8	1.57	2.05
69.0	21.07	0.068	125.3	1.57	2.06
75.9	21.26	0.054	129.0	1.56	2.06
83.5	21.46	0.055	136.4	1.55	2.02
91.8	21.66	0.052	134.6	1.55	1.99
101.0	21.87	0.043	136.6	1.56	1.96
111.1	22.09	0.041	137.6	1.55	1.98
122.2	22.28	0.050	131.7	1.56	– –
135.0	22.50	0.051	137.1	1.54	– –
148.5	22.70	0.064	133.9	1.57	– –
163.3	22.93	0.071	135.9	1.58	– –

Table 2.9: Galaxy parameters, cont.

NGC 4387					
Radius	μ_R	ϵ	ϕ	$B-R$	$U-R$
(1)	(2)	(3)	(4)	(5)	(6)
2.7	17.66	– –	– –	– –	2.17
3.2	17.83	– –	– –	1.65	2.15
4.0	18.04	– –	– –	1.64	2.13
4.7	18.22	0.261	141.2	1.64	2.13
5.4	18.38	0.280	141.3	1.64	2.13
5.9	18.49	0.296	141.2	1.64	2.12
6.5	18.62	0.309	141.0	1.64	2.12
7.2	18.75	0.320	141.0	1.64	2.12
7.9	18.89	0.328	141.3	1.64	2.12
8.7	19.04	0.338	140.9	1.63	2.12
9.6	19.19	0.346	140.8	1.63	2.12
10.5	19.35	0.359	140.9	1.63	2.11
11.6	19.51	0.373	140.7	1.63	2.14
12.7	19.68	0.384	140.7	1.64	2.13
14.0	19.85	0.393	140.6	1.63	2.13
15.4	20.05	0.397	140.7	1.62	2.10
17.0	20.23	0.407	140.5	1.63	2.13
18.7	20.44	0.412	140.6	1.62	2.14
20.5	20.65	0.413	140.9	1.62	2.12
22.6	20.89	0.411	141.4	1.62	2.14
24.8	21.15	0.408	142.2	1.61	2.09
27.3	21.41	0.405	142.7	1.61	2.10
30.0	21.70	0.394	142.9	1.63	2.11
33.0	21.99	0.385	143.3	1.59	– –
36.3	22.28	0.376	143.5	1.58	– –
40.0	22.57	0.361	143.5	1.60	– –
44.0	22.86	0.350	143.1	1.61	– –
48.4	23.14	0.344	142.9	– –	– –
53.2	23.41	0.341	142.2	– –	– –

Table 2.9: Galaxy parameters, cont.

NGC 4406					
Radius	μ_R	ϵ	ϕ	$B-R$	$U-R$
(1)	(2)	(3)	(4)	(5)	(6)
3.1	16.63	0.120	129.3	– –	– –
3.7	16.85	0.122	129.3	1.59	– –
4.5	17.07	0.133	125.4	1.59	– –
5.1	17.23	0.139	123.8	1.59	– –
5.7	17.34	0.143	123.3	1.59	– –
6.2	17.46	0.148	122.2	1.59	– –
6.8	17.57	0.155	121.5	1.59	2.23
7.5	17.68	0.160	120.6	1.58	2.22
8.3	17.79	0.164	120.3	1.59	2.22
9.1	17.91	0.169	120.0	1.59	2.21
10.0	18.02	0.175	119.6	1.59	2.20
11.0	18.14	0.177	119.8	1.58	2.20
12.1	18.26	0.180	119.5	1.58	2.19
13.3	18.39	0.182	119.0	1.57	2.18
14.7	18.52	0.184	119.5	1.57	2.17
16.1	18.64	0.194	120.0	1.57	2.18
17.7	18.77	0.195	120.5	1.57	2.16
19.5	18.90	0.199	120.3	1.57	2.17
21.5	19.04	0.202	120.5	1.56	2.17
23.6	19.16	0.209	121.6	1.57	2.14
26.0	19.29	0.217	121.2	1.57	2.14
28.6	19.41	0.226	122.0	1.57	2.14
31.4	19.53	0.234	122.4	1.56	2.14
34.6	19.65	0.238	123.1	1.56	2.11
38.0	19.79	0.239	123.2	1.56	2.09
41.8	19.92	0.244	123.3	1.56	2.10
46.0	20.06	0.245	123.0	1.56	2.09
50.6	20.22	0.242	123.3	1.55	2.07
55.7	20.37	0.247	124.6	1.56	2.06
61.3	20.52	0.253	125.3	1.55	2.05
67.4	20.69	0.253	125.3	1.54	2.05
74.1	20.86	0.249	124.8	1.53	2.03
81.5	21.00	0.253	123.4	1.55	2.03
89.6	21.15	0.261	121.7	1.55	2.05
98.6	21.32	0.267	120.0	1.56	2.06
108.5	21.50	0.264	119.0	1.57	2.06
119.3	21.70	0.259	118.3	1.57	– –
131.2	21.87	0.275	117.5	1.58	– –
144.4	22.03	0.295	117.9	1.59	– –
158.8	22.16	0.329	118.1	1.60	– –
174.7	22.30	0.356	119.0	– –	– –

Table 2.9: Galaxy parameters, cont.

NGC 4472					
Radius	μ_R	ϵ	ϕ	$B-R$	$U-R$
(1)	(2)	(3)	(4)	(5)	(6)
3.2	16.22	0.067	164.5	– –	– –
3.9	16.37	0.067	163.1	– –	– –
4.7	16.54	0.069	163.9	1.68	– –
5.4	16.68	0.076	164.9	1.67	– –
5.9	16.78	0.080	164.1	1.67	– –
6.5	16.88	0.087	164.0	1.67	– –
7.2	16.98	0.096	164.0	1.67	2.32
7.9	17.09	0.103	163.6	1.67	2.31
8.7	17.20	0.112	162.7	1.66	2.31
9.6	17.31	0.118	162.4	1.66	2.30
10.5	17.43	0.124	162.3	1.66	2.29
11.6	17.54	0.135	162.1	1.66	2.29
12.7	17.66	0.147	162.2	1.66	2.29
14.0	17.78	0.153	162.8	1.66	2.29
15.4	17.90	0.163	162.3	1.66	2.28
17.0	18.01	0.173	162.3	1.66	2.28
18.7	18.14	0.179	162.1	1.66	2.28
20.5	18.26	0.179	162.2	1.66	2.27
22.6	18.40	0.180	162.0	1.66	2.27
24.8	18.54	0.180	161.9	1.66	2.27
27.3	18.68	0.181	161.6	1.66	2.27
30.0	18.84	0.178	161.4	1.66	2.24
33.0	19.00	0.175	161.5	1.65	2.25
36.3	19.17	0.166	161.1	1.65	2.23
39.9	19.33	0.167	160.8	1.65	2.22
44.0	19.50	0.168	160.3	1.64	2.22
48.4	19.66	0.167	160.4	1.64	2.19
53.2	19.81	0.170	160.2	1.64	2.18
58.5	19.97	0.172	159.5	1.63	2.17
64.4	20.11	0.179	159.5	1.63	2.16
70.8	20.26	0.177	159.0	1.63	2.15
77.9	20.41	0.176	158.9	1.63	2.15
85.7	20.58	0.175	158.8	1.63	2.14
94.2	20.75	0.170	158.3	1.63	2.12
103.6	20.93	0.169	158.1	1.63	2.13
116.7	21.23	0.164	156.7	1.60	2.06
128.3	21.46	0.160	155.6	1.59	2.05
141.2	21.69	0.165	155.1	1.59	2.06
155.3	21.90	0.178	153.5	1.60	2.07
170.8	22.14	0.176	150.7	– –	– –

Table 2.9: Galaxy parameters, cont.

NGC 4478					
Radius	μ_R	ϵ	ϕ	$B-R$	$U-R$
(1)	(2)	(3)	(4)	(5)	(6)
3.2	17.39	0.144	152.6	– –	– –
4.0	17.72	0.148	150.6	1.54	2.09
4.6	17.89	0.155	150.3	1.54	2.08
5.4	18.04	0.163	148.8	1.55	2.08
5.9	18.15	0.170	147.7	1.55	2.09
6.5	18.27	0.175	147.0	1.55	2.09
7.1	18.39	0.182	146.6	1.55	2.08
7.8	18.52	0.189	146.1	1.55	2.08
8.6	18.66	0.193	145.3	1.55	2.08
9.5	18.81	0.195	145.2	1.55	2.07
10.4	18.97	0.194	144.7	1.55	2.05
11.5	19.15	0.192	143.7	1.54	2.07
12.6	19.33	0.190	143.6	1.54	2.06
13.9	19.52	0.184	143.3	1.54	2.05
15.3	19.73	0.181	142.9	1.54	2.06
16.8	19.96	0.177	142.0	1.54	2.03
18.5	20.21	0.171	141.1	1.53	2.01
20.3	20.45	0.169	140.4	1.52	2.02
22.4	20.71	0.162	138.9	1.53	2.01
24.6	20.98	0.163	137.9	1.52	2.00
27.0	21.25	0.160	136.4	1.52	2.01
29.7	21.55	0.159	136.1	1.49	1.94
32.7	21.81	0.167	135.9	1.52	1.94
36.0	22.12	0.176	136.9	1.51	1.99
39.6	22.42	0.178	138.5	1.51	1.96
43.5	22.76	0.177	140.2	1.49	– –
47.9	23.11	0.164	143.5	1.48	– –
52.7	23.45	0.143	148.5	1.47	– –
58.0	23.82	0.121	155.3	– –	– –

Table 2.9: Galaxy parameters, cont.

NGC 4486					
Radius	μ_R	ϵ	ϕ	$B-R$	$U-R$
(1)	(2)	(3)	(4)	(5)	(6)
4.6	17.01	0.022	137.6	1.68	2.27
5.3	17.08	0.020	137.3	1.68	2.28
5.8	17.14	0.016	151.4	1.68	2.29
6.4	17.21	0.023	168.8	1.68	2.29
7.0	17.28	0.029	175.6	1.68	2.29
7.7	17.36	0.029	1.7	1.68	2.29
8.5	17.44	0.033	178.4	1.68	2.28
9.3	17.55	0.019	174.9	1.67	2.26
10.2	17.65	0.031	174.9	1.67	2.25
11.3	17.76	0.031	177.9	1.67	2.27
12.4	17.87	0.029	173.6	1.67	2.25
13.6	17.99	0.036	176.7	1.67	2.24
15.0	18.12	0.033	169.2	1.66	2.24
16.5	18.25	0.038	172.8	1.66	2.23
18.2	18.38	0.044	171.2	1.66	2.22
20.0	18.52	0.044	168.5	1.66	2.21
22.0	18.67	0.045	166.4	1.65	2.19
24.2	18.81	0.051	164.3	1.65	2.18
26.6	18.96	0.053	163.2	1.64	2.16
29.2	19.12	0.053	161.8	1.64	2.13
32.2	19.27	0.055	160.6	1.64	2.12
35.4	19.42	0.062	159.6	1.63	2.12
38.9	19.57	0.071	159.8	1.64	2.10
42.8	19.72	0.080	158.1	1.63	2.05
47.1	19.89	0.074	157.5	1.62	2.01
51.8	20.05	0.082	157.5	1.62	2.04
57.0	20.21	0.083	156.4	1.62	2.04
62.7	20.36	0.087	156.2	1.62	2.03
69.0	20.52	0.100	155.9	1.61	2.01
75.8	20.69	0.097	157.1	1.61	1.98
83.4	20.86	0.105	155.5	1.61	1.96
91.8	21.04	0.105	154.8	1.61	1.95
101.0	21.23	0.110	155.8	1.61	1.95
111.1	21.43	0.118	156.2	1.60	1.93
122.2	21.64	0.131	154.2	1.60	1.91
134.4	21.87	0.135	153.4	1.59	1.85
147.8	22.05	0.148	150.7	1.59	– –
162.6	22.28	0.148	150.7	– –	– –

Table 2.9: Galaxy parameters, cont.

NGC 4551					
Radius (1)[a]	μ_R (2)	ϵ (3)	ϕ (4)	$B-R$ (5)	$U-R$ (6)
2.7	17.78	– –	– –	1.56	– –
3.2	17.99	0.219	67.5	1.55	– –
3.9	18.18	0.208	67.8	1.55	2.14
4.6	18.38	0.218	68.2	1.55	2.15
5.3	18.54	0.227	68.3	1.55	2.13
5.8	18.66	0.232	68.4	1.54	2.11
6.4	18.78	0.238	68.4	1.54	2.12
7.1	18.90	0.243	68.5	1.54	2.12
7.8	19.03	0.247	68.7	1.54	2.11
8.5	19.17	0.249	68.8	1.54	2.12
9.4	19.31	0.254	68.7	1.54	2.13
10.3	19.45	0.258	69.0	1.55	2.12
11.4	19.60	0.261	69.1	1.55	2.13
12.5	19.76	0.268	69.1	1.55	2.12
13.8	19.93	0.272	68.8	1.55	2.10
15.1	20.11	0.277	69.5	1.55	2.10
16.6	20.29	0.283	68.6	1.54	2.12
18.3	20.48	0.289	68.7	1.55	2.13
20.1	20.68	0.292	68.8	1.56	2.12
22.1	20.90	0.291	68.3	1.55	2.16
24.4	21.11	0.297	69.0	1.55	2.12
26.8	21.36	0.296	69.0	1.54	2.06
29.5	21.61	0.295	69.1	1.55	2.09
32.4	21.89	0.284	69.3	1.55	2.10
35.6	22.21	0.265	69.4	1.54	2.11
39.2	22.53	0.248	70.1	1.53	2.13
43.5	22.90	0.239	70.2	1.55	– –
47.8	23.28	0.229	70.8	– –	– –

Table 2.9: Galaxy parameters, cont.

NGC 4636					
Radius (1)	μ_R (2)	ϵ (3)	ϕ (4)	$B-R$ (5)	$U-R$ (6)
3.8	17.24	0.021	157.5	– –	– –
4.6	17.41	0.023	167.9	1.64	– –
5.3	17.55	0.023	166.4	1.63	– –
5.9	17.65	0.022	168.1	1.63	– –
6.4	17.76	0.023	163.9	1.62	– –
7.1	17.87	0.025	165.5	1.62	2.27
7.8	17.99	0.029	162.7	1.62	2.26
8.6	18.11	0.036	161.0	1.61	2.26
9.4	18.24	0.035	162.0	1.60	2.25
10.4	18.36	0.039	160.0	1.60	2.25
11.4	18.50	0.043	160.1	1.59	2.22
12.6	18.63	0.047	160.0	1.59	2.20
13.8	18.76	0.061	161.6	1.59	2.19
15.2	18.90	0.066	158.2	1.59	2.18
16.7	19.04	0.076	157.3	1.58	2.16
18.4	19.16	0.082	157.2	1.58	2.17
20.2	19.30	0.091	155.2	1.57	2.13
22.3	19.42	0.101	155.1	1.57	2.15
24.5	19.54	0.112	155.0	1.57	2.12
26.9	19.66	0.122	151.4	1.57	2.11
29.6	19.81	0.123	150.8	1.55	2.10
32.6	19.96	0.127	150.6	1.56	2.10
35.9	20.11	0.132	148.2	1.55	2.06
39.4	20.24	0.149	146.5	1.56	2.08
43.4	20.40	0.165	147.7	1.54	2.03
47.7	20.53	0.181	146.6	1.53	2.01
52.5	20.64	0.202	146.3	1.54	2.02
57.7	20.76	0.222	147.2	1.55	2.00
63.5	20.89	0.226	146.6	1.53	1.97
69.9	21.02	0.235	146.7	1.54	1.95
76.9	21.15	0.238	147.3	1.54	1.98
84.5	21.31	0.239	147.3	1.52	1.97
93.0	21.44	0.255	147.1	1.53	1.97
102.6	21.61	0.256	147.6	1.52	1.93
112.9	21.78	0.260	146.1	1.52	– –
124.2	21.96	0.263	147.4	1.51	– –
136.6	22.17	0.262	145.8	1.52	– –
150.2	22.38	0.269	145.7	1.53	– –
165.3	22.57	0.290	144.0	– –	– –

Table 2.9: Galaxy parameters, cont.

NGC 4649					
Radius	μ_R	ϵ	ϕ	$B-R$	$U-R$
(1)	(2)	(3)	(4)	(5)	(6)
3.2	16.28	0.053	94.8	--	--
3.9	16.41	0.066	97.5	--	--
4.7	16.57	0.082	96.4	--	--
5.4	16.70	0.089	97.9	1.67	--
6.0	16.80	0.097	99.7	1.66	--
6.6	16.91	0.105	100.0	1.66	--
7.2	17.02	0.114	100.3	1.66	2.41
8.0	17.13	0.122	100.2	1.66	2.41
8.7	17.24	0.130	100.4	1.66	2.40
9.6	17.36	0.136	100.8	1.66	2.40
10.6	17.48	0.141	101.1	1.65	2.39
11.6	17.61	0.147	101.8	1.65	2.39
12.8	17.74	0.151	101.9	1.65	2.38
14.1	17.87	0.148	102.5	1.65	2.37
15.5	18.01	0.151	102.6	1.65	2.37
17.0	18.16	0.151	102.6	1.65	2.34
18.7	18.32	0.149	101.9	1.64	2.33
20.6	18.48	0.151	102.4	1.65	2.34
22.7	18.64	0.153	102.8	1.64	2.32
25.0	18.80	0.154	103.2	1.64	2.31
27.5	18.97	0.156	103.8	1.63	2.30
30.2	19.12	0.165	103.8	1.63	2.29
33.2	19.27	0.175	104.5	1.64	2.29
36.5	19.41	0.187	103.7	1.63	2.28
40.2	19.54	0.202	104.1	1.62	2.27
44.2	19.67	0.209	103.5	1.62	2.26
48.6	19.81	0.216	103.9	1.62	2.26
53.5	19.96	0.217	103.2	1.61	2.26
58.8	20.11	0.217	103.9	1.62	2.26
64.7	20.28	0.215	104.2	1.60	2.23
71.1	20.47	0.212	104.5	1.60	2.22
78.3	20.69	0.195	104.5	1.59	2.21
86.1	20.90	0.196	105.2	1.60	2.20
94.7	21.10	0.203	105.2	1.59	2.19
104.2	21.30	0.212	105.2	1.60	2.22
114.6	21.51	0.216	105.8	1.59	--
126.0	21.76	0.211	106.9	1.56	--
138.7	22.02	0.213	107.4	1.58	--
152.5	22.30	0.215	105.9	1.63	--
167.8	22.55	0.233	107.2	--	--
184.5	22.79	0.235	107.4	--	--

Table 2.9: Galaxy parameters, cont.

NGC 4697					
Radius	μ_R	ϵ	ϕ	$B-R$	$U-R$
(1)	(2)	(3)	(4)	(5)	(6)
2.6	16.29	--	--	--	--
3.2	16.44	--	--	--	--
3.8	16.60	0.323	64.9	--	--
4.8	16.79	0.354	66.2	--	--
5.4	16.92	0.363	66.8	--	--
5.9	17.02	0.371	66.6	1.60	2.19
6.5	17.13	0.376	66.7	1.60	2.18
7.2	17.24	0.381	66.7	1.60	2.18
7.9	17.36	0.386	66.9	1.59	2.16
8.7	17.48	0.388	66.9	1.59	2.15
9.6	17.60	0.392	66.8	1.59	2.16
10.5	17.72	0.393	66.7	1.59	2.14
11.6	17.85	0.390	66.7	1.58	2.13
12.7	17.97	0.388	66.8	1.57	2.12
14.0	18.11	0.387	66.8	1.57	2.10
15.4	18.24	0.387	67.0	1.57	2.09
16.9	18.36	0.394	67.6	1.57	2.09
18.6	18.49	0.397	67.4	1.56	2.08
20.5	18.63	0.402	66.8	1.56	2.08
22.5	18.75	0.415	66.8	1.56	2.06
24.8	18.87	0.426	66.8	1.55	2.05
27.2	18.99	0.435	66.9	1.55	2.04
30.0	19.12	0.447	66.7	1.55	2.03
33.0	19.26	0.452	66.8	1.54	2.03
36.3	19.40	0.455	66.9	1.54	2.03
39.9	19.55	0.451	67.2	1.54	2.01
43.9	19.71	0.447	67.2	1.54	2.00
48.2	19.89	0.438	67.0	1.53	1.99
53.1	20.08	0.420	67.5	1.52	1.98
58.4	20.29	0.402	67.7	1.52	1.96
64.2	20.51	0.385	67.8	1.52	1.95
70.6	20.75	0.366	67.1	1.50	1.92
77.7	20.97	0.353	67.2	1.49	1.91
85.4	20.19	0.342	67.4	1.49	1.90
94.0	21.44	0.319	67.2	1.46	1.85
104.5	21.72	0.306	67.2	1.44	1.85
115.0	21.96	0.301	67.6	1.42	1.85
126.5	22.18	0.300	69.1	1.43	--
139.2	22.38	0.308	69.2	1.41	--
153.1	22.60	0.308	68.8	1.39	--
168.5	22.84	0.317	68.4	--	--
187.6	23.08	0.307	66.7	--	--

Table 2.9: Galaxy parameters, cont.

NGC 4874					
Radius	μ_R	ϵ	ϕ	$B-R$	$U-R$
(1)'	(2)	(3)	(4)	(5)	(6)
3.8	18.78	0.094	23.1	1.64	2.31
4.6	19.00	0.088	23.2	1.62	2.23
5.3	19.18	0.076	21.6	1.62	2.22
5.8	19.31	0.081	26.5	1.62	2.19
6.4	19.43	0.086	29.3	1.63	2.26
7.0	19.59	0.075	28.3	1.61	2.17
7.7	19.72	0.070	30.0	1.61	2.17
8.5	19.87	0.065	29.2	1.61	2.25
9.3	20.03	0.052	35.0	1.59	2.20
10.2	20.20	0.049	38.4	1.58	2.13
11.3	20.33	0.040	42.2	1.58	2.14
12.4	20.47	0.044	45.4	1.59	2.22
13.6	20.64	0.032	30.3	1.55	2.16
15.0	20.75	0.036	30.4	1.56	2.12
16.5	20.85	0.056	28.6	1.58	2.18
18.2	20.96	0.063	34.3	1.56	2.15
20.0	21.07	0.080	27.4	1.55	2.10
22.0	21.17	0.061	32.7	1.51	2.10
24.2	21.27	0.083	39.9	1.53	2.10
26.6	21.40	0.087	36.4	1.50	2.01
29.2	21.38	0.106	36.2	1.52	2.02
32.2	21.48	0.142	34.5	1.52	2.03
35.4	21.71	0.145	35.3	1.50	2.03
38.9	21.83	0.155	32.0	1.47	– –
42.8	22.01	0.128	28.1	1.46	– –
47.1	22.15	0.138	29.2	1.43	– –
51.8	22.30	0.148	28.2	1.40	– –
57.0	22.45	0.099	34.9	– –	– –
62.7	22.66	0.063	55.4	– –	– –
69.0	22.84	0.045	57.0	– –	– –
75.8	22.91	0.048	54.7	– –	– –
83.4	23.06	0.075	53.9	– –	– –
91.8	23.29	0.142	64.9	– –	– –

Table 2.9: Galaxy parameters, cont.

NGC 4889					
Radius	μ_R	ϵ	ϕ	$B-R$	$U-R$
(1)	(2)	(3)	(4)	(5)	(6)
3.8	18.10	– –	– –	1.56	2.33
4.6	18.33	– –	– –	1.55	2.33
5.3	18.50	– –	– –	1.56	2.34
5.8	18.64	0.237	77.3	1.56	2.35
6.4	18.77	0.246	77.4	1.56	2.31
7.0	18.92	0.254	77.3	1.55	2.28
7.7	19.07	0.266	77.6	1.53	2.27
8.5	19.21	0.273	77.4	1.53	2.24
9.3	19.36	0.276	77.8	1.52	2.23
10.2	19.50	0.286	78.1	1.53	2.19
11.3	19.66	0.299	77.8	1.52	2.15
12.4	19.81	0.300	78.0	1.51	2.10
13.6	19.96	0.309	77.9	1.51	2.20
15.0	20.10	0.313	78.3	1.50	2.26
16.5	20.26	0.325	78.5	1.50	2.18
18.2	20.39	0.325	78.5	1.49	2.21
20.0	20.51	0.346	78.3	1.53	2.13
22.0	20.69	0.348	77.7	1.51	2.01
24.2	20.87	0.342	78.3	1.48	2.17
26.6	21.03	0.344	78.5	1.48	2.10
29.2	21.19	0.345	78.7	1.46	2.21
32.2	21.34	0.340	78.4	1.48	2.30
35.4	21.51	0.339	79.7	1.48	2.28
38.9	21.68	0.341	79.7	1.48	2.18
42.8	21.86	0.334	81.4	1.41	2.14
47.1	22.06	0.350	78.5	1.38	2.09
51.8	22.26	0.362	75.1	1.37	2.05
57.0	22.43	0.374	77.5	1.37	– –
62.7	22.59	0.375	79.2	1.36	– –
69.0	22.82	0.352	80.5	1.30	– –
75.8	22.99	0.366	79.1	1.31	– –
83.4	23.20	0.363	80.5	– –	– –

Table 2.9: Galaxy parameters, cont.

NGC 5638					
Radius	μ_R	ϵ	ϕ	$B-R$	$U-R$
(1)	(2)	(3)	(4)	(5)	(6)
3.2	17.66	0.048	139.3	– –	– –
3.9	17.89	0.048	139.9	1.61	– –
4.7	18.14	0.048	138.7	1.60	1.96
5.5	18.34	0.050	138.9	1.60	1.94
6.0	18.48	0.050	139.8	1.60	1.93
6.6	18.62	0.050	140.1	1.60	1.90
7.3	18.76	0.054	141.0	1.59	1.90
8.0	18.91	0.056	140.7	1.59	1.89
8.8	19.07	0.056	140.8	1.59	1.89
9.7	19.22	0.060	142.4	1.58	1.86
10.7	19.37	0.064	142.9	1.58	1.85
11.7	19.51	0.071	141.6	1.58	1.87
12.9	19.65	0.080	142.3	1.58	1.84
14.2	19.79	0.085	141.5	1.57	1.77
15.6	19.94	0.092	141.5	1.57	1.80
17.2	20.09	0.099	142.3	1.57	1.84
18.9	20.25	0.104	140.8	1.57	– –
20.8	20.43	0.106	141.8	1.57	– –
22.9	20.61	0.107	143.3	1.56	– –
25.2	20.81	0.105	143.9	1.55	– –
27.7	21.02	0.107	144.8	1.54	– –
30.5	21.22	0.112	146.0	1.52	– –
33.5	21.42	0.113	147.3	1.52	– –
36.9	21.63	0.118	149.1	1.51	– –
40.6	21.86	0.118	149.4	1.50	– –
44.6	22.11	0.119	148.6	1.49	– –
49.1	22.38	0.115	152.7	1.47	– –
54.0	22.65	0.121	159.4	– –	– –
59.4	22.96	0.112	160.7	– –	– –
65.3	23.24	0.128	163.5	– –	– –
71.8	23.66	0.126	160.6	– –	– –

Table 2.9: Galaxy parameters, cont.

NGC 5813					
Radius	μ_R	ϵ	ϕ	$B-R$	$U-R$
(1)	(2)	(3)	(4)	(5)	(6)
3.2	17.40	0.077	149.2	1.66	2.37
3.8	17.65	0.084	149.2	1.64	2.34
4.6	17.94	0.087	149.8	1.62	2.31
5.4	18.16	0.087	148.4	1.63	2.28
5.9	18.31	0.087	146.6	1.63	2.27
6.5	18.46	0.085	145.3	1.64	2.28
7.2	18.61	0.085	145.1	1.62	2.27
7.9	18.76	0.084	143.0	1.60	2.27
8.7	18.90	0.087	142.6	1.62	2.26
9.5	19.04	0.090	142.0	1.61	2.24
10.5	19.17	0.094	141.1	1.61	2.23
11.5	19.30	0.102	139.7	1.60	2.23
12.7	19.43	0.108	139.3	1.61	2.22
13.9	19.55	0.120	138.4	1.61	2.23
15.3	19.67	0.127	138.6	1.61	2.22
16.9	19.80	0.136	138.1	1.60	2.21
18.6	19.93	0.144	138.2	1.60	2.22
20.4	20.06	0.155	136.6	1.60	2.22
22.5	20.18	0.168	136.0	1.60	2.22
24.7	20.31	0.186	136.4	1.60	2.24
27.2	20.43	0.195	136.2	1.59	2.20
29.9	20.55	0.217	135.6	1.59	2.21
32.9	20.66	0.231	134.9	1.59	2.22
36.2	20.79	0.240	134.3	1.59	2.21
39.8	20.92	0.250	133.6	1.59	2.20
43.7	21.06	0.251	133.7	1.57	2.20
48.1	21.22	0.251	133.7	1.57	2.16
52.9	21.38	0.255	133.2	1.58	2.18
58.2	21.55	0.257	133.5	1.57	2.19
64.0	21.72	0.266	133.5	1.58	2.13
70.4	21.90	0.272	133.4	1.58	2.22
76.0	22.04	0.276	134.6	1.58	2.22
83.5	22.22	0.278	134.5	1.57	– –
91.9	22.41	0.286	134.7	1.57	– –
101.0	22.59	0.292	133.4	1.57	– –
111.2	22.78	0.296	132.5	1.57	– –
122.2	22.96	0.304	131.4	1.55	– –
134.5	23.15	0.307	130.5	– –	– –
148.1	23.28	0.329	131.0	– –	– –
163.0	23.46	0.335	128.4	– –	– –
172.6	23.53	0.358	123.8	– –	– –

Table 2.9: Galaxy parameters, cont.

NGC 5831					
Radius (1)	μ_R (2)	ϵ (3)	ϕ (4)	$B-R$ (5)	$U-R$ (6)
2.7	17.40	– –	– –	1.69	– –
3.2	17.64	0.223	114.4	1.68	2.23
3.9	17.90	0.245	114.8	1.67	2.21
4.7	18.17	0.263	114.8	1.67	2.20
5.5	18.37	0.274	114.7	1.66	2.19
6.0	18.51	0.281	114.6	1.66	2.18
6.6	18.64	0.287	114.6	1.66	2.18
7.3	18.78	0.290	114.6	1.66	2.16
8.0	18.92	0.288	115.0	1.65	2.16
8.7	19.05	0.273	115.9	1.66	2.15
9.6	19.20	0.265	116.2	1.66	2.13
10.5	19.36	0.250	116.8	1.65	2.12
11.6	19.53	0.228	117.1	1.64	2.10
12.7	19.70	0.208	118.7	1.64	2.11
14.0	19.90	0.180	120.1	1.63	2.10
15.4	20.09	0.159	122.1	1.63	2.09
17.0	20.29	0.140	124.0	1.62	2.10
18.7	20.49	0.126	127.3	1.61	2.05
20.5	20.67	0.119	129.7	1.62	2.04
22.6	20.87	0.108	133.0	1.61	2.04
24.8	21.06	0.093	135.4	1.60	2.06
27.3	21.25	0.090	136.1	1.60	2.04
30.0	21.44	0.089	135.4	1.60	2.05
33.0	21.63	0.102	135.0	1.60	2.03
36.4	21.83	0.110	135.1	1.60	2.08
40.0	22.01	0.120	136.2	1.59	2.03
44.0	22.20	0.129	138.3	1.58	2.04
48.4	22.41	0.131	138.1	1.58	2.05
52.8	22.59	0.140	140.7	1.60	– –
58.5	22.88	0.123	138.0	– –	– –
64.4	23.18	0.100	137.3	– –	– –
69.0	23.38	0.099	141.6	– –	– –

Table 2.9: Galaxy parameters, cont.

NGC 5845					
Radius (1)	μ_R (2)	ϵ (3)	ϕ (4)	$B-R$ (5)	$U-R$ (6)
2.7	16.88	– –	– –	1.66	– –
3.2	17.23	– –	– –	1.65	– –
3.9	17.61	– –	– –	1.65	2.43
4.7	18.02	0.230	142.2	1.65	2.43
5.5	18.35	0.235	142.5	1.64	2.40
6.0	18.59	0.245	142.5	1.64	2.40
6.6	18.83	0.257	142.5	1.64	2.41
7.3	19.07	0.273	142.4	1.65	2.41
8.0	19.31	0.293	142.2	1.66	2.42
8.7	19.51	0.304	143.8	1.63	2.40
9.5	19.75	0.325	143.2	1.62	2.38
10.5	19.99	0.346	142.7	1.62	2.39
11.5	20.24	0.361	141.9	1.61	2.42
12.7	20.52	0.372	141.6	1.59	2.41
13.9	20.79	0.380	141.2	1.59	2.33
15.3	21.07	0.379	140.5	1.59	2.36
16.8	21.37	0.374	140.1	1.60	2.36
18.5	21.70	0.357	139.1	1.60	2.35
20.4	22.03	0.339	138.2	1.60	2.40
22.4	22.38	0.320	137.6	1.58	– –
24.7	22.75	0.284	136.2	1.55	– –
27.1	23.11	0.276	136.9	1.55	– –
29.8	23.49	0.251	134.0	– –	– –

Table 2.9: Galaxy parameters, cont.

IC 1101					
Radius (1)	μ_R (2)	ϵ (3)	ϕ (4)	$B-R$ (5)	$U-R$ (6)
2.7	19.55	– –	– –	1.63	– –
3.2	19.70	– –	– –	1.62	– –
4.0	19.88	– –	– –	1.61	– –
4.7	20.07	– –	– –	1.61	2.37
5.5	20.22	0.232	17.8	1.60	2.39
6.0	20.34	0.244	18.2	1.60	2.36
6.6	20.46	0.257	18.8	1.60	2.34
7.2	20.54	0.275	19.2	1.61	2.34
7.9	20.66	0.290	20.2	1.60	2.39
8.7	20.78	0.305	20.2	1.60	2.34
9.6	20.90	0.318	20.5	1.59	2.35
10.6	21.03	0.333	21.0	1.58	2.36
11.6	21.15	0.345	20.9	1.58	2.39
12.8	21.26	0.364	21.1	1.58	2.37
14.1	21.39	0.377	21.9	1.57	2.34
15.5	21.50	0.393	22.2	1.56	2.28
17.0	21.63	0.406	21.2	1.56	2.29
18.7	21.74	0.426	21.8	1.56	2.30
20.6	21.85	0.445	22.1	1.55	2.32
22.6	21.98	0.448	22.8	1.54	2.28
24.9	22.15	0.441	23.6	1.55	2.25
27.4	22.31	0.443	24.2	1.55	2.29
30.1	22.47	0.458	24.2	1.53	– –
33.1	22.61	0.471	24.3	– –	– –
36.5	22.76	0.486	24.9	– –	– –
40.1	22.91	0.498	25.1	– –	– –
44.1	23.13	0.490	25.5	– –	– –
48.5	23.28	0.510	23.7	– –	– –
53.4	23.52	0.502	24.1	– –	– –
58.7	23.72	0.504	25.4	– –	– –

Table 2.9: Galaxy parameters, cont.

NGC 6051					
Radius (1)	μ_R (2)	ϵ (3)	ϕ (4)	$B-R$ (5)	$U-R$ (6)
3.2	19.00	– –	– –	1.77	– –
4.0	19.26	0.186	164.6	1.76	2.48
4.7	19.45	0.206	164.7	1.77	2.45
5.5	19.62	0.218	165.0	1.76	2.45
6.0	19.73	0.227	165.1	1.76	2.45
6.6	19.85	0.236	165.0	1.76	2.43
7.3	19.95	0.253	165.0	1.76	2.45
8.0	20.07	0.263	165.6	1.76	2.44
8.8	20.17	0.279	165.3	1.76	2.47
9.7	20.28	0.292	165.6	1.77	2.39
10.7	20.38	0.307	165.9	1.78	2.44
11.7	20.52	0.303	165.8	1.77	2.43
12.9	20.66	0.303	165.8	1.76	2.38
14.2	20.82	0.297	165.9	1.75	2.39
15.6	20.97	0.298	166.2	1.74	2.44
17.2	21.13	0.295	165.5	1.73	2.41
18.9	21.26	0.309	164.8	1.75	2.46
20.8	21.40	0.323	164.0	1.73	2.46
22.9	21.52	0.340	164.1	1.73	2.50
25.2	21.65	0.354	163.9	1.69	2.44
27.7	21.79	0.360	163.9	1.68	2.36
30.5	21.93	0.371	164.5	1.70	2.41
33.5	22.18	0.291	143.6	1.57	2.27
36.9	22.21	0.389	167.9	1.62	– –
40.6	22.45	0.373	165.3	1.56	– –
44.6	22.58	0.391	165.6	1.67	– –
49.1	22.74	0.402	165.5	1.72	– –
54.0	22.90	0.415	165.6	1.83	– –
59.4	23.25	0.406	166.2	– –	– –

Table 2.9: Galaxy parameters, cont.

NGC 6086					
Radius (1)	μ_R (2)	ϵ (3)	ϕ (4)	$B-R$ (5)	$U-R$ (6)
2.7	18.77	– –	– –	1.54	2.26
3.2	19.06	0.247	3.6	1.53	2.24
3.9	19.37	0.256	2.7	1.53	2.23
4.7	19.71	0.256	2.5	1.52	2.22
5.5	19.96	0.255	1.8	1.52	2.19
6.0	20.13	0.264	1.8	1.52	2.12
6.6	20.29	0.273	1.6	1.51	2.14
7.3	20.45	0.284	1.3	1.50	2.14
8.0	20.59	0.296	1.3	1.50	2.10
8.8	20.72	0.315	1.3	1.52	2.15
9.7	20.86	0.318	1.5	1.51	2.18
10.5	21.00	0.307	3.3	1.48	2.16
11.5	21.19	0.292	2.2	1.48	2.10
12.7	21.35	0.298	3.0	1.47	2.16
13.9	21.50	0.312	3.2	1.52	2.12
15.3	21.68	0.311	3.4	1.50	2.11
16.9	21.92	0.294	3.3	1.48	2.20
18.6	22.08	0.298	2.4	1.52	2.12
20.0	22.24	0.302	2.9	1.51	2.05
22.0	22.41	0.310	3.9	1.46	2.04
24.2	22.58	0.316	5.1	1.49	1.96
26.6	22.74	0.329	4.8	1.50	2.09
29.2	22.89	0.348	5.7	1.50	– –
32.2	23.02	0.369	5.0	1.49	– –
35.4	23.18	0.372	5.7	1.52	– –
38.9	23.30	0.387	6.2	1.47	– –
42.8	23.46	0.398	7.7	1.38	– –
47.1	23.65	0.392	6.8	1.50	– –
51.8	23.95	0.372	6.8	– –	– –
57.0	24.13	0.366	5.5	– –	– –

Table 2.9: Galaxy parameters, cont.

NGC 6269					
Radius (1)	μ_R (2)	ϵ (3)	ϕ (4)	$B-R$ (5)	$U-R$ (6)
3.2	18.47	– –	– –	– –	– –
3.9	18.72	0.251	81.8	– –	– –
4.7	18.98	0.266	81.5	1.67	– –
5.5	19.18	0.273	81.8	1.66	– –
6.0	19.33	0.274	81.1	1.65	– –
6.6	19.49	0.271	81.1	1.64	2.31
7.3	19.65	0.267	81.1	1.63	2.34
8.0	19.82	0.261	81.2	1.62	2.33
8.8	19.99	0.253	80.8	1.62	2.35
9.7	20.14	0.256	80.1	1.61	2.36
10.5	20.26	0.242	81.7	1.61	2.30
11.5	20.41	0.250	81.0	1.61	2.30
12.7	20.56	0.256	81.2	1.61	2.29
13.9	20.71	0.250	81.3	1.61	2.25
15.3	20.87	0.244	81.2	1.60	2.28
16.8	21.03	0.243	81.3	1.59	2.26
18.5	21.18	0.247	80.9	1.61	2.27
20.4	21.35	0.243	79.8	1.59	2.25
22.4	21.53	0.248	80.4	1.58	2.20
24.6	21.70	0.253	79.7	1.57	2.30
27.1	21.88	0.258	78.1	1.56	– –
29.8	22.05	0.266	77.1	1.56	– –
32.8	22.25	0.266	76.9	1.54	– –
36.1	22.42	0.278	76.4	1.52	– –
39.7	22.59	0.290	77.5	1.54	– –
43.7	22.77	0.296	76.6	1.51	– –
48.0	22.94	0.314	75.5	1.52	– –
52.8	23.09	0.332	76.1	– –	– –
58.1	23.30	0.331	77.9	– –	– –

Table 2.9: Galaxy parameters, cont.

NGC 7626					
Radius	μ_R	ϵ	ϕ	$B-R$	$U-R$
(1)	(2)	(3)	(4)	(5)	(6)
3.8	17.99	0.072	0.8	1.69	2.36
4.6	18.25	0.080	2.8	1.71	2.39
5.3	18.44	0.094	3.3	1.71	2.35
5.8	18.56	0.094	3.3	1.70	2.30
6.4	18.68	0.101	5.6	1.71	2.35
7.0	18.81	0.103	4.9	1.70	2.36
7.7	18.93	0.108	3.8	1.70	2.32
8.5	19.06	0.107	5.2	1.70	2.32
9.3	19.19	0.108	6.3	1.71	2.32
10.2	19.32	0.115	7.4	1.70	2.29
11.3	19.47	0.111	7.4	1.70	2.31
12.4	19.62	0.110	9.5	1.71	2.29
13.6	19.76	0.113	10.2	1.70	2.29
15.0	19.91	0.121	10.7	1.69	2.27
16.5	20.07	0.125	9.7	1.70	2.30
18.2	20.22	0.132	12.0	1.72	2.23
20.0	20.37	0.134	10.7	1.70	2.23
22.0	20.53	0.145	12.9	1.69	2.21
24.2	20.68	0.151	11.1	1.68	2.25
26.6	20.84	0.151	11.4	1.67	2.19
29.2	20.99	0.161	15.1	1.69	2.20
32.2	21.16	0.157	12.4	1.67	2.19
35.4	21.31	0.173	10.9	1.68	2.18
38.9	21.49	0.182	12.5	1.70	2.16
42.8	21.67	0.181	12.5	1.67	--
47.1	21.87	0.177	12.5	1.66	--
51.8	22.12	0.143	11.8	1.67	--
57.0	22.31	0.155	10.7	1.70	--
62.7	22.55	0.136	7.2	1.68	--
69.0	22.74	0.157	13.5	--	--

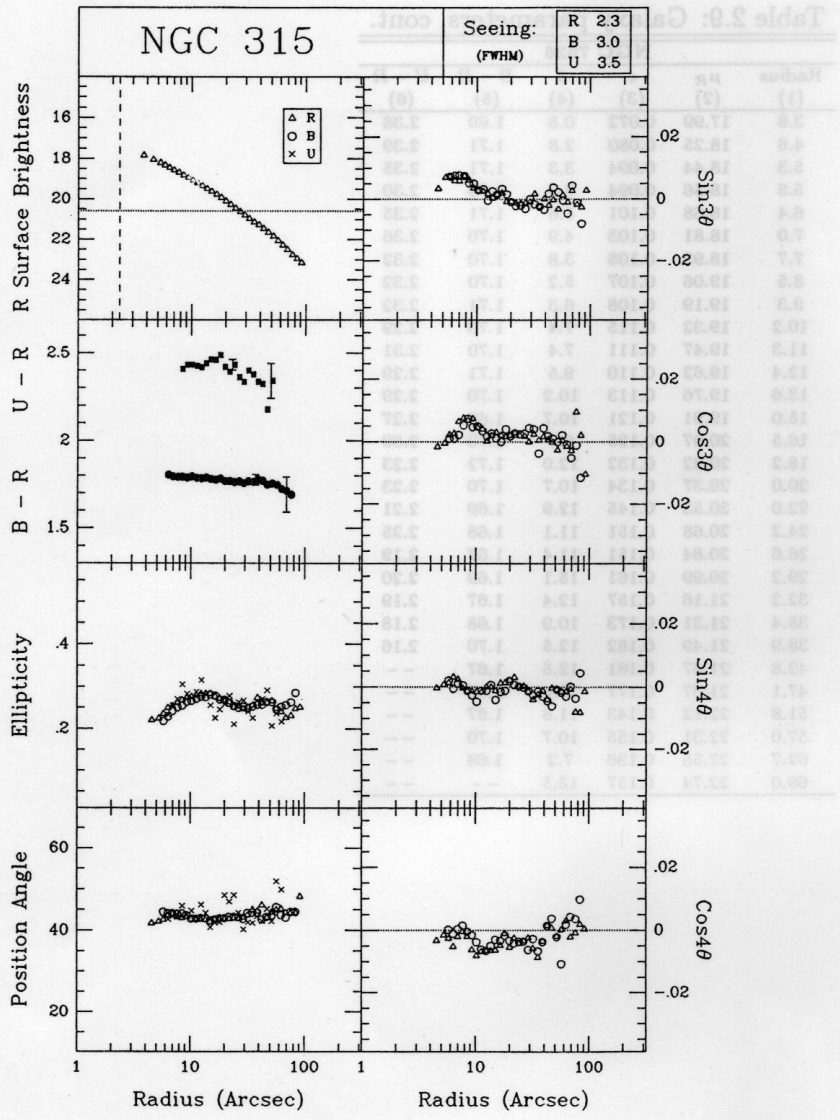

Figure 2.17: *The R-band surface brightness, ellipticity, and major axis position angle profiles, as well as the $B-R$ and $U-R$ color gradients and the cos 3θ (C3), sin 3θ (S3), cos 4θ (C4), and sin 4θ (S4) profiles. The data are plotted as a function of major axis radius in arcseconds. Data in the R band are indicated by open triangles, in B by open circles and in U by crosses. Representative error bars for a 1% uncertainty in the sky are shown at two radii for the color profiles.*

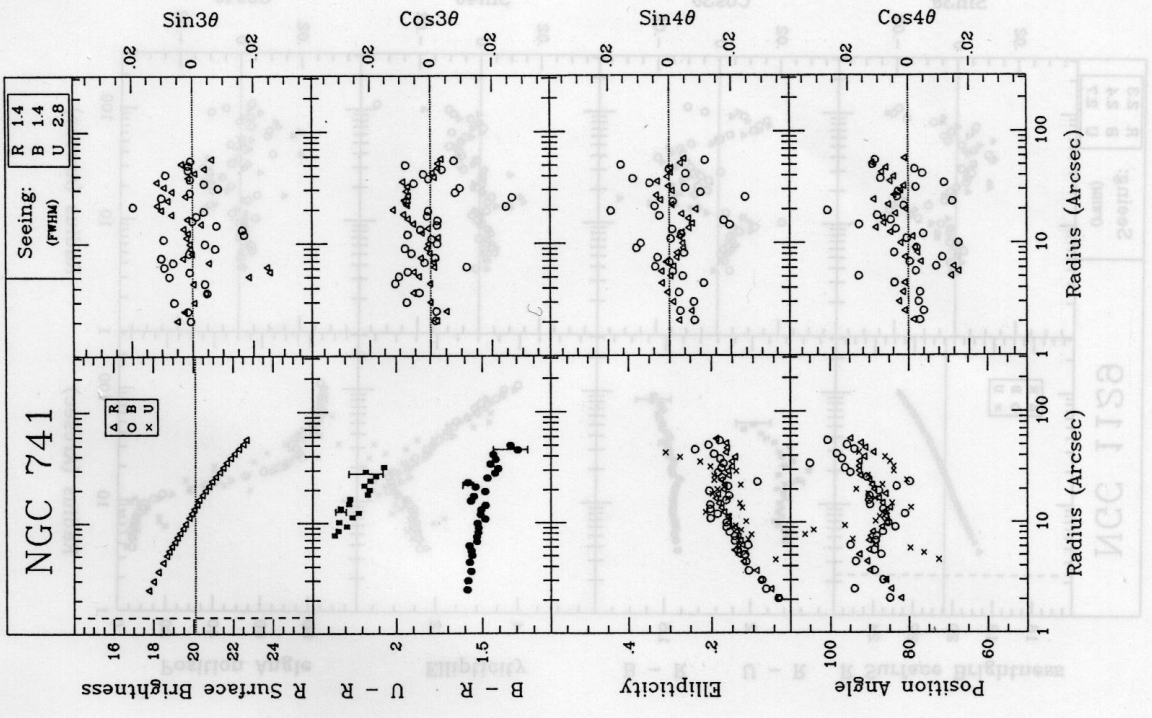
NGC 741
Seeing: (FWHM)
R 1.4
B 1.4
U 2.8
R Surface Brightness
U − R
B − R
Ellipticity
Position Angle
Sin3θ
Cos3θ
Sin4θ
Cos4θ
Radius (Arcsec)

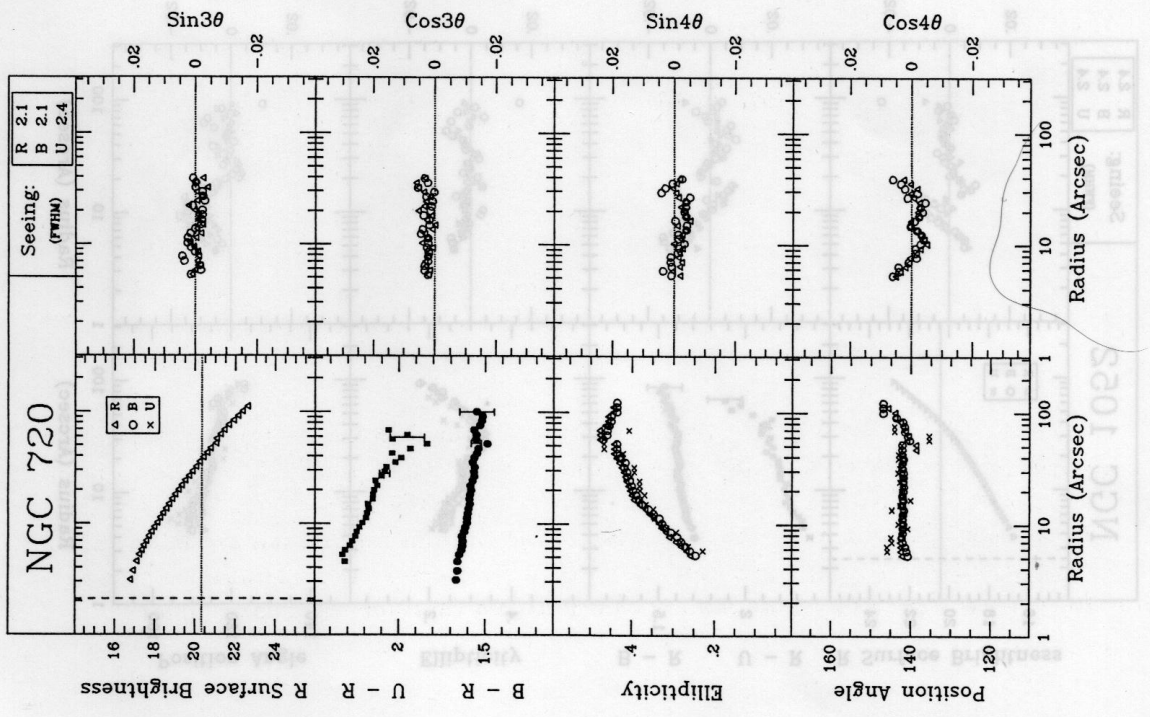
NGC 720
Seeing: (FWHM)
R 2.1
B 2.1
U 2.4
R Surface Brightness
U − R
B − R
Ellipticity
Position Angle
Sin3θ
Cos3θ
Sin4θ
Cos4θ
Radius (Arcsec)

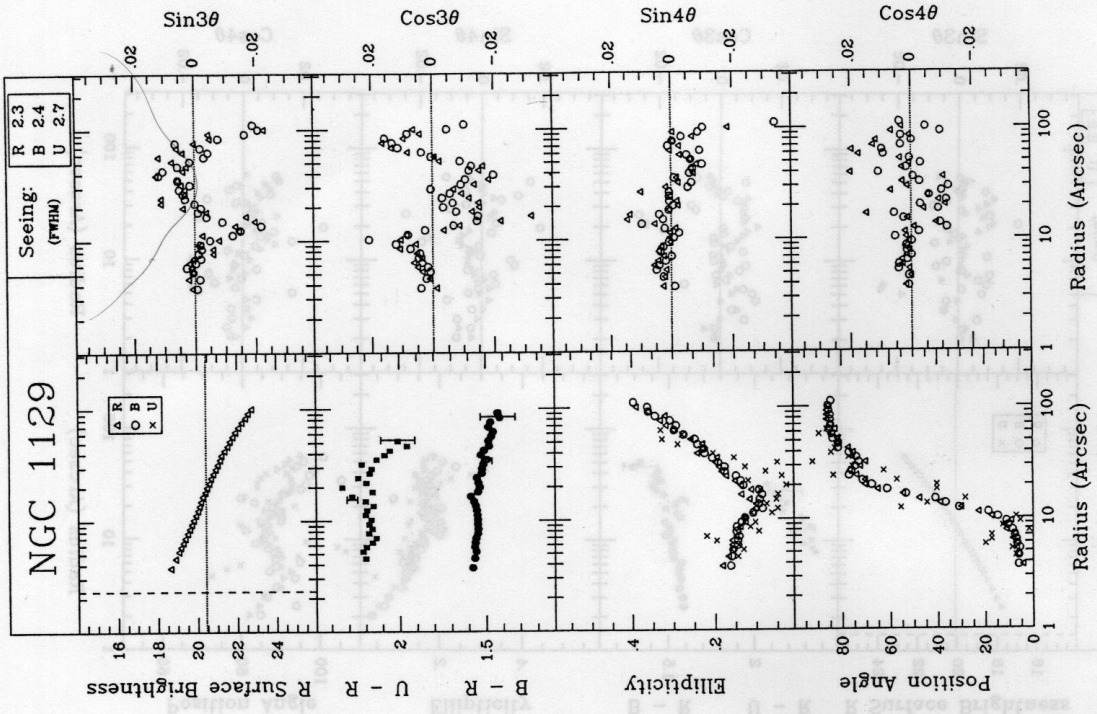
NGC 1129
Seeing: (FWHM)
R 2.3
B 2.4
U 2.7
Sin3θ
Cos3θ
Sin4θ
Cos4θ
R Surface Brightness
U − R
B − R
Ellipticity
Position Angle
Radius (Arcsec)

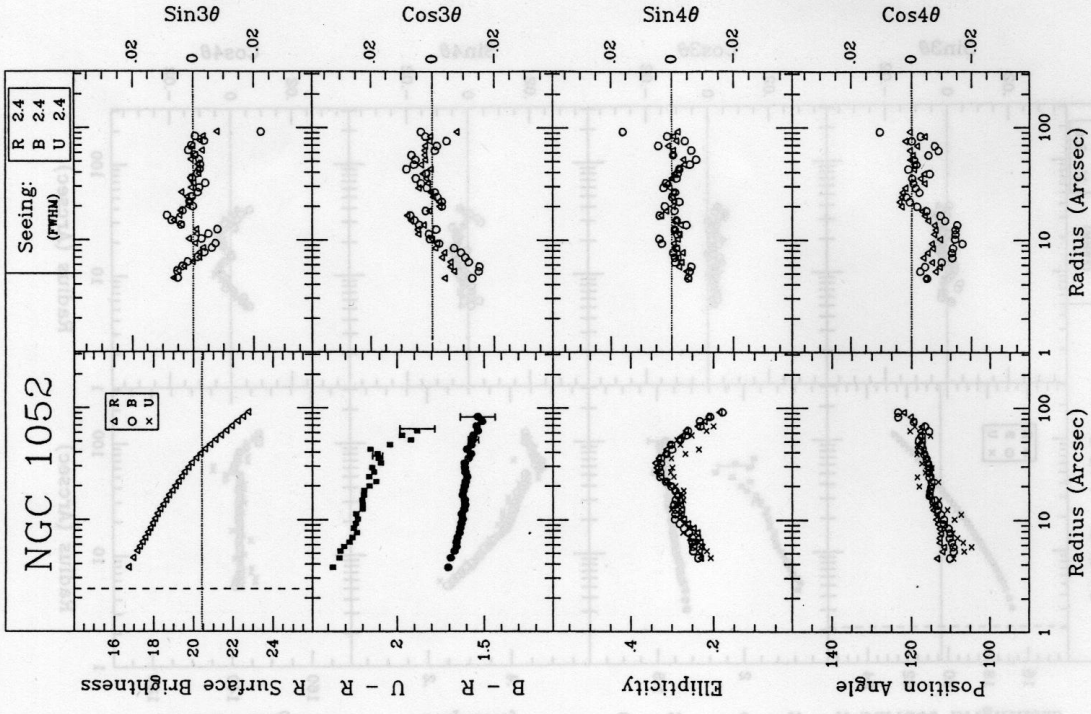
NGC 1052
Seeing: (FWHM)
R 2.4
B 2.4
U 2.4
Sin3θ
Cos3θ
Sin4θ
Cos4θ
R Surface Brightness
U − R
B − R
Ellipticity
Position Angle
Radius (Arcsec)

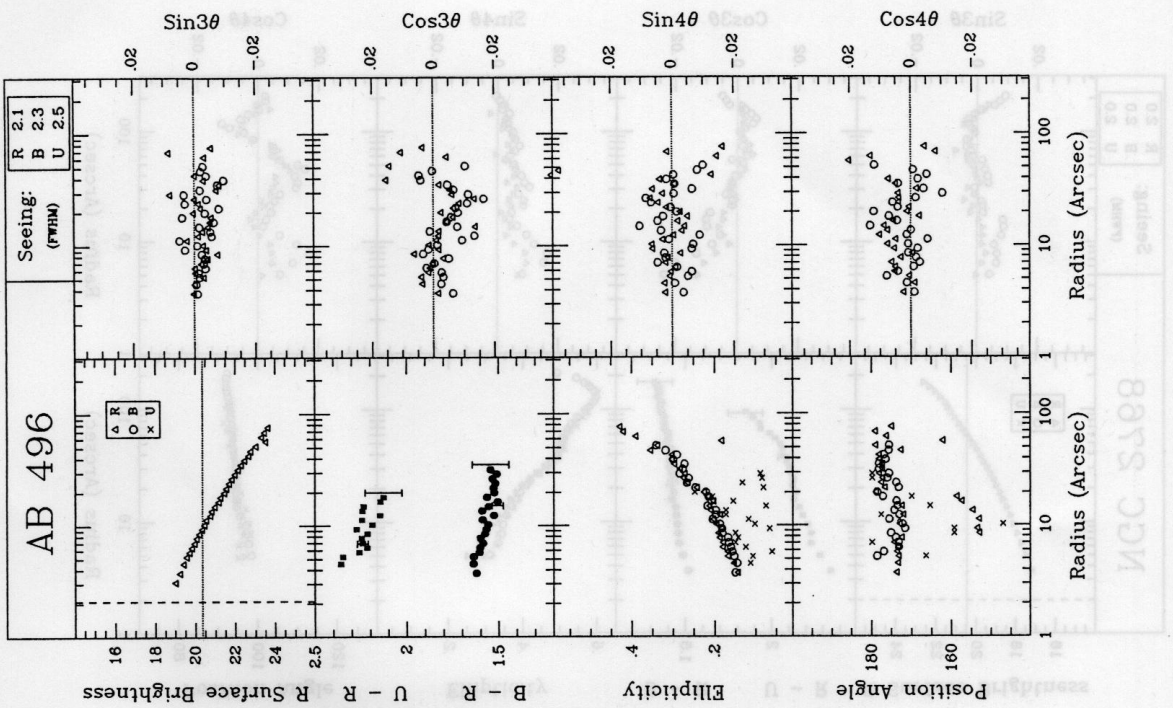
AB 496
Seeing: (FWHM)
R 2.1
B 2.3
U 2.5
Sin3θ
Cos3θ
Sin4θ
Cos4θ
R Surface Brightness
U − R
B − R
Ellipticity
Position Angle
Radius (Arcsec)

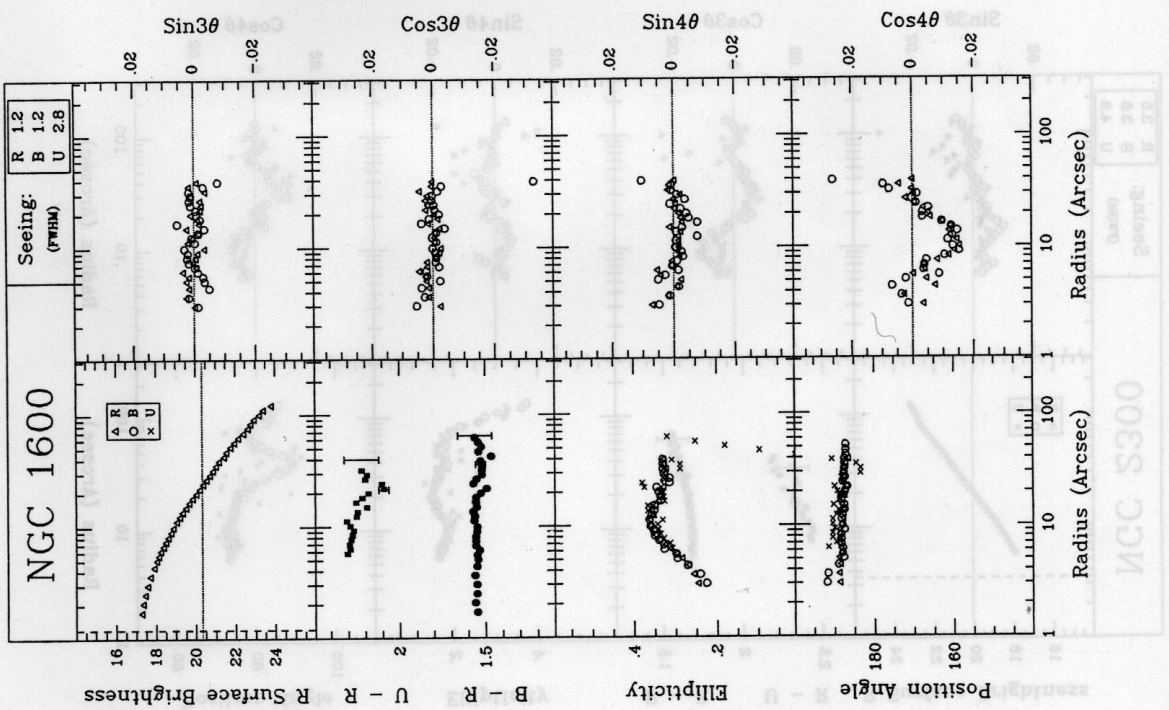
NGC 1600
Seeing: (FWHM)
R 1.2
B 1.2
U 2.8
Sin3θ
Cos3θ
Sin4θ
Cos4θ
R Surface Brightness
U − R
B − R
Ellipticity
Position Angle
Radius (Arcsec)

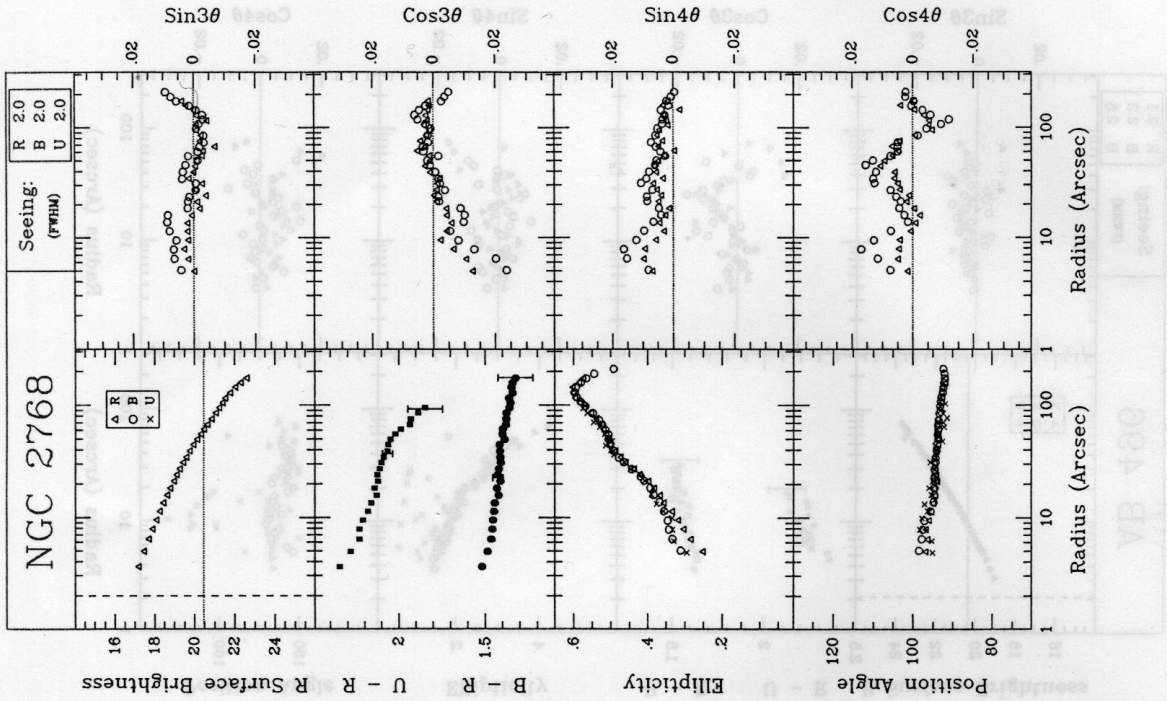
NGC 2768
Seeing: (FWHM)
R 2.0
B 2.0
U 2.0
Sin3θ
Cos3θ
Sin4θ
Cos4θ
R Surface Brightness
U − R
B − R
Ellipticity
Position Angle
Radius (Arcsec)

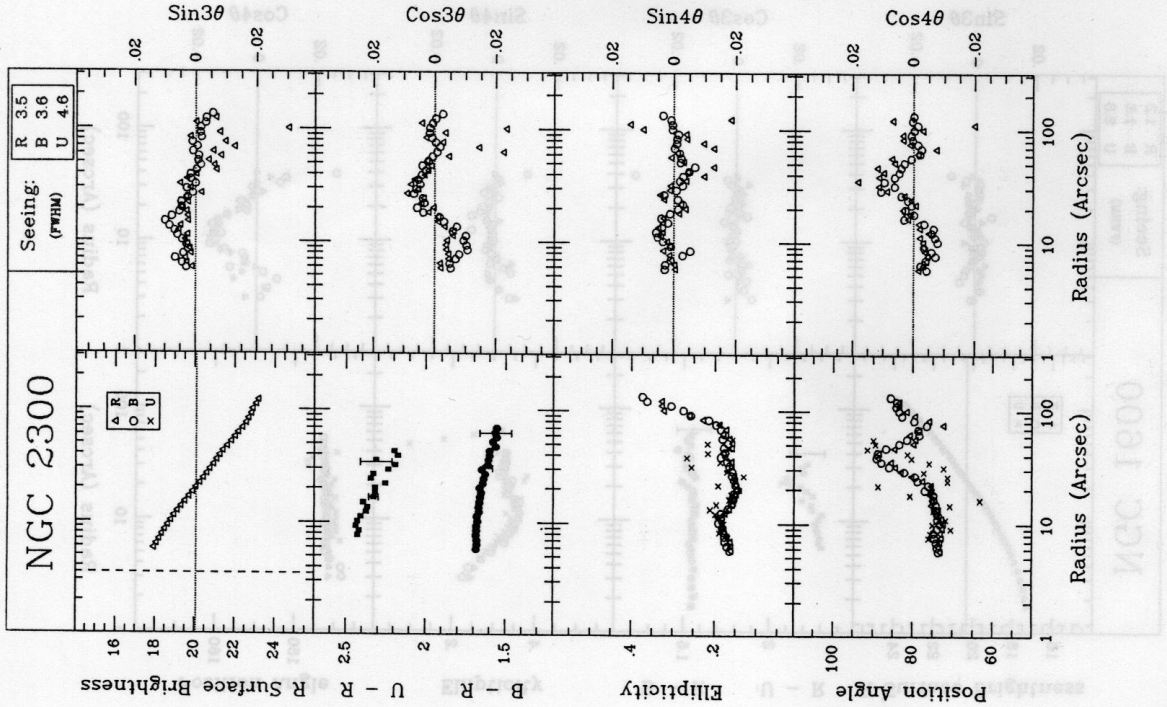
NGC 2300
Seeing: (FWHM)
R 3.5
B 3.6
U 4.6
Sin3θ
Cos3θ
Sin4θ
Cos4θ
R Surface Brightness
U − R
B − R
Ellipticity
Position Angle
Radius (Arcsec)

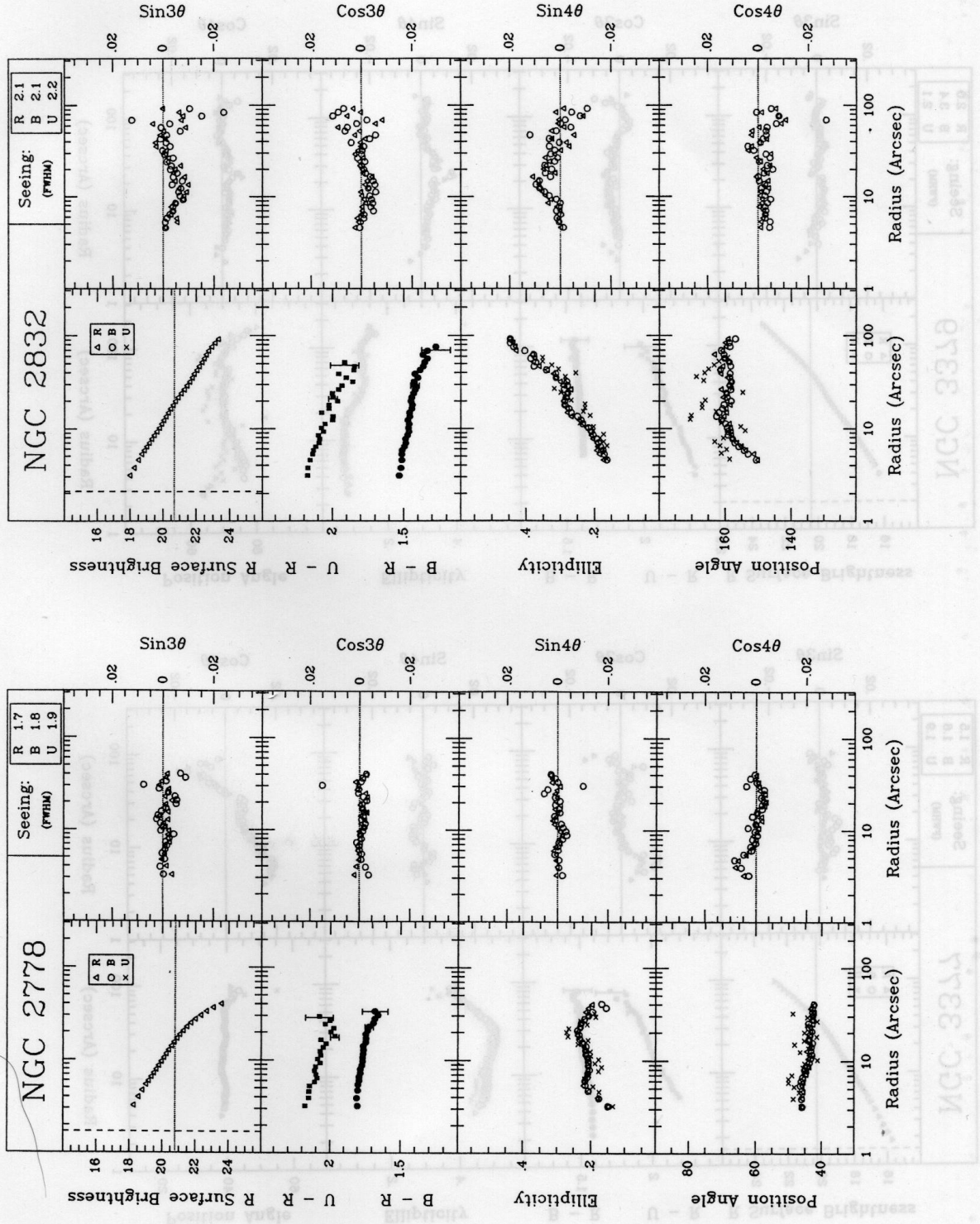
NGC 2832
Seeing: (FWHM)
R 2.1
B 2.1
U 2.2
Sin3θ
Cos3θ
Sin4θ
Cos4θ
R Surface Brightness
U − R
B − R
Ellipticity
Position Angle
Radius (Arcsec)
NGC 2778
R 1.7
B 1.8
U 1.9

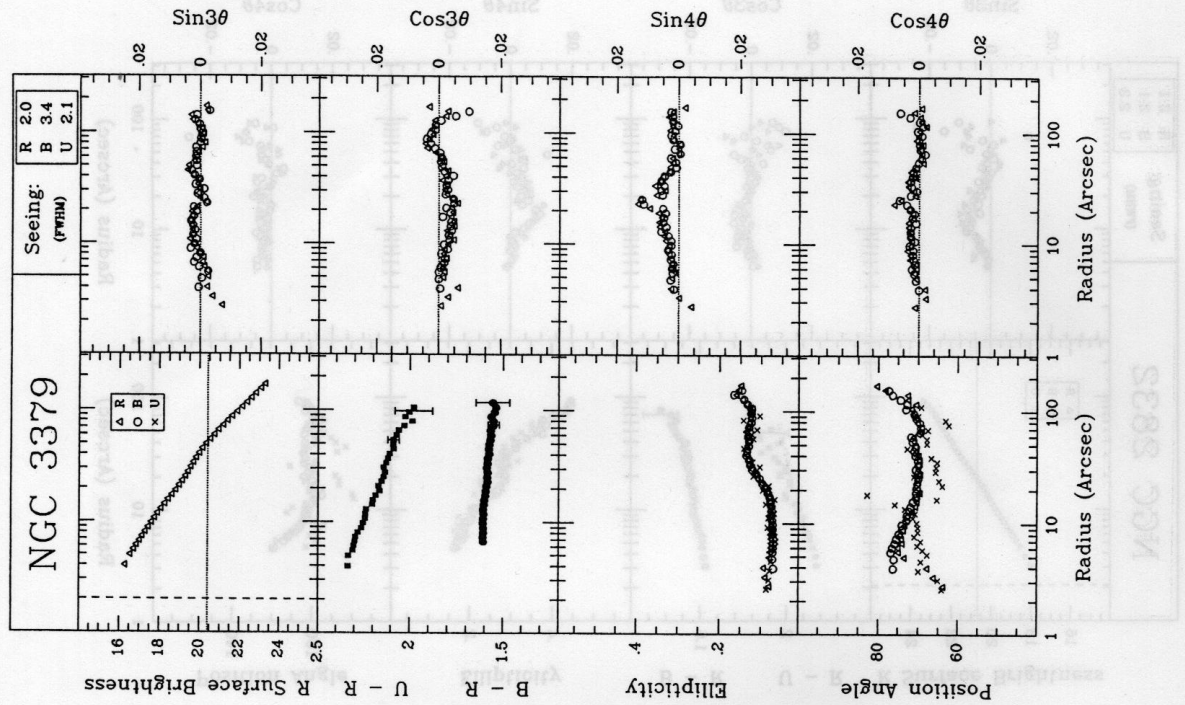
NGC 3379
Seeing: (FWHM)
R 2.0
B 3.4
U 2.1
Sin3θ
Cos3θ
Sin4θ
Cos4θ
R Surface Brightness
U − R
B − R
Ellipticity
Position Angle
Radius (Arcsec)

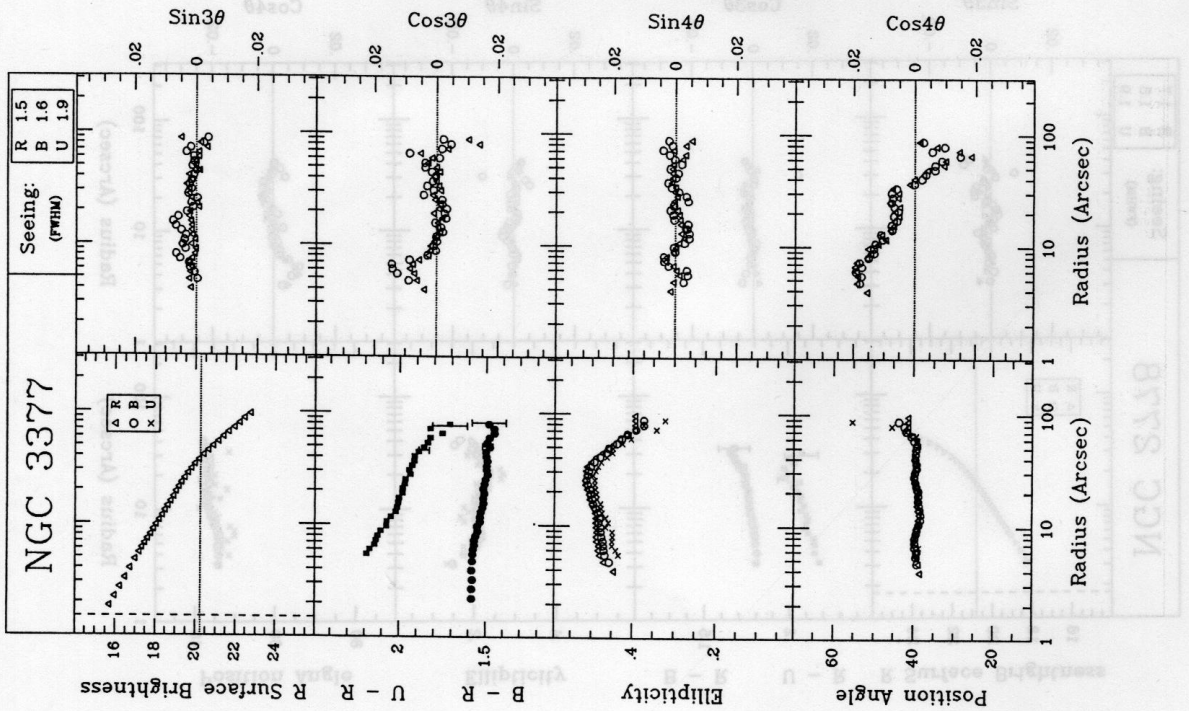
NGC 3377
Seeing: (FWHM)
R 1.5
B 1.6
U 1.9
Sin3θ
Cos3θ
Sin4θ
Cos4θ
R Surface Brightness
U − R
B − R
Ellipticity
Position Angle
Radius (Arcsec)

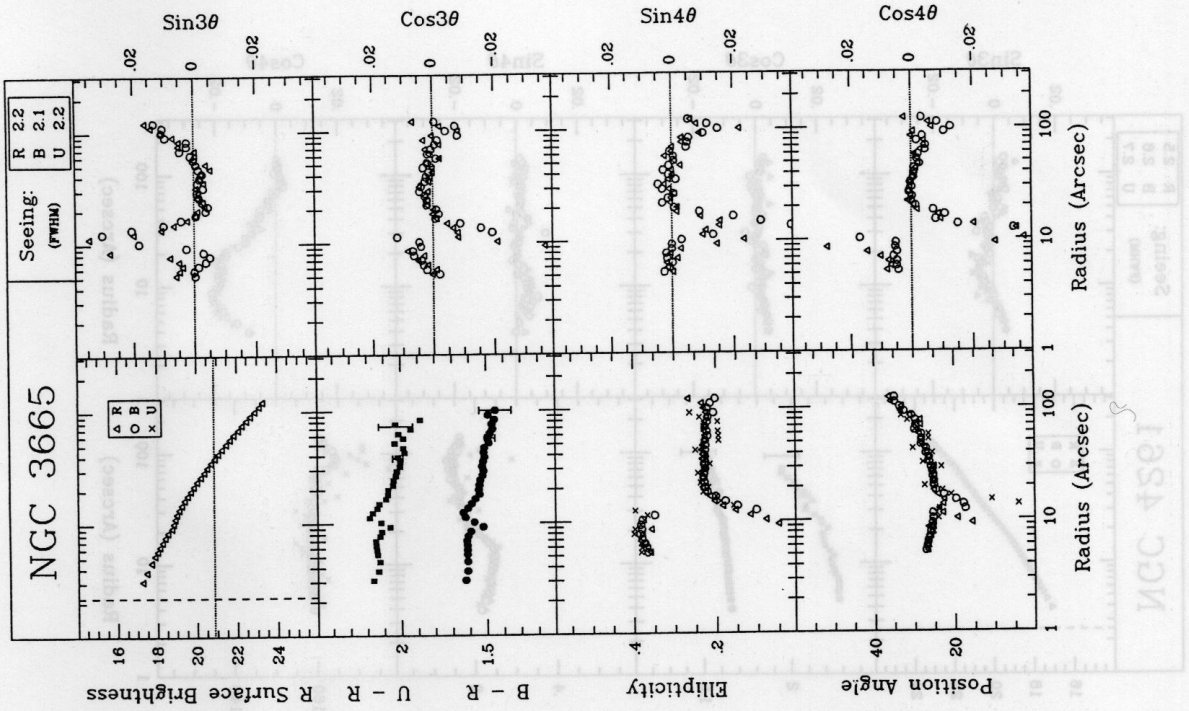
NGC 3665
Seeing: (FWHM)
R 2.2
B 2.1
U 2.2
Sin3θ
Cos3θ
Sin4θ
Cos4θ
R Surface Brightness
B − R
U − R
Ellipticity
Position Angle
Radius (Arcsec)

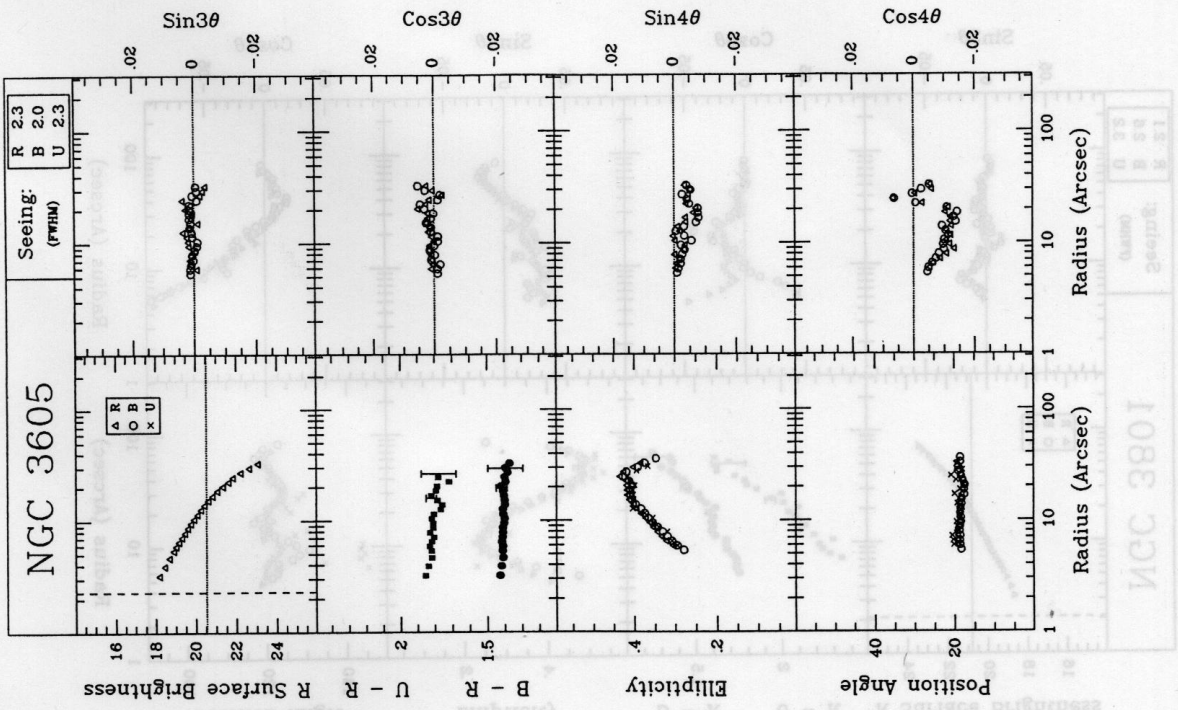
NGC 3605
Seeing: (FWHM)
R 2.3
B 2.0
U 2.3
Sin3θ
Cos3θ
Sin4θ
Cos4θ
R Surface Brightness
B − R
U − R
Ellipticity
Position Angle
Radius (Arcsec)

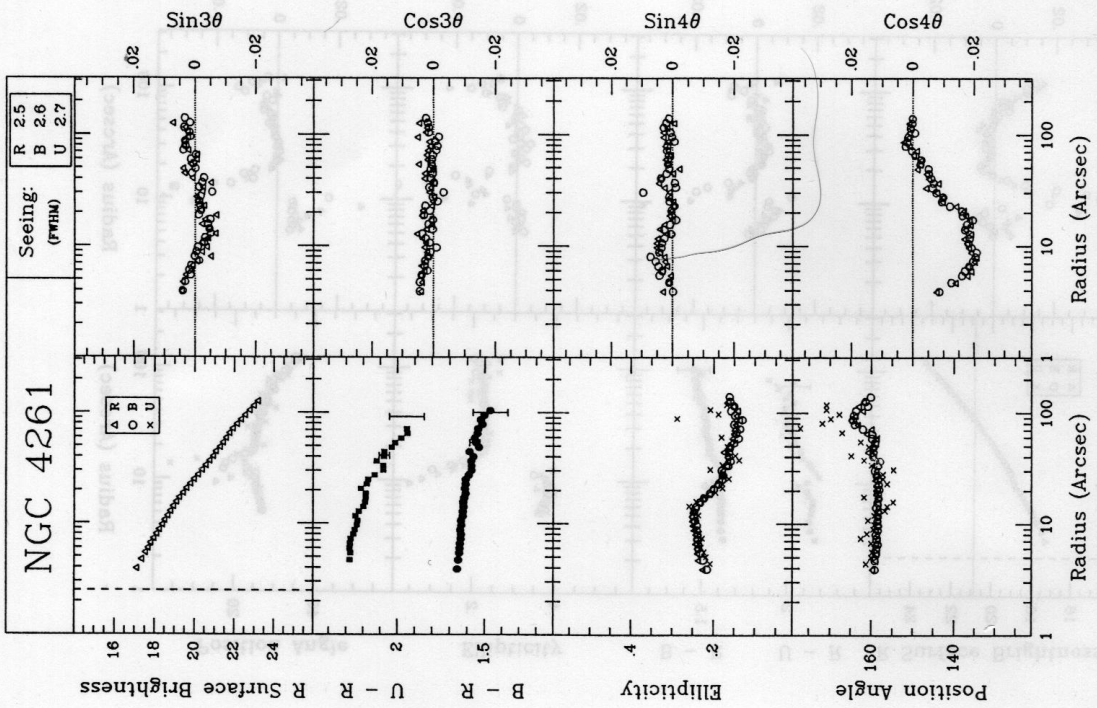
NGC 4261
Seeing: (FWHM)
R 2.5
B 2.6
U 2.7
Sin3θ
Cos3θ
Sin4θ
Cos4θ
R Surface Brightness
B − R
U − R
Ellipticity
Position Angle
Radius (Arcsec)

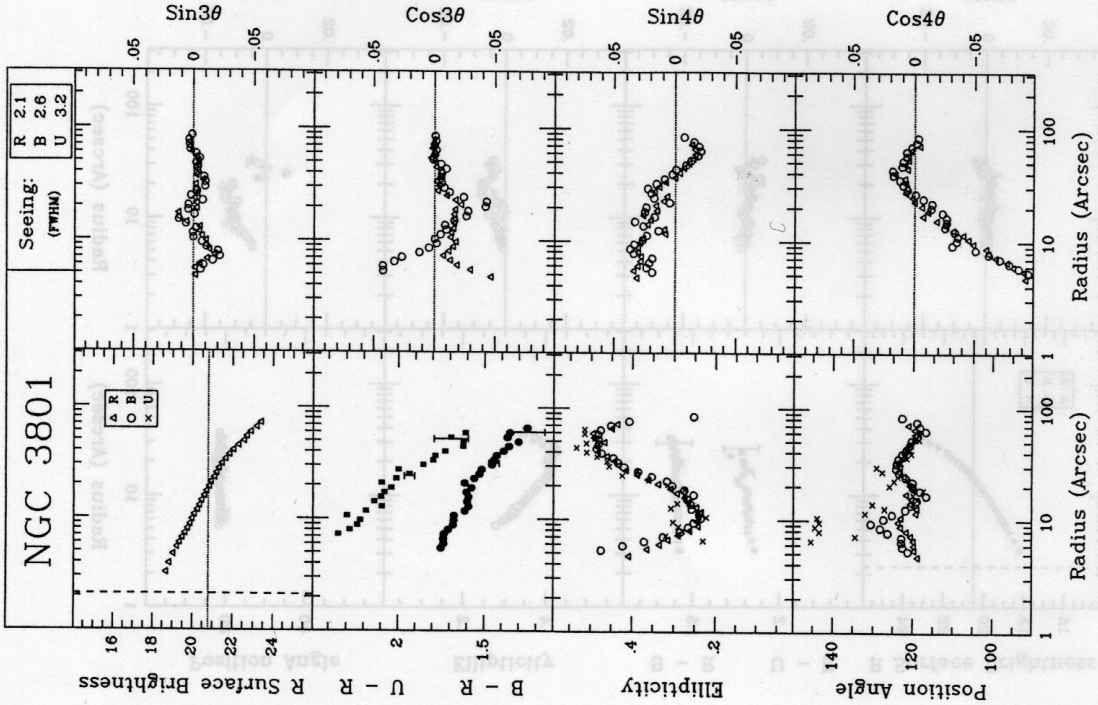
NGC 3801
Seeing: (FWHM)
R 2.1
B 2.6
U 3.2
Sin3θ
Cos3θ
Sin4θ
Cos4θ
R Surface Brightness
B − R
U − R
Ellipticity
Position Angle
Radius (Arcsec)

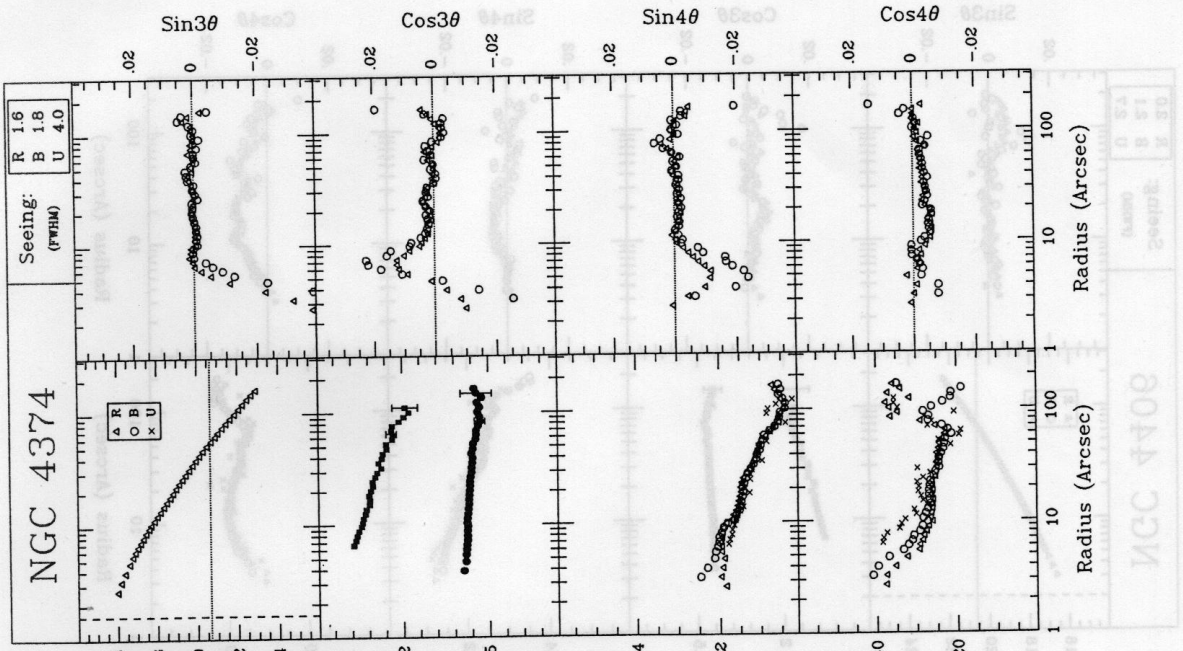
NGC 4374
Seeing: (FWHM)
R 1.6
B 1.8
U 4.0
Sin3θ
Cos3θ
Sin4θ
Cos4θ
R Surface Brightness
B − R
U − R
Ellipticity
Position Angle
Radius (Arcsec)

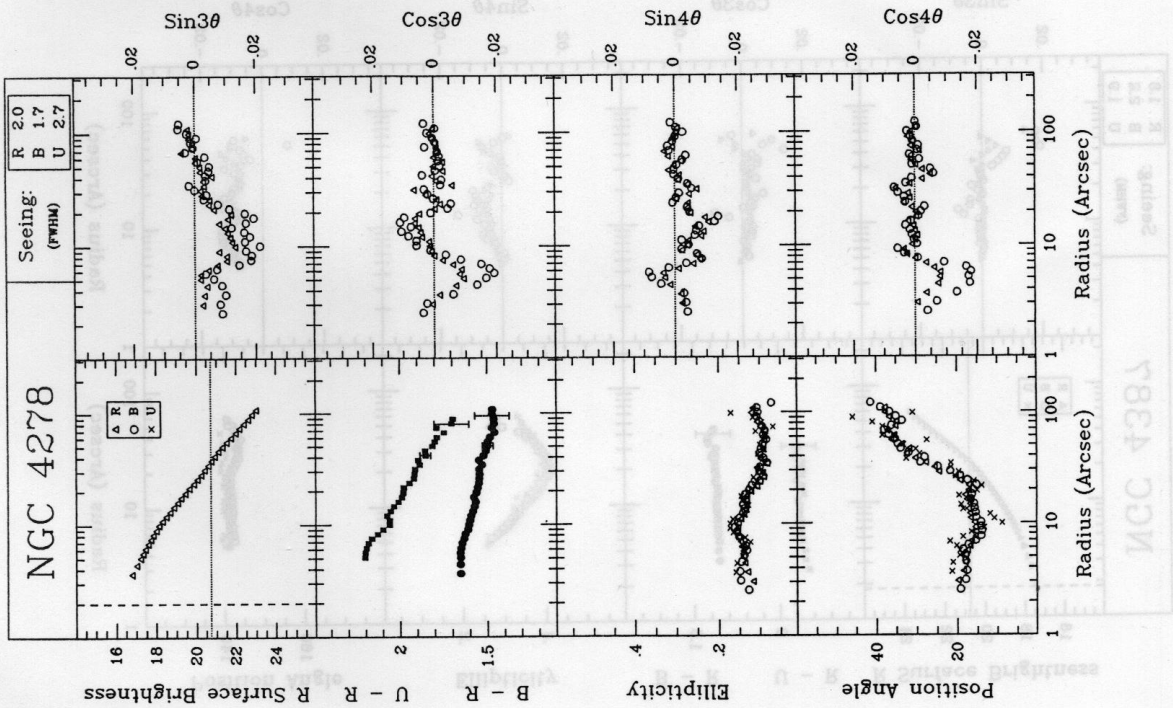
NGC 4278
Seeing: (FWHM)
R 2.0
B 1.7
U 2.7
Sin3θ
Cos3θ
Sin4θ
Cos4θ
R Surface Brightness
B − R
U − R
Ellipticity
Position Angle
Radius (Arcsec)

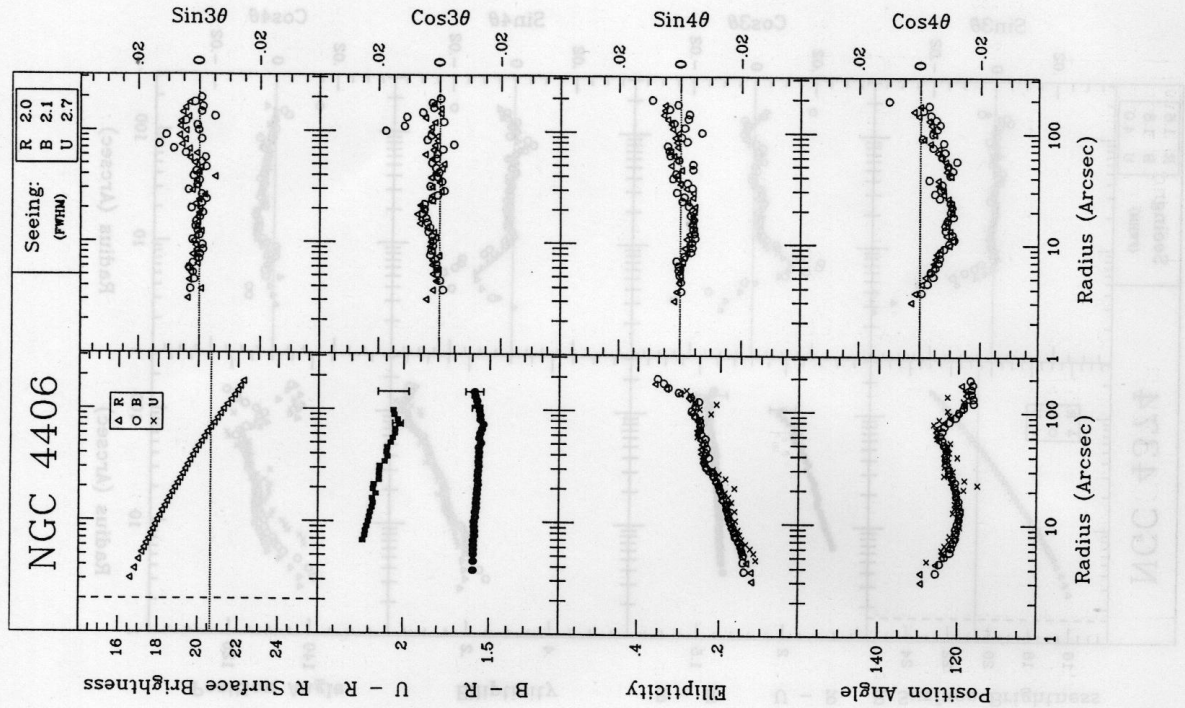
NGC 4406
Seeing: (FWHM)
R 2.0
B 2.1
U 2.7
Sin3θ
Cos3θ
Sin4θ
Cos4θ
R Surface Brightness
U − R
B − R
Ellipticity
Position Angle
Radius (Arcsec)

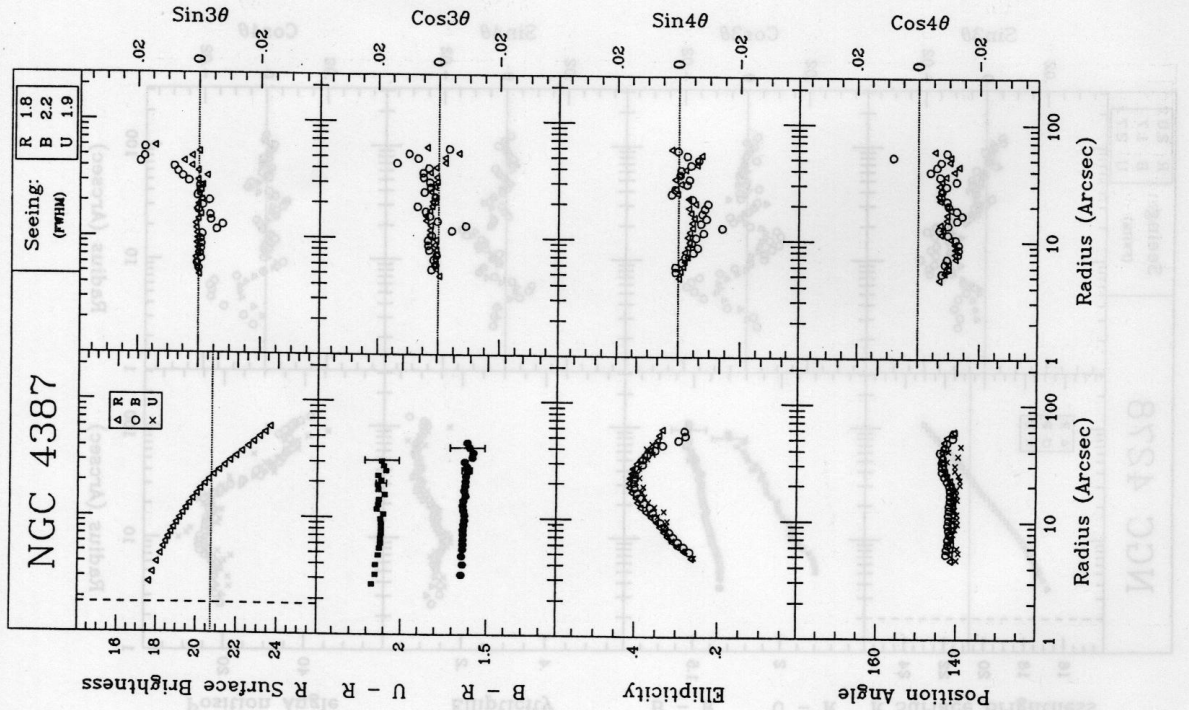
NGC 4387
Seeing: (FWHM)
R 1.8
B 2.2
U 1.9
Sin3θ
Cos3θ
Sin4θ
Cos4θ
R Surface Brightness
U − R
B − R
Ellipticity
Position Angle
Radius (Arcsec)

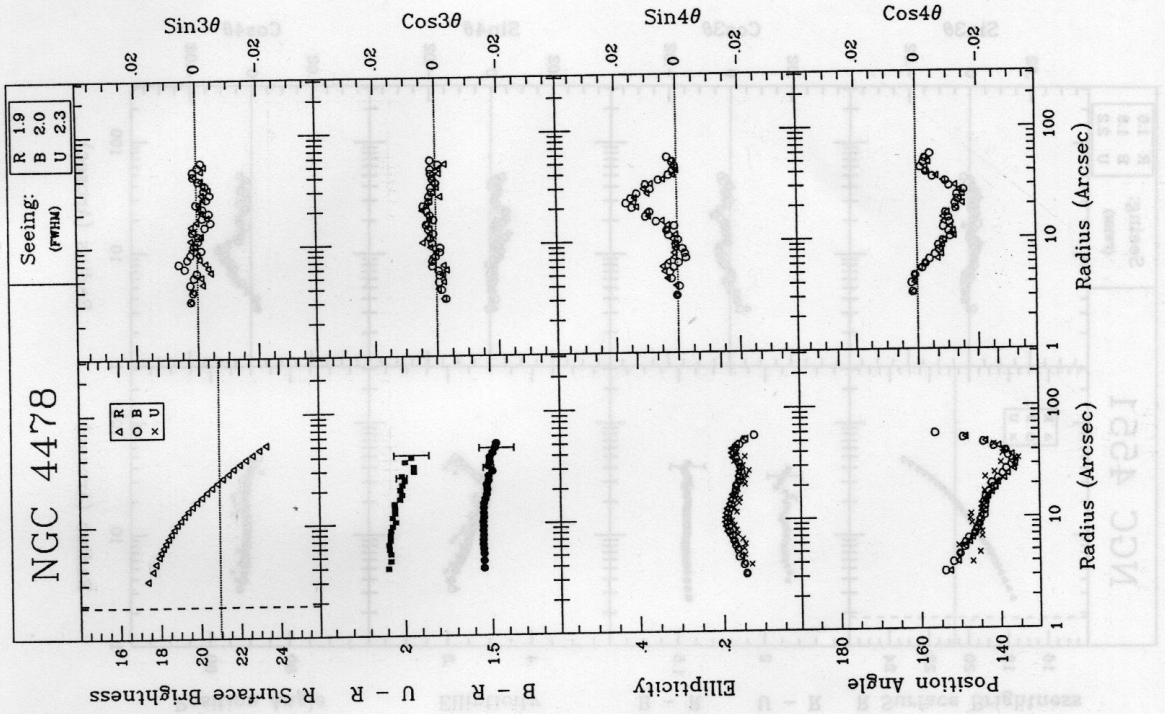
NGC 4478
Seeing: (FWHM)
R 1.9
B 2.0
U 2.3
Sin3θ
Cos3θ
Sin4θ
Cos4θ
R Surface Brightness
U − R
B − R
Ellipticity
Position Angle
Radius (Arcsec)

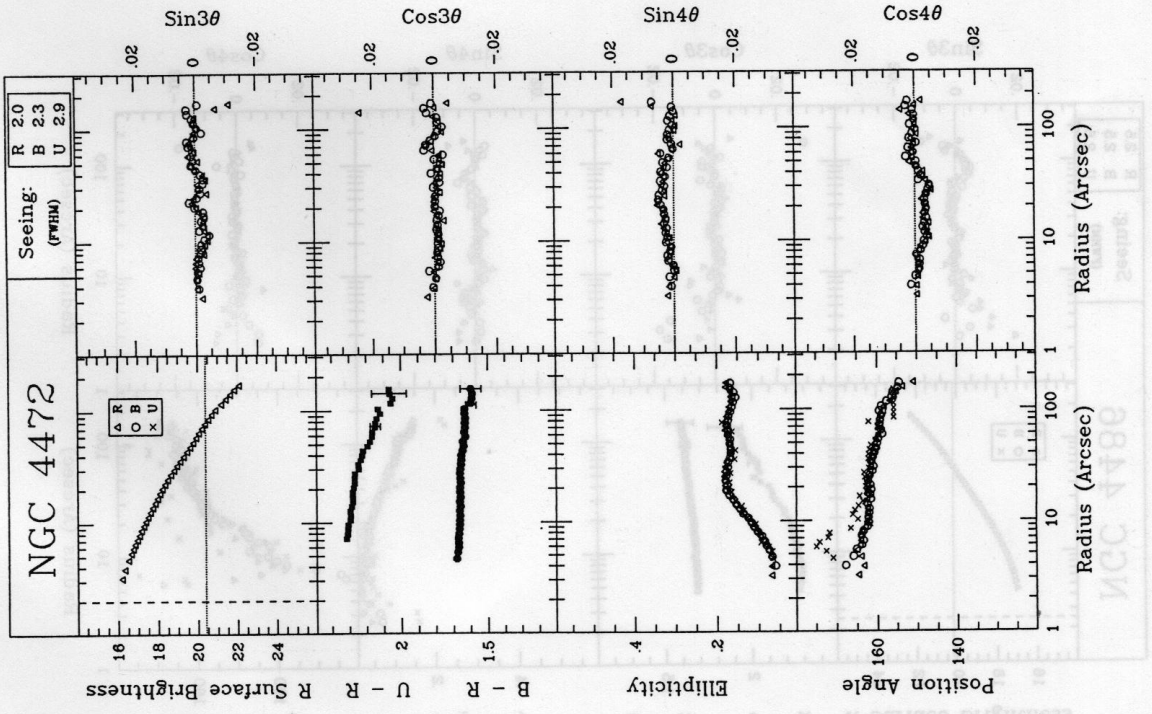
NGC 4472
Seeing: (FWHM)
R 2.0
B 2.3
U 2.9
Sin3θ
Cos3θ
Sin4θ
Cos4θ
R Surface Brightness
U − R
B − R
Ellipticity
Position Angle
Radius (Arcsec)

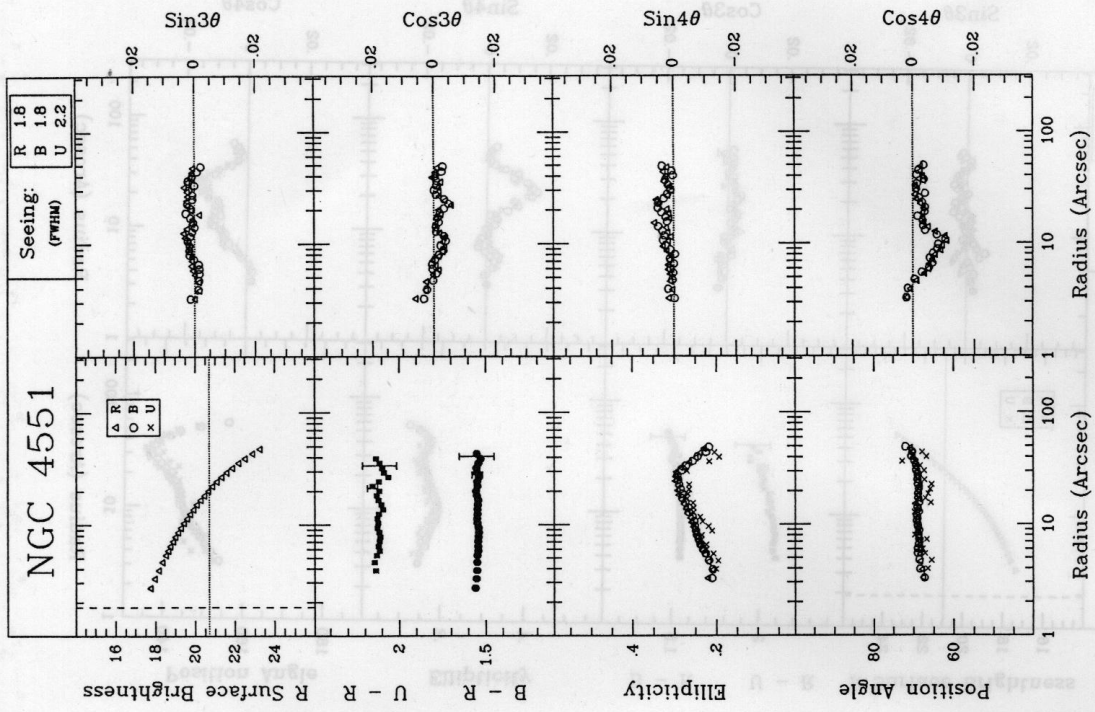
NGC 4551
Seeing: (FWHM)
R 1.8
B 1.8
U 2.2
R Surface Brightness
U − R
B − R
Ellipticity
Position Angle
Sin3θ
Cos3θ
Sin4θ
Cos4θ
Radius (Arcsec)

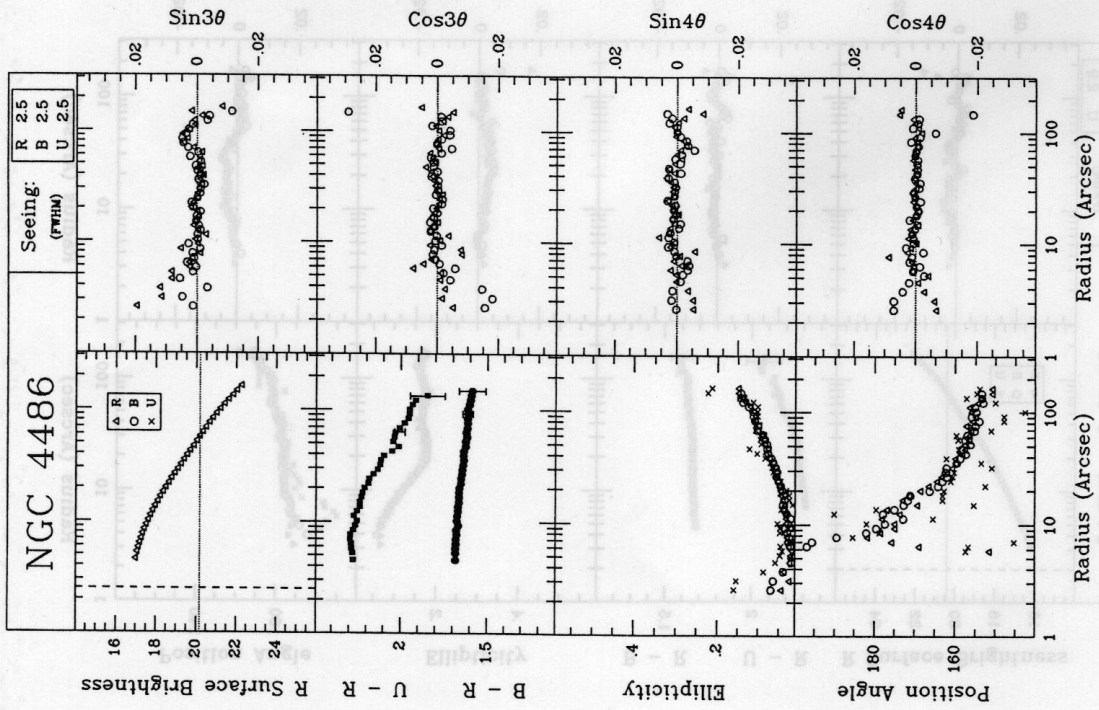
NGC 4486
Seeing: (FWHM)
R 2.5
B 2.5
U 2.5
R Surface Brightness
U − R
B − R
Ellipticity
Position Angle
Sin3θ
Cos3θ
Sin4θ
Cos4θ
Radius (Arcsec)

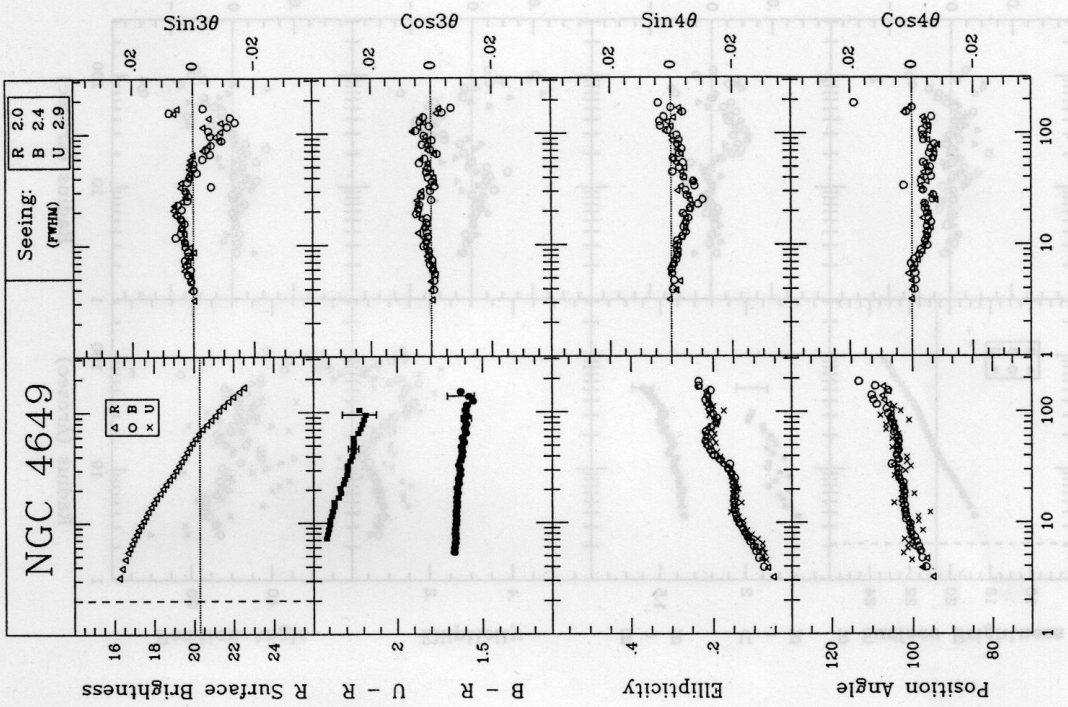
NGC 4649
Seeing: (FWHM)
R 2.0
B 2.4
U 2.9
R Surface Brightness
U − R
B − R
Ellipticity
Position Angle
Sin3θ
Cos3θ
Sin4θ
Cos4θ
Radius (Arcsec)

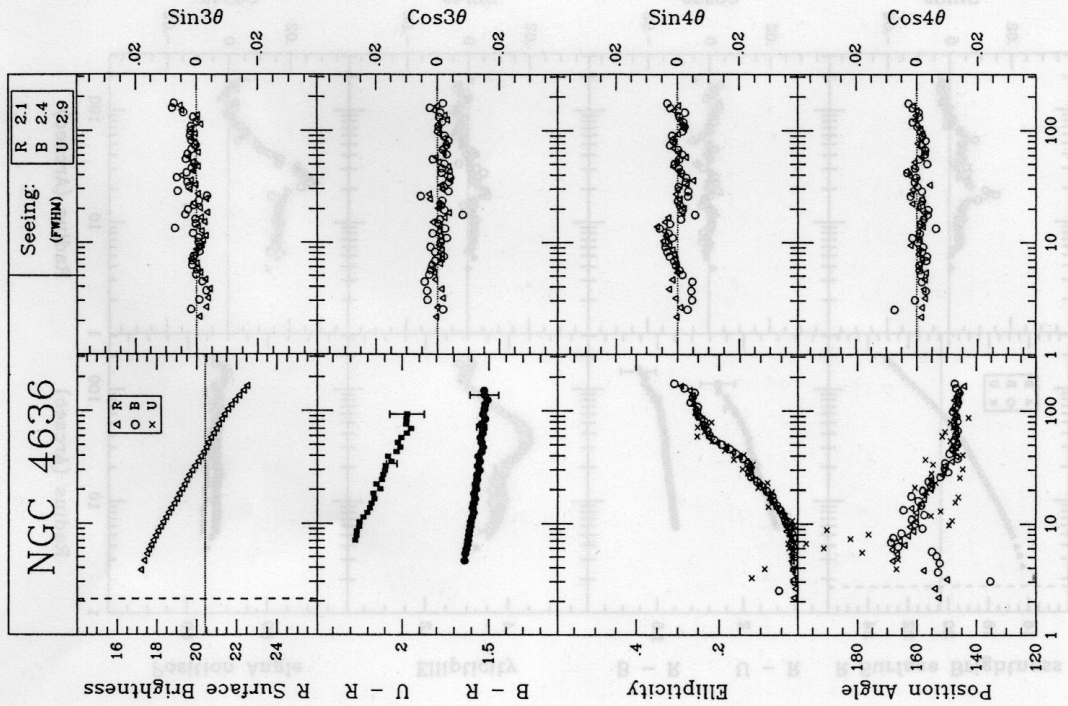
NGC 4636
Seeing: (FWHM)
R 2.1
B 2.4
U 2.9
R Surface Brightness
U − R
B − R
Ellipticity
Position Angle
Sin3θ
Cos3θ
Sin4θ
Cos4θ
Radius (Arcsec)

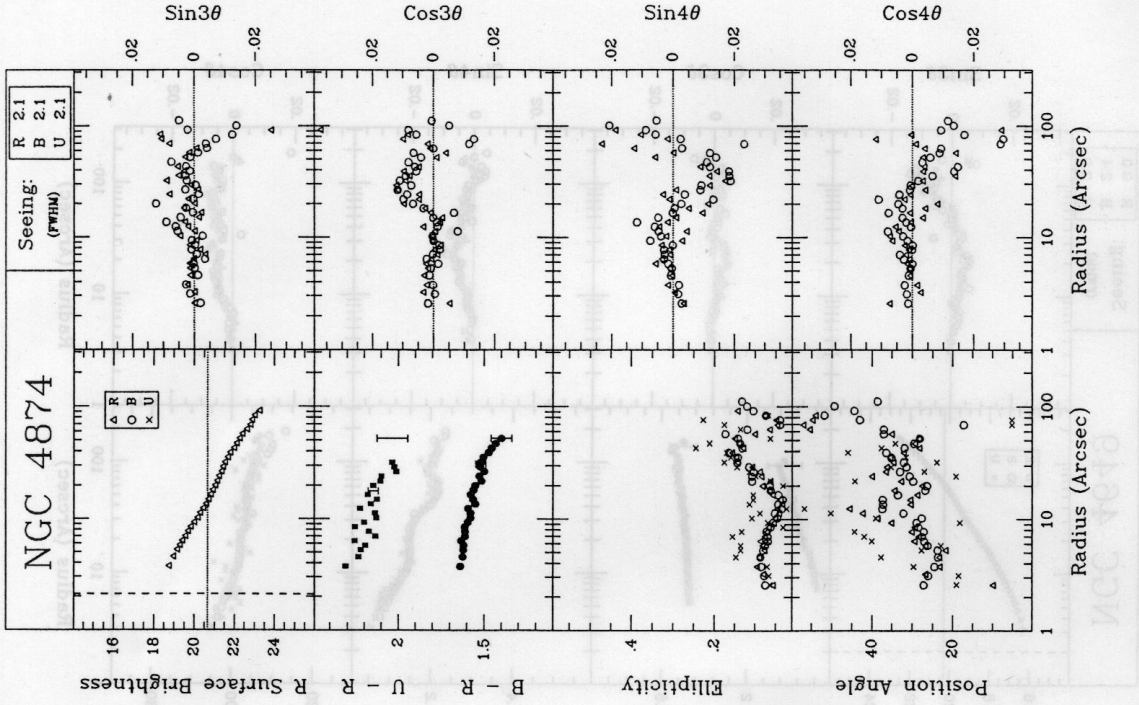
NGC 4874
Seeing: (FWHM)
R 2.1
B 2.1
U 2.1
R Surface Brightness
U − R
B − R
Ellipticity
Position Angle
Sin3θ
Cos3θ
Sin4θ
Cos4θ
Radius (Arcsec)

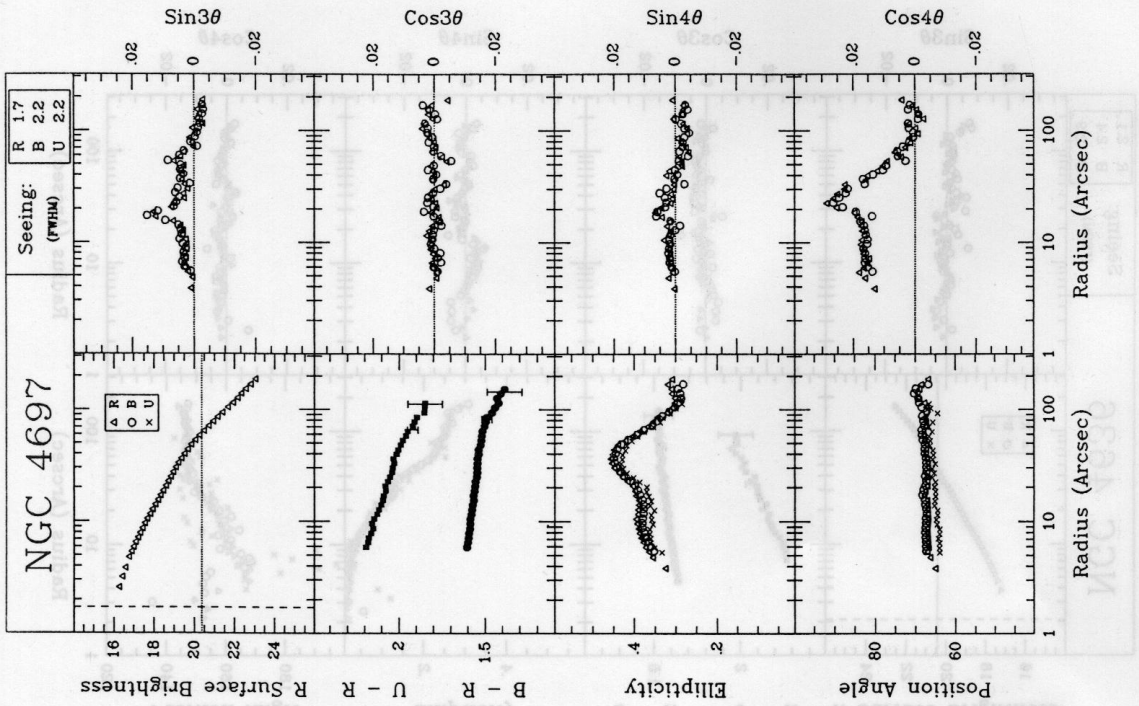
NGC 4697
Seeing: (FWHM)
R 1.7
B 2.2
U 2.2
R Surface Brightness
U − R
B − R
Ellipticity
Position Angle
Sin3θ
Cos3θ
Sin4θ
Cos4θ
Radius (Arcsec)

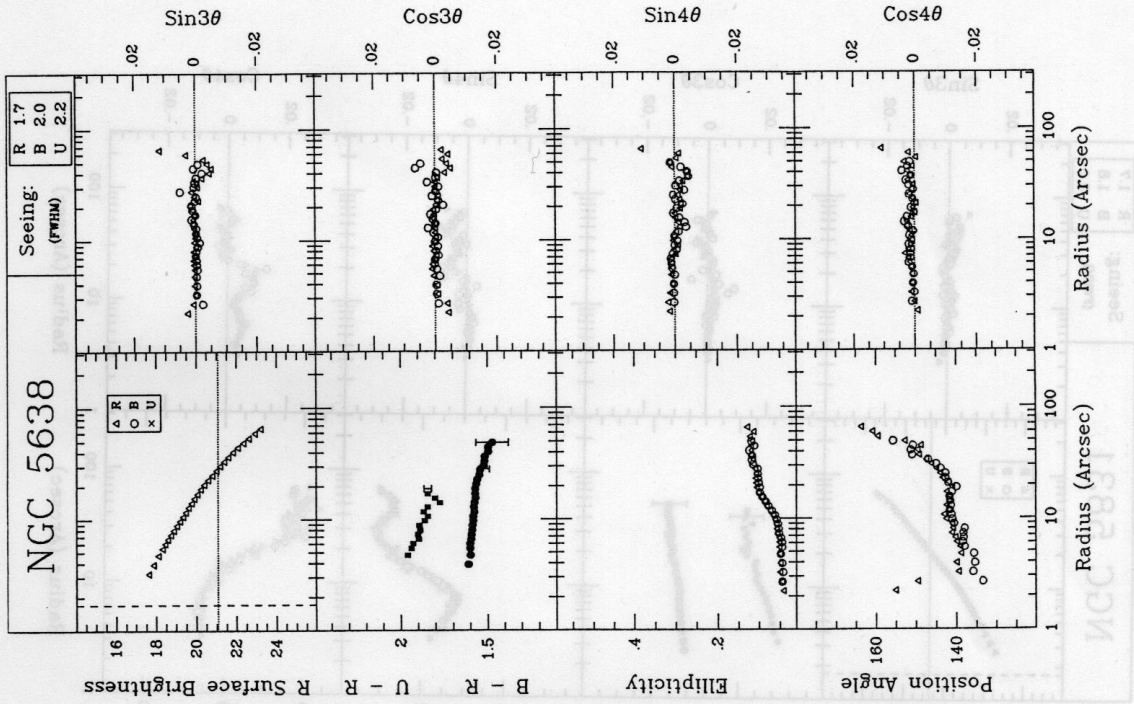
NGC 5638
Seeing: (FWHM)
R 1.7
B 2.0
U 2.2
Sin3θ
Cos3θ
Sin4θ
Cos4θ
R Surface Brightness
B − R
U − R
Ellipticity
Position Angle
Radius (Arcsec)

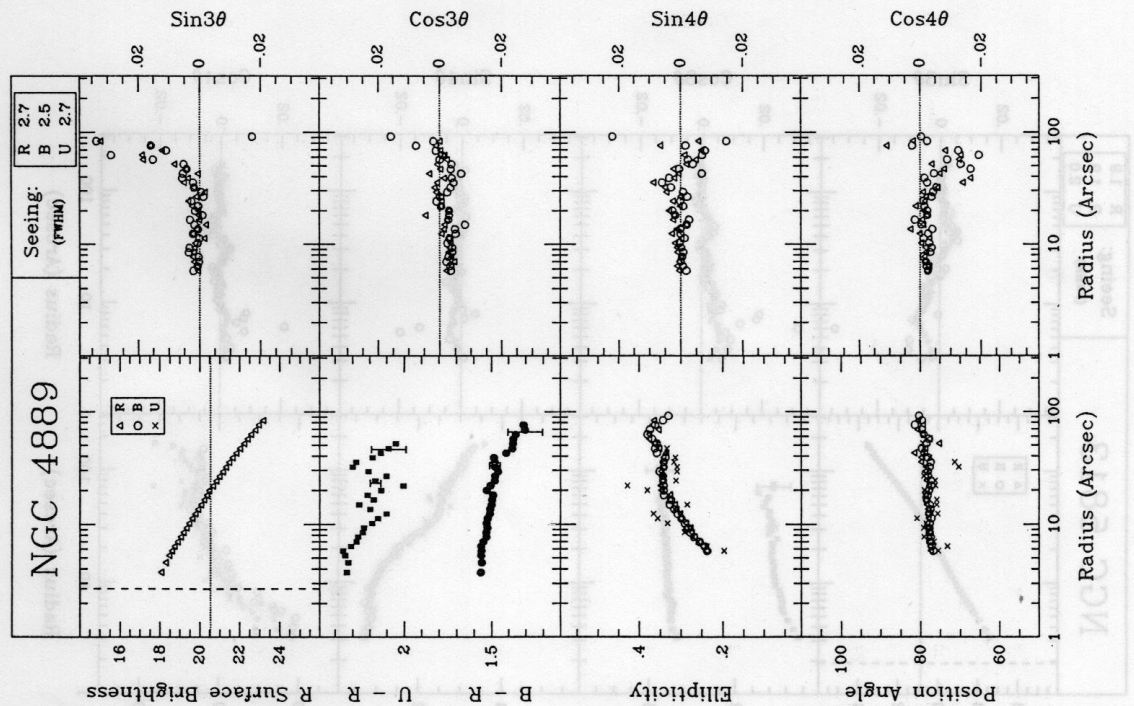
NGC 4889
Seeing: (FWHM)
R 2.7
B 2.5
U 2.7
Sin3θ
Cos3θ
Sin4θ
Cos4θ
R Surface Brightness
B − R
U − R
Ellipticity
Position Angle
Radius (Arcsec)

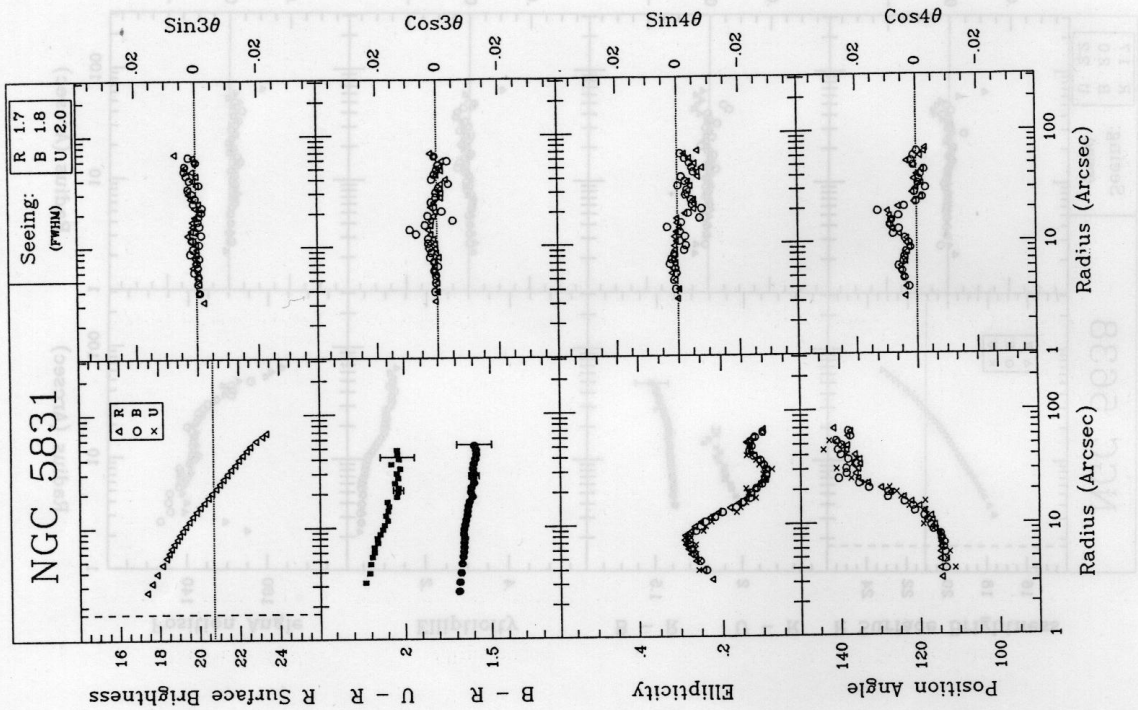
NGC 5831
Seeing: (FWHM)
R 1.7
B 1.8
U 2.0
Sin3θ
Cos3θ
Sin4θ
Cos4θ
R Surface Brightness
U − R
B − R
Ellipticity
Position Angle
Radius (Arcsec)

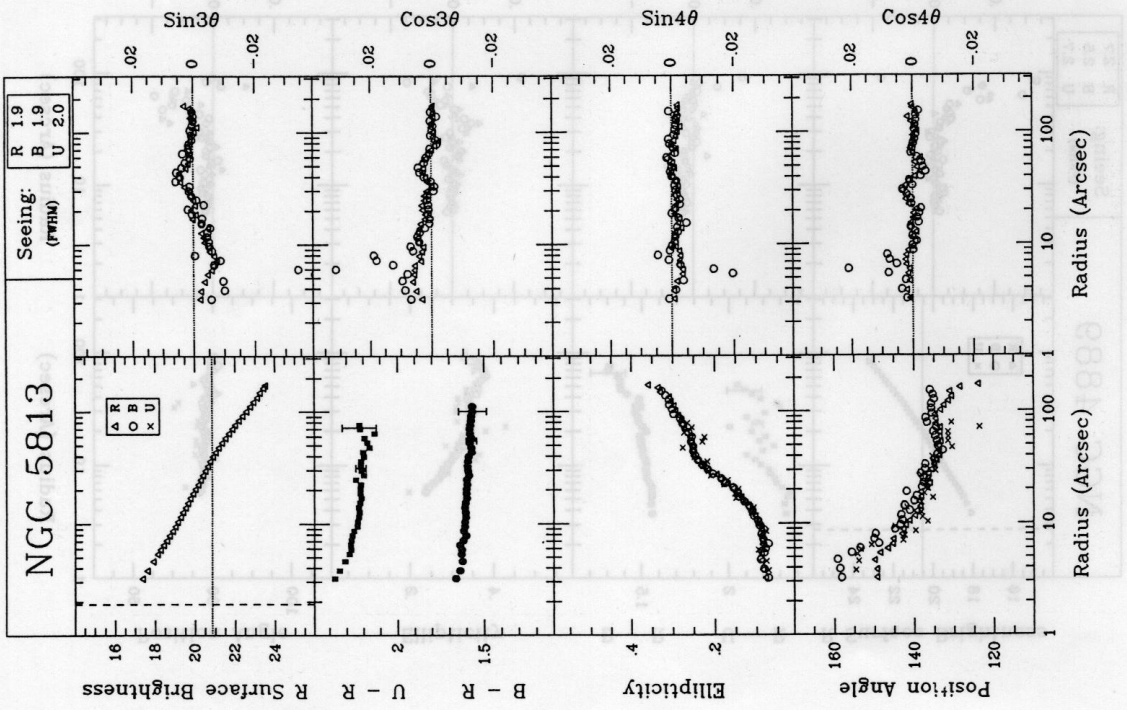
NGC 5813
Seeing: (FWHM)
R 1.9
B 1.9
U 2.0
Sin3θ
Cos3θ
Sin4θ
Cos4θ
R Surface Brightness
U − R
B − R
Ellipticity
Position Angle
Radius (Arcsec)

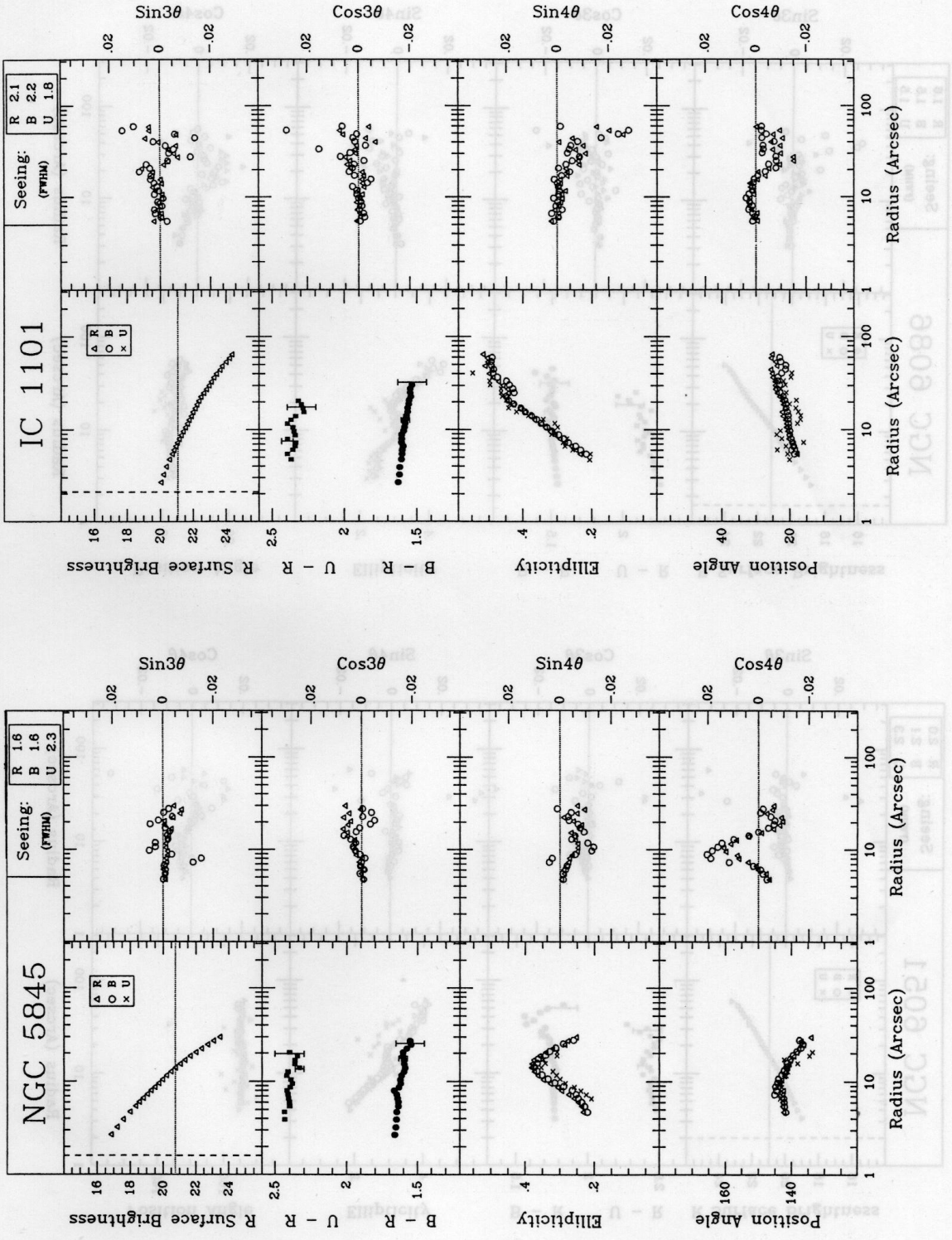
IC 1101
Seeing: (FWHM)
R 2.1
B 2.2
U 1.8
R Surface Brightness
U − R
B − R
Ellipticity
Position Angle
Sin3θ
Cos3θ
Sin4θ
Cos4θ
Radius (Arcsec)
NGC 5845
Seeing: (FWHM)
R 1.6
B 1.6
U 2.3
R Surface Brightness
U − R
B − R
Ellipticity
Position Angle
Sin3θ
Cos3θ
Sin4θ
Cos4θ
Radius (Arcsec)

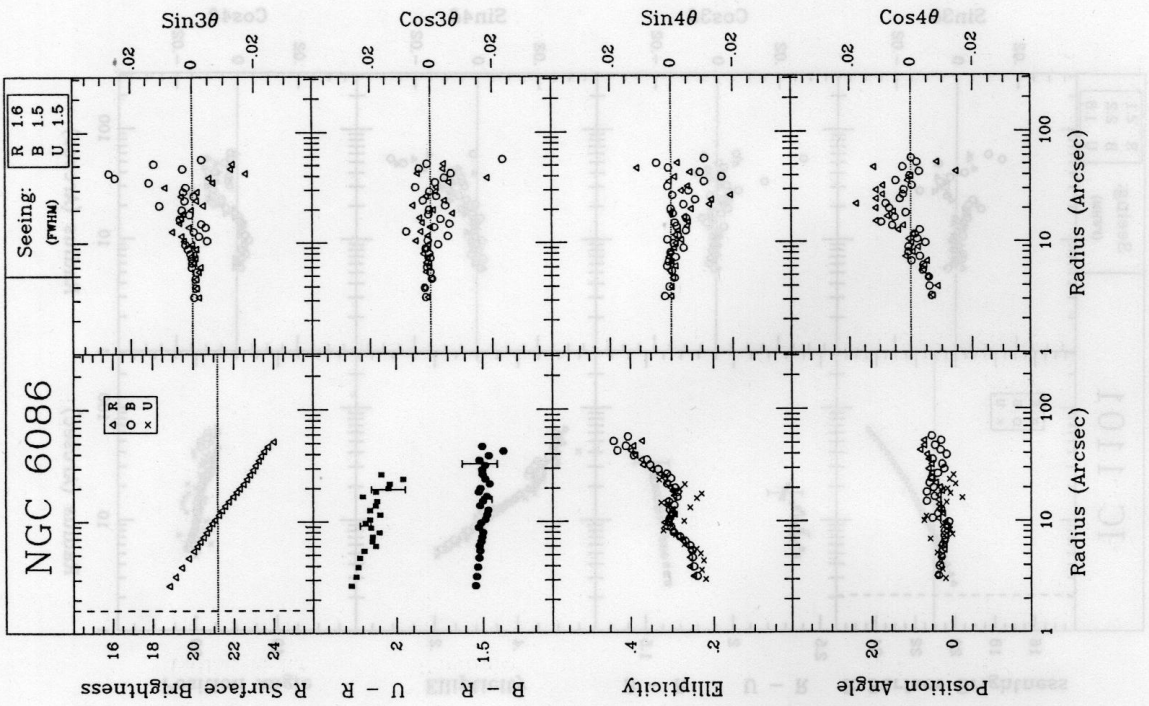
NGC 6086
Seeing: (FWHM)
R 1.6
B 1.5
U 1.5
R Surface Brightness
U − R
B − R
Ellipticity
Position Angle
Sin3θ
Cos3θ
Sin4θ
Cos4θ
Radius (Arcsec)

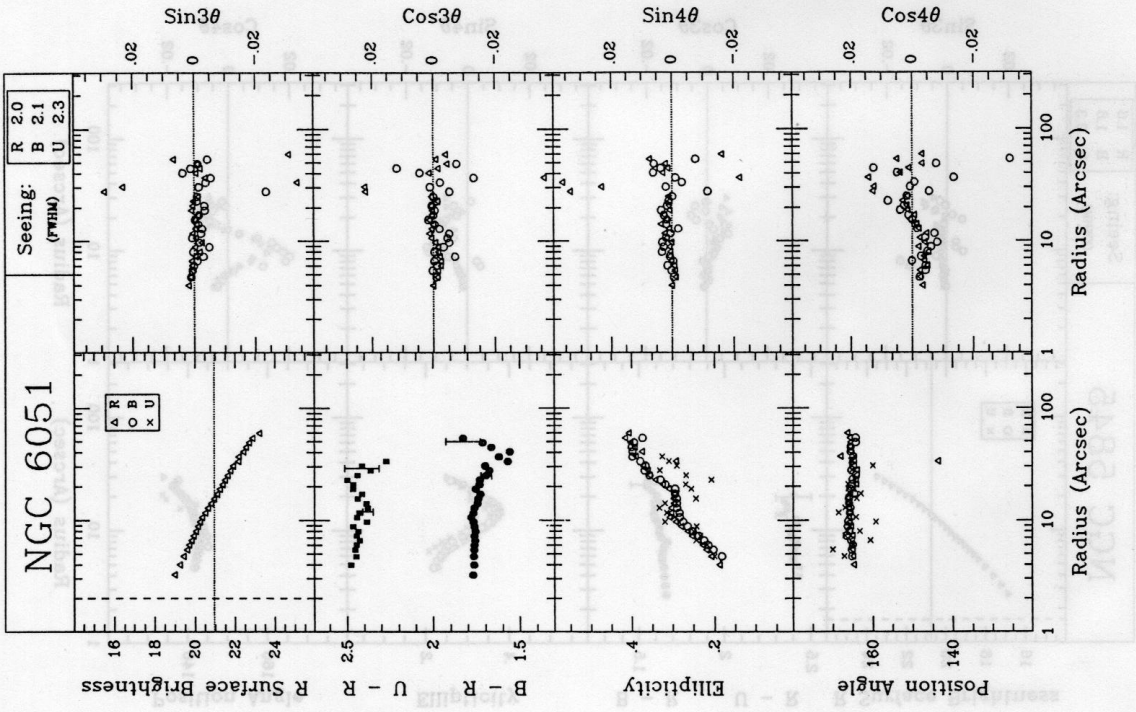
NGC 6051
Seeing: (FWHM)
R 2.0
B 2.1
U 2.3
R Surface Brightness
U − R
B − R
Ellipticity
Position Angle
Sin3θ
Cos3θ
Sin4θ
Cos4θ
Radius (Arcsec)

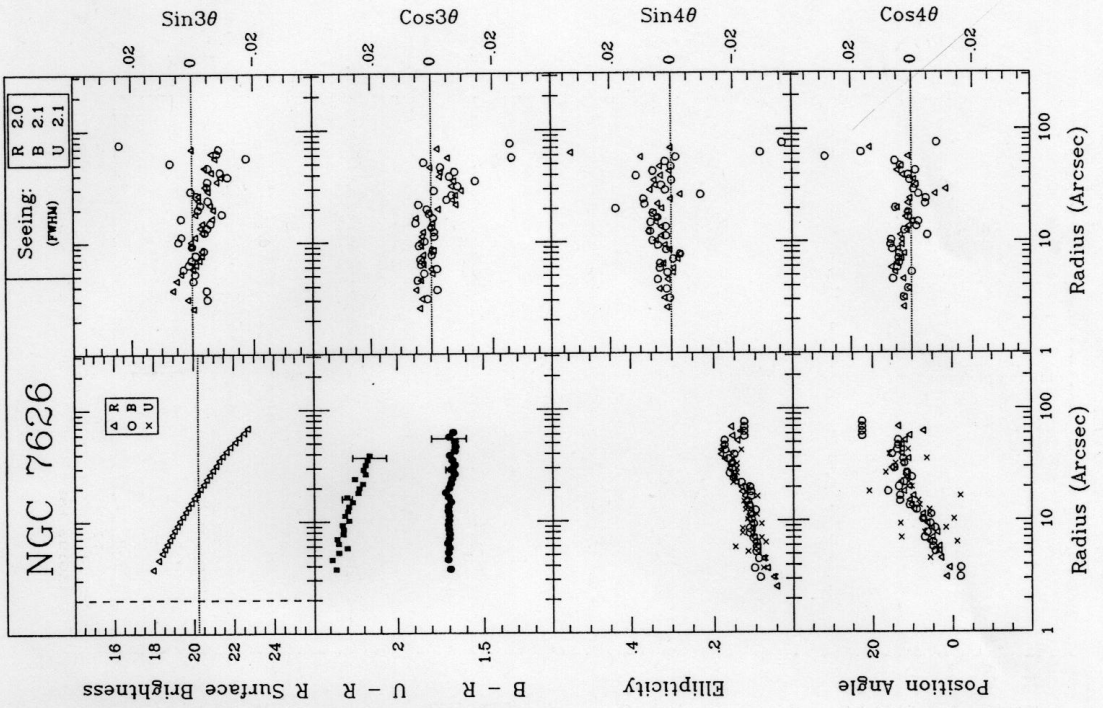
NGC 7626
Seeing: (FWHM)
R 2.0
B 2.1
U 2.1
R Surface Brightness
U − R
B − R
Ellipticity
Position Angle
Sin3θ
Cos3θ
Sin4θ
Cos4θ
Radius (Arcsec)

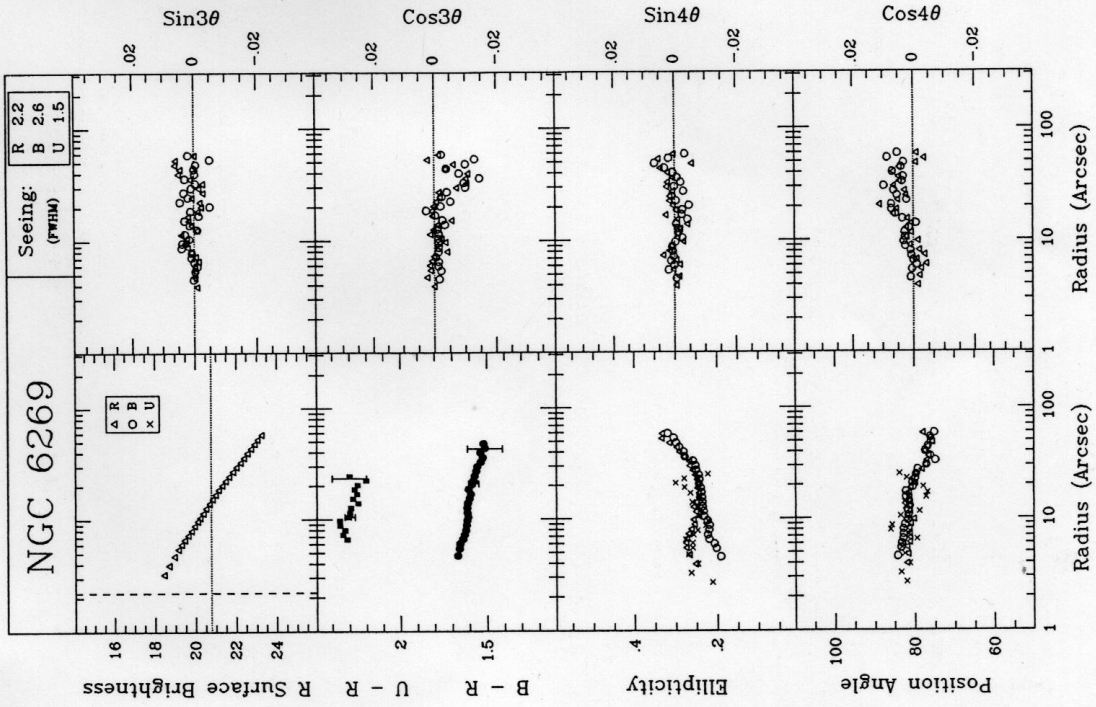
NGC 6269
Seeing: (FWHM)
R 2.2
B 2.6
U 1.5
R Surface Brightness
U − R
B − R
Ellipticity
Position Angle
Sin3θ
Cos3θ
Sin4θ
Cos4θ
Radius (Arcsec)